# Cantilever Based Mass Sensing

## Alternative Readout and Operation Schemes

**Dohn, Søren; Boisen, Anja; Hansen, Ole**

*Publication date:*
2007

*Document Version*
Publisher's PDF, also known as Version of record

# Cantilever Based Mass Sensing
## Alternative Readout and Operation Schemes

Søren Dohn[1]

November 9, 2006

[1]MIC - Department of Micro and Nanotechnology, Technical University of Denmark, Building 345E, 2800 Kgs. Lyngby, Denmark.

# Preface

This thesis has been written as a partial fulfilment of the requirements for obtaining the Ph.D. degree at the Technical University of Denmark (DTU). The Ph.D. project has been carried out at MIC - Department of Micro and Nanotechnology at DTU in the period from September 1, 2003 to November 9, 2006.

This Ph.D. project has been financed by a DTU Ph.D. grant and has been carried out as part of the NanoProbe project at MIC supervised by

**Professor, Anja Boisen**

**Associate Professor, Ole Hansen**

I would like to thank my two supervisors for their valuable help. Anja Boisen for her support, guidance and for giving me the chance to be a part of the NanoProbe group - I have learnt a lot, not merely scientifically. Ole Hansen for his valuable help on theoretical and practical matters regarding measurements - is there something you don't know about?

The NanoProbe group should also have it's recognition, both past and present members - I don't think a better group exists. The great social relationship within the group is an important key to achieving the high scientific level and friendly, helpful atmosphere that are always present.

A special thanks should also go to the NanoIntegration group lead by Associate Professor Peter Bøggild for help with equipment. I would also like to thank the rest of MIC for providing a really fruitful working atmosphere.

But the greatest of thanks goes to my family, Rebecca and Clara for their love, support and encouragement.

Søren Dohn
November 9, 2006
Department of Micro and Nanotechnology,
Building 345E
2800 Kgs. Lyngby Denmark

# Abstract

Cantilever based mass sensors utilize that a change in vibrating mass will cause a change in the resonant frequency. This can be used for very accurate sensing of adsorption and desorption processes on the cantilever surface. The change in resonant frequency caused by a single molecule depends on various parameters including the vibrating mass of the cantilever and the frequency at which it vibrates. The minimum amount of molecules detectable is highly dependent on the noise of the system as well as the method of readout.

The aim of this Ph.D. thesis has been twofold: To develop a readout method suitable for a portable device and to investigate the possibility of enhancing the functionality and sensitivity of cantilever based mass sensors.

A readout method based on the hard contact between the cantilever and a biased electrode placed in close proximity to the cantilever is proposed. The viability of the method is shown theoretically, and the output signal is shown to scale very well with the dimensions of the cantilever, and hence should be applicable to nano-scale cantilevers.

The hard contact method is proven to work on cantilevers on the micro- and nano-scale with measured resonant frequencies up to 11MHz. Values of the reciprocal frequency resolution as high as 80000 are obtained together with a signal to noise ratio of $10^8$. The result is an almost digital readout, which in turn simplifies the detection of the resonant frequency considerably.

An analytical expression is derived relating the mass and position of a particle attached to a cantilever to the resonant frequency. It is shown theoretical possible to find the mass and position of a particle by measurements of the resonant frequency of several bending modes.

In the measurements the sensitivity of the cantilever based mass sensor is improved when operated at higher bending modes. By measuring the resonant frequency of several bending modes both the mass and position of an attached gold bead are determined.

# Dansk Resumé

Bjælkebaserede masse sensorer fungerer ved at en ændring i den bevægelige masse vil ændre bjælkens resonans frekvens. Dette kan bruges til meget præcise målinger på de absorptions og desorptions processer der finder sted på bjælkens overflad. Ændringen i resonans frekvens når et enkelt molekyle sætter sig på overfladen afhænger af flere parametere, herunder massen af bjælken og den frekvens hvormed den vibrerer. Det antal molekyler, der minimum skal til for at kunne detekteres, afhænger af støjen i systemet såvel som udlæsningsmetoden

Målet for denne Ph.D. opgave har været at udvikle en udlæsningsmetode, der kunne bruges i transportable systemer, samt at undersøge muligheden for at forbedre funktionaliteten og følsomheden af bjælke baserede masse sensorer.

En udlæsningsmetode baseret på hård kontakt mellem bjælken og en elektrode, som placeres tæt ved bjælkens spids og pålægges et elektrisk potentiale, er præsenteret. Muligheden for at benytte udlæsningsmetoden er beskrevet teoretisk og det vises at udlæsnings signalet skalerer fint med dimensionerne af bjælken. Metoden burde således kunne benyttes på nano-skala bjælker.

Det er blevet vist, at metoden med hård kontakt mellem elektroden og bjælken virker på mikro- og nano-skala bjælker med målte resonans frekvenser op til 11MHz. Den inverse frekvensopløsning opnået med metoden er så høj som 80000 med et signal-støj forhold på $10^8$. Dette resulterer i en næsten digital udlæsning, der simplificrer udlæsningen af resonans frekvensen betragteligt.

Et analytisk udtryk der sammenkæder massen og positionen af en partikel, der sætter sig på bjælken, med resonans frekvensen er fundet. Det er således teoretisk muligt at bestemme massen og positionen ud fra målinger af resonans frekvensen for grundtonen og nogle få overtoner.

Ud fra målinger findes det, at følsomheden af den bjælkebaserede masse sensor forøges ved at operere den ved overtonerne. Ved at måle på flere overtoner samt grundtonen bestemmes både positionen og massen af en guld-kugle på bjælkens overflade.

# Table of Contents

# List of Figures

# List of Tables

# Chapter 1

# Introduction

On the earth sensors of nature have been a critical part of the evolution of sophisticated life-forms giving their owner advantages in terms of ability to sense food, detect hostile competitors, and find suitable partners.

The biological sensors of today are highly specialized and with capabilities that humans are striving to reproduce. With the development of micro-electro-mechanical systems (MEMS) we were given a new tool to improve the man-made sensors, resulting in the development of highly compact sensor systems reproducing the senses familiar to all of us: The eye [1] (charged-coupled device - used in commercial digital camera and mobile phones), the ear [2, 3] (micro machined microphone - used in hearing-aids and mobile phones on the market) and the nose [4, 5].

Currently, the sensors are evolving from MEMS into nano-electro-mechanical system (NEMS) thereby trying to mimic the length scales of nature itself. One sensor technology which is seen to have promising capabilities at the nanoscale is the cantilever based sensor [6, 7]. A cantilever based sensor consist of a cantilever coated with a recognition layer in addition to a system transforming the mechanical response of the cantilever into an electrical signal.

Cantilever based sensors are used for a wide variety of applications and can generally be operated in either static of dynamic mode. In the static mode the signal response in the cantilever based sensor is created by a bending of the cantilever. The bending can be due to a surface stress caused by a chemical or biochemical reaction on the cantilever surface [8, 9] or by the bimorph effect caused by a change in temperature [10–12]. In the dynamic mode the cantilever based sensor is commonly used as a mass sensor and is therefore called a cantilever based mass sensor. The focus in this Ph.D. thesis is on the cantilever based mass sensor.

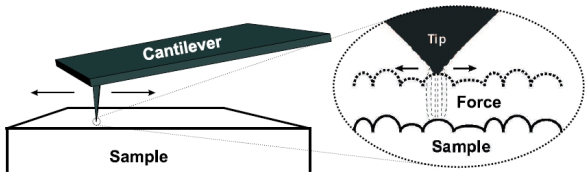


**Figure 1.1:** The principle of an atomic force microscope. The forces between a sharp tip and the sample is translated into a bending of the cantilever. By scanning the cantilever across a surface the surface metrology can be obtained with atomic resolution. Reproduced from [14].

## 1.1 Cantilever Based Mass Sensors

The ancestor of the cantilever based mass sensor is the atomic force microscope (AFM) [13]. In the AFM a sharp tip is positioned at the apex of a cantilever, and the sample-tip interaction forces are measured while scanning the cantilever across a surface (figure 1.1). Combining this with an optical readout method, where a laser beam is reflected on the backside of the cantilever and the position of the reflected beam is monitored [15], the topography of a surface can be found with atomic resolution. Some of the first to investigate the principle of the cantilever based mass sensor were Chen *et al.* [16] and Thundat *et al.* [17]. They used the fact that every mechanical structure has a resonant frequency, and the resonant frequency is highly dependent on the geometry, material parameters, to some degree the surrounding media, and the force exerted upon it. By monitoring the resonant frequency of a cantilever exposed to, for instance, molecules in the gas phase, any absorbance may be measurable as a change in resonant frequency due to the change of vibrating mass, geometry and surface stress (figure 1.2).

The cantilever based mass sensor is a generic platform and can be designed to the

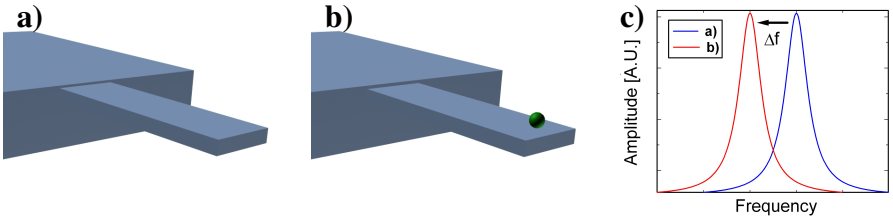


**Figure 1.2:** The principle of a cantilever based mass sensor. The frequency response of the unloaded cantilever (a) and of the cantilever with an attached particle (b) is measured and plotted (c) and from the change in resonant frequency, $\Delta f$ the mass of the attached particle can be found.

specific area of interest, and one of the major advantages of the cantilever based mass sensor is that it provides label free detection of target molecules. Measurements have been performed on a wide variety of substances, including hydrogen absorbance in carbon nanotubes [18], chemical vapours [17], and single cell detection [19].

### 1.1.1 Sensitivity

One of the ultimately goals of the cantilever based mass sensor is the ability to measure single small molecules which requires a sensitivity in the sub zepto-gram ($10^{-21}$g) regime. The minimum detectable mass depends on the ratio between the mass of the cantilever and the resonant frequency of the cantilever. Generally the resonant frequency increases when the dimensions are decreased, so a straightforward approach to enhance the sensitivity is to decrease the dimensions of the cantilever. The feature size of cantilever based mass sensor are currently approaching the nano-meter scale. Recently systems capable of detecting masses in the atto- and zepto-gram ($10^{-18} - 10^{-21}$g) range have been reported [20, 21], and the claim is that yocto-gram sensitivity is within reach [22]. This is by far better than the reported sensitivities of other mass sensing techniques, such as the quartz crystal microbalance technique where typical sensitivities are in the nano/pico-gram range [23] for a single device.

However, not only the mass and resonant frequency are important - the mechanical losses and noise of the cantilever, as well as the readout system are equally important. The noise and losses of the mechanical system are often associated with the media surrounding the cantilever, and high-sensitivity cantilever based mass sensors are generally operated at low pressures [24]. Metal coatings of the cantilever are widely used to allow for surface chemistry, but are also a significant source of damping [25]. The noise of the readout system is associated with the transduction of the mechanical response into an electrical signal and depends highly on the method of choice [20, 26–31].

### 1.1.2 Actuation and Readout

To make the cantilever vibrate several mechanisms can be used depending on the purpose, desired sensitivity and to some extent on the method of readout. The most common ways of actuation and readout from the cantilever are schematically shown in figure 1.3.

A common way of actuating cantilever based mass sensors is by electrostatic actuation, where a nearby electrode is biased with an alternating voltage with regard

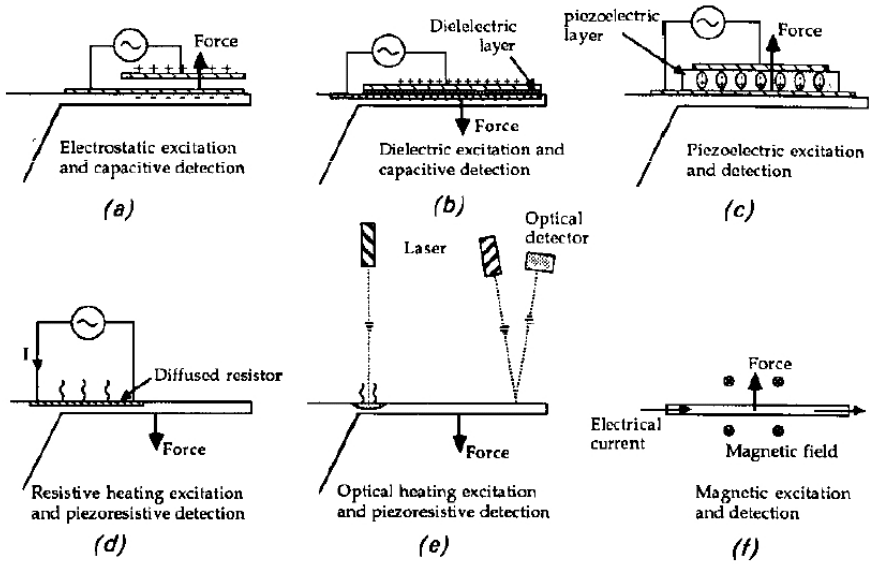


**Figure 1.3:** Schematic of the most common cantilever actuation and readout principles. The relevant techniques are explained in the text. Reproduced from [32] - notice that the caption of part (e) should say optical heating excitation and optical detection.

to the cantilever. This creates a periodic, electrostatic force on the cantilever that can actuate and excite the cantilever. Electrostatic actuation is often used together with capacitive readout, since the motion of the cantilever causes a change in the charge on the actuation-electrode and cantilever, which in turn causes a current to flow. Capacitive readout is easy to integrate in a chip, but is extremely sensitive to stray/parasitic capacitance and integration of elaborate electronic readout systems on the cantilever chip are necessary [33, 34]. Furthermore, the strong actuation signals contaminate the desired readout-signal since they share the same frequency, and therefore advanced measurement techniques must be used.

Actuation by piezo-eletric means is adopted from standard AFM configurations, where a piezo-eletric material is sandwiched between metal electrodes. An applied voltage will cause a change in the dimensions, and by applying an alternating voltage, the cantilever can be actuated. Using the reverse principle to generate a voltage when the piezo-electric material is strained, the piezo-electric material can also be used for readout either in combination with piezo-electric actuation [35] or other actuation mechanisms [36]. When combined, the strong actuation signals contaminate the desired readout-signal since they share the same frequency as in the case of electrostatic actuation and capacitive readout.

Heating of the cantilever will in most cases cause a bending due to the bimorph-

effect, and this is also used for actuation of the cantilever. The heating can be done by internal heaters [37, 38], or by an external laser source [39]. The laser is also commonly used as a method of readout, either by the AFM-method [15] or by sophisticated interferometrical methods [40–42]. The drawback of these methods is that delicate aligning of the detection optics to the cantilever chip is required when scaling the cantilever to the nano-scale.

A method very often used for extreme sensitivity cantilever based mass sensor is magnetomotive actuation and readout. By driving an alternating current through a built-in conductor and at the same time applying a static magnetic field, the cantilever can be actuated by the Lorenz force on the moving electrons [43–45]. The movement of the conductor in the electric field at the same time generates a current, by which readout of the cantilever can performed. The method requires magnetic fields in the order of 1-10T and elaborate cooling of the device, electronics as well as superconductors is often used to achieve this, making the method highly unsuitable for real applications.

## 1.2 Thesis Outline

The aim of the Ph.D. project has been twofold: To develop a readout method suitable for a portable device and to investigate the possibility of enhancing the functionality of cantilever based mass sensors by detection of several compounds using a single cantilever.

### 1.2.1 Position and Mode Dependence

When the frequency response of a cantilever based mass sensor is evaluated to estimate the weight of adsorbed molecules it is always assumed that the added molecules are either distributed in a homogenous layer all over the cantilever [21] or as a point mass at the tip of the cantilever [46]. The mass response of a cantilever based mass sensor changes with the position of the added mass because all parts of the beam do not move equal distances [47], and the approach is thereby inconsistent with the vision of having single molecule sensitivity.

A tool is needed to make use of the unmatched sensitivity of cantilever based mass sensor and to do real and reliable single molecule detection. The same kind of tool would be extremely useful in the emerging field of hollow cantilevers [48] in which the target molecules flow through the cantilever or bridge and, in some approaches, adsorb on the surface at a random position. The channel will not allow for monitoring of the position, and a tool for telling both position and mass

of the attached particles would be beneficial.

In this thesis, formulas are derived from which the position of an added mass can be deduced from measurements of several bending modes. The formulas will be compared to measurements of the change in resonant frequency as a function of the mass position [47]. Using experimental data, the theory will be shown to be able to predict the mass and position of the attached particle.

### 1.2.2 Hard Contact Readout

A great challenge still at hand is to make portable sensor systems working in ambient conditions with such high sensitivity as demonstrated by [18,20,21]. For small, stationary systems the desired sensitivity could probably be realized using optical detection. However, the delicate alignment of the detection optics to the cantilever chip will make the system hard to use. Electronic detection relaxes the alignment requirements and can be highly compact, but since integration of elaborate electronics and readout systems on the cantilever chip are necessary [33,34], the chips will be rather costly. A further problem is that the total area of the chip will be dominated by the area of the electronics compared to the area of the sensing elements.

In this thesis it is shown that detection of the resonant frequency of a cantilever based mass sensor is possible by measuring the time average current flowing from an electrode to the cantilever during hard contact occurring once every cycle of the cantilever vibration. The electronic detection method provides very high resolution in ambient conditions using simple low bandwidth off-chip electronics. Moreover, the detection method does not suffer from the common problem in electronic detection methods, where the strong actuation signals often contaminate the detected signal.

### 1.2.3 Chapters Outline

**Chapter 2** The general theory applicable to cantilever based mass sensors is presented. This includes a derivation of the resonant frequency for cantilevers as well as their responsivity. The effects of dissipation and noise will be discussed together with the effects of forces on a cantilever.

**Chapter 3** The theory developed for evaluation of the position dependent mass responsivity is derived in this chapter. A theoretical example is given to show that the position and mass can be determined from measurements of several bending modes.

**Chapter 4** The principle and theory behind the hard contact readout method are presented. Also, several considerations relevant for the method of readout are discussed.

**Chapter 5** The fabrication process of cantilevers used for investigation of hard contact readout is presented. The design considerations based upon the theoretical assumption are discussed.

**Chapter 6** The experimental setup needed for performing measurements on both the position dependent mass sensitivity and the fabricated devices for testing of the hard contact readout method is presented.

**Chapter 7** Measurements on the position dependent mass sensitivity are presented and compared to the theoretical findings. The ability of finding the position and mass of an attached particle is tested. Finally the obtained results are discussed.

**Chapter 8** The hard contact readout method is characterized by measurements on the fabricated devices. Measurements of lifetime, of change in mass and on nano-scale cantilevers are presented. The obtained results are discussed after each section.

**Chapter 9** A conclusion is made based on the findings.

There are several appendices at the end of the thesis containing a list of publications (Appendix A), a derivation of the spring constant of a coated cantilever (Appendix B), and detailed process parameters for the devices fabricated (Appendix C-D). The abbreviations used throughout the thesis are listed in Appendix E, and the physical constants used in calculations and simulations are listed in Appendix F.

# Chapter 2

# General Cantilever Theory

A general cantilever theory relevant for cantilever based mass sensors will be presented below. Several aspects will be addressed like resonant frequency, mass responsivity, spring hardening and softening. Also, important issues regarding dissipation and noise will be described.

## 2.1 Fundamentals of Cantilever Theory

In the following some general cantilever theory will be presented starting with the governing equation of motion from which the resonant frequencies of a cantilever will be deduced. In addition, the topic of mass responsivity will be covered.

### 2.1.1 The Beam Equation

The equation of motion for a cantilever with length, $L$, width, $w$, and height $h$ like the one depicted in figure 2.1 is given by the Euler-Bernoulli beam equation [49]

$$\frac{\partial^2 U(z,t)}{\partial t^2}\rho\Gamma + \frac{\partial^4 U(z,t)}{\partial z^4}EI = 0\,, \tag{2.1}$$

where $U(z,t)$ is the displacement in the $y$-direction, $\rho$ is the density, $\Gamma = wh$ is the cross-sectional area, $E$ is the Young's modulus, and $I$ is the area moment of inertia of the beam. The solution to this differential equation is a harmonic, $U(z,t) = U(z)e^{-\mathrm{i}\omega_n t}$, where $\omega_n$ is the resonant frequency. By insertion into equation 2.1 the spatial solution can be found

$$\frac{d^4 U(z,t)}{dz^4} = \kappa_n^4 U(z,t), \quad \kappa_n^4 = \frac{\omega_n^2 \rho\Gamma}{EI} \tag{2.2}$$

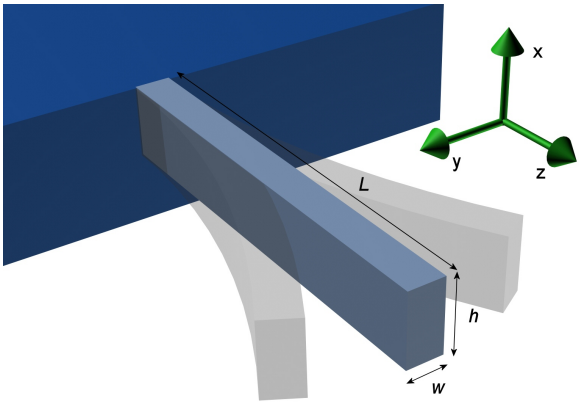


**Figure 2.1:** Schematic of a vibrating cantilever. The cantilever has the length $L$, width $w$, and height $h$. The density of the cantilever is $\rho$ and Young's modulus is $E$.

$$\frac{d^4U(z,t)}{dz^4} = \kappa^4 U(z,t), \quad \kappa^4 = \frac{\omega^2 \rho \Gamma}{EI} \tag{2.3}$$

The boundary conditions of a fixed free beam are

$$U(0,t) = 0 \qquad \left.\frac{\partial U(z,t)}{\partial z}\right|_{z=0} = 0$$
$$\left.\frac{\partial U^2(z,t)}{\partial z^2}\right|_{z=L} = 0 \qquad \left.\frac{\partial U^3(z,t)}{\partial z^3}\right|_{z=L} = 0$$

Using the boundary conditions, the solution to equation 2.2 is on the form [50]

$$U_n(z) = A_n(\cos \kappa_n z - \cosh \kappa_n z) + B_n(\sin \kappa_n z - \sinh \kappa_n z)\,, \tag{2.4}$$
$$A_n/B_n = -1.362, -0.982, -1.001, -1.000, \ldots\,, \tag{2.5}$$

where $n$ denotes the modal number. The modal constants are determined from

$$\cos \kappa_n L \cosh \kappa_n L = -1 \tag{2.6}$$

having a value of

$$\kappa_n L = C_n = 1.875, 4.694, 7.855, 10.996, \ldots \tag{2.7}$$

The first four eigenmodes are shown in figure 2.2.

The eigenfunctions can be normalized to the desired value, but a convenient measure is to normalize so that $A_n = 1$ whereby

$$\int_0^L U_m(z) U_n(z) \mathrm{d}z = L\delta_{mn} \tag{2.8}$$

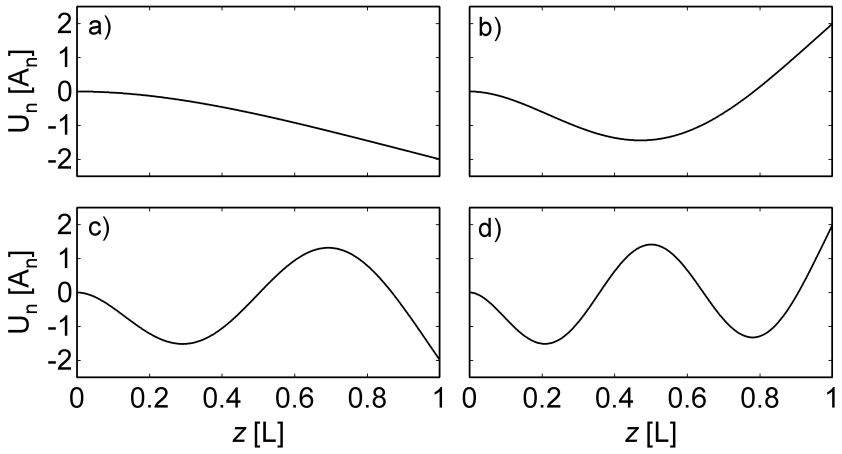


**Figure 2.2:** Schematics of the first four bending modes of a cantilever seen from the side. (a) shows first mode, (b) second mode and so forth. The amplitude is in units of $A_n$ and the position is in units of the length $L$, where 0 indicates the base of the cantilever.

### 2.1.2 Eigenfrequencies

The eigenfrequencies of the cantilever can be found from equation 2.2 but still the area moment of inertia needs to be calculated. The area moment of inertia when bending a structure around the x-axis is given by

$$I_x = \int_{\mathrm{A}} y^2 \mathrm{d}A \,, \tag{2.9}$$

where $y$ is the distance from the $z$-axis. In case of a rectangular, uniform cantilever the area moment of inertia is

$$I_{cant} = \int_{-h/2}^{h/2} \int_{w/2}^{w/2} y^2 \mathrm{d}y\mathrm{d}x = \frac{w^3 h}{12} \tag{2.10}$$

assuming small bending. For a coated cantilever the calculations are slightly more complicated (see Appendix B). The eigenfrequencies are from equation 2.2

$$\omega_n = \frac{C_n^2}{L^2}\sqrt{\frac{EI}{\rho\Gamma}} = \frac{C_n^2}{2\sqrt{3}}\frac{w}{L^2}\sqrt{\frac{E}{\rho}} \tag{2.11}$$

It is commonly used to simplify the beam-dynamics with that of a harmonic oscil-

lator, whereby the cantilever is assigned a spring constant and an effective mass.

$$\omega_n \equiv \sqrt{\frac{k}{m_{eff}}},$$
$$m_{eff} = \frac{3m_0}{C_n^4}, \quad m_0 = \rho\Gamma L, \quad k = \frac{3EI}{L^3} \tag{2.12}$$

The effective mass depends on the mode of vibration as can also be seen from figure 2.2 since the mass participating in the vibration changes with the mode.

### 2.1.3 Mass Responsivity

From equation 2.11 and 2.12 it is clear that the resonant frequency depends on the vibrating mass. The change in resonant frequency due to a change in mass is called the mass responsivity, $\mathcal{R}$, of the cantilever [51]. This is a very important parameter for cantilever based mass sensors, since it in turn will determine the minimum detectable mass.

Assuming that the change in mass, $\Delta m$ is very small compared to $m_0$ and distributed evenly over the entire cantilever surface, the mass responsivity of a cantilever can be found by differentiation of equation 2.11 with respect to the mass of the cantilever

$$\mathcal{R} \equiv \frac{\partial\omega_n}{\partial m_0} = -\frac{\omega_n}{2m_0} \approx \frac{\Delta\omega_n}{\Delta m}, \tag{2.13}$$

where $\Delta\omega_n$ is the change in the n$^{th}$ resonant frequency caused by an added mass, $\Delta m$.

To obtain a high mass responsivity the cantilever must have a high resonant frequency, which can be obtained by having a large Young's modulus, low density, and small dimensions. Furthermore, it must have a low mass, requiring a low density and small dimensions. The mass responsivity of the cantilever is seen to also depend on the mode of operation as $\mathcal{R} \propto C_n^2$, so a higher mass responsivity can be obtained at higher modes.

The smallest detectable mass or the sensitivity of the sensor, $\Delta m_{min}$, is given by the inverse responsivity times the minimum detectable frequency change $\Delta\omega_{min}$

$$\Delta m_{min} = \mathcal{R}^{-1}\Delta\omega_{min} \tag{2.14}$$

The frequency stability and thereby $\Delta\omega_{min}$ is determined by the noise of the system originating from both the readout circuitry and the resonator itself.

## 2.2 Dissipation and Quality Factor

A cantilever with a kinetic energy will experience damping and thereby dissipation of its kinetic energy. The dissipation is defined as the ratio of energy lost per cycle to the stored energy, and is the inverse of the quality factor ($Q$-factor).

Dissipation occurs through several mechanisms that are either intrinsic to the cantilever or extrinsic processes. The intrinsic processes are among others material damping (phonon-phonon interactions, phonon-electron interactions, and thermoelastic damping) [44, 52, 53] and anchor losses [32, 52, 54]. The extrinsic dissipation occurs due to interactions with the surrounding media and can be controlled by the mode of operation. The total dissipation is the sum of all contributions

$$\frac{1}{Q} = \sum \frac{1}{Q_{\text{int}}} + \sum \frac{1}{Q_{\text{ext}}} = \frac{1}{Q_{\text{mat}}} + \frac{1}{Q_{\text{anc}}} + \frac{1}{Q_{\text{sur}}} + ... \tag{2.15}$$

For single crystalline micro-cantilevers operated at ambient conditions viscous damping or momentum exchange with the surrounding medium is the dominant source of dissipation, giving rise to quite low $Q$-factors, $Q \sim 100$ [51]. If the cantilevers on the other hand are sandwiched structures or polymer cantilevers material damping can be dominant [25, 55].

### 2.2.1 Momentum Exchange

Momentum exchange occurs when the cantilever and the surrounding molecules collide and exchange energy and momentum, usually giving rise to a damping of the cantilever. For a resonator this affects the characteristics of the device tremendously, and is highly dependent on the gas pressure [24, 56], the dimensions [24, 56, 57], and the mode of operation [57, 58]. The damping mechanism can be divided in three regions depending on the pressure, $p$ [24]

**Intrinsic region** For $p < 1$Pa for most gasses the effect of momentum exchange is negligible compared to the intrinsic damping of the resonator

**Molecular region** The damping is caused by independent collisions between gas molecules and the resonator. This effect is dominating at $1 < p < 1000$Pa but the range depends highly on the geometry. The dissipation caused by the gas on a micro-scale cantilever was found by Blom *et al.* [24]

$$Q_{gas,m} = \omega_n \frac{w\rho}{C_n k_m p} , \tag{2.16}$$

where $k_m$ is the damping coefficient for air at room temperature (see Appendix F).

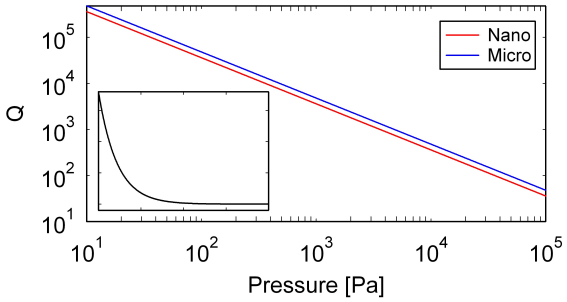


**Figure 2.3:** Pressure dependency of the $Q$-factor due to momentum exchange for nano- ($w$=200nm, $h$=220nm, and $L = 3.8\mu$m) and micro-scale ($w = 2\mu$m, $h = 2.5\mu$m, and $L = 50\mu$m) cantilevers. The inset shows the same graph with a linear $y$-axis.

**Viscous region** For $p > 1000$Pa the gas acts as a viscous fluid and damping is the dominant source of dissipation. The exact damping depends highly on the geometry of the resonator and must be calculated using fluid mechanics or measured.

An accurate description of the dynamics in the full pressure range requires governing equations in each range. A simplified expression suitable for a nanometer-scale cantilever describing the dissipation in the entire pressure range is given by Ekinci *et al.* [51]

$$Q_{gas} = m_{eff}\omega_n \nu / pA \,, \tag{2.17}$$

where $A = hL$ is the surface area of the resonator perpendicular to the motion and $\nu = \sqrt{k_B T / m_m}$ is the velocity of the molecules, where $m_m$ is the weight of the surrounding air molecules.

The simple model of Ekinci *et al.* anticipates a decrease in $Q$-factor when operating the cantilever at higher modes, whereas the model of Blom *et al.* anticipates that $Q \propto C_n$. In figure 2.3 the $Q$-factor due to momentum exchange is depicted as a function of pressure for a micro-scale (calculated using equation 2.16) and a nano-scale cantilever (calculated using equation 2.17). The nano-scale cantilever is seen to have a slightly lower $Q$-factor than the micro-scale cantilever in these calculations.

### 2.2.2 Zener's Model

The influence of dissipation on the dynamics of cantilevers can be described by adding a damping term in the beam equation (equation 2.1) or by Zener's formal-

ism [50]. Zener's formalism account for the physics in intrinsic damping and in the following this theory will be presented.

Standard stress-strain theory uses the basic assumption that materials are elastic, meaning that no irreversible processes take place during the deformation. Zener was the first to generalize Hooke's stress-strain relation $\sigma = E\epsilon$ to include inelastic processes, and thereby dissipation of energy and noise. This was done by allowing for mechanical relaxation, thus making the stress-strain relation dependent on the timescale of which a process occur. The formula for stress and strain in Zener's formalism is

$$\sigma + \tau_\epsilon \frac{d\sigma}{dt} = E_R \left( \epsilon + \tau_\sigma \frac{d\epsilon}{dt} \right) , \tag{2.18}$$

where $\tau_\epsilon$ and $\tau_\sigma$ are time constants characteristic for the strain and the stress, and $E_R$ is the relaxed value of Young's modulus. From the time constants an unrelaxed Young's modulus can be defined as $E_U = \frac{\tau_\sigma}{\tau_\epsilon} E_R$.

Looking at harmonic variations in the stress and strain in the form $\sigma = \sigma_0 e^{-i\omega\, t}$ and $\epsilon = \epsilon_0 e^{-i\omega\, t}$, and inserting in equation 2.18 an expression can be obtained for the time-dependent Young's modulus

$$\begin{aligned} \sigma_0(1 - \mathrm{i}\omega\tau_\epsilon) &= E_R\epsilon_0(1 - \mathrm{i}\omega\tau_\sigma) \Rightarrow \\ E(\omega) \equiv \frac{\sigma}{\epsilon} = \frac{\sigma_0}{\epsilon_0} &= E_R \frac{1 - \mathrm{i}\omega\tau_\sigma}{1 - \mathrm{i}\omega\tau_\epsilon} = E_R \frac{1 + \omega^2\tau_\epsilon\tau_\sigma - \mathrm{i}\omega(\tau_\sigma - \tau_\epsilon)}{1 + \omega^2\tau_\epsilon^2} \end{aligned}$$

By defining the three parameters

$$E_{\mathrm{eff}}(\omega) = \frac{1 + \omega^2\bar{\tau}^2}{1 + \omega^2\tau_\epsilon^2} E_R, \quad \bar{\tau} = \sqrt{\tau_\epsilon\tau_\sigma}, \quad \Delta = \frac{E_U - E_R}{\sqrt{E_R E_U}} = \frac{\tau_\sigma - \tau_\epsilon}{\bar{\tau}} ,$$

where $\Delta$ is the relaxation strength, the frequency dependent Young's modulus can be rewritten to

$$E(\omega) = E_{\mathrm{eff}}(\omega) \left( 1 - \frac{\mathrm{i}\omega\bar{\tau}}{1 + \omega^2\bar{\tau}^2} \Delta \right) \tag{2.19}$$

The imaginary part of Young's modulus determines the loss of the system.

From the frequency dependent Young's modulus and assuming a small $\Delta$ the mechanical dissipation or inverse $Q$-factor can be defined as the ratio between the imaginary and the real part of equation 2.19 as

$$Q^{-1} = \frac{\omega\bar{\tau}}{1 + \omega^2\bar{\tau}^2} \Delta \tag{2.20}$$

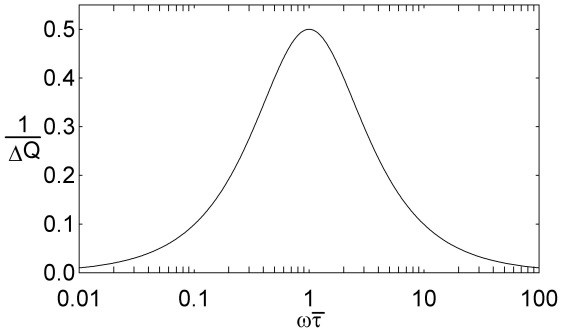


**Figure 2.4:** Dissipation according to Zener's model in units of the relaxation strength $\Delta$. The maximum dissipation occurs for $\omega = 1/\bar{\tau}$ where $\bar{\tau}$ is the characteristic relaxation time of the material.

The dissipation has a maximum $Q^{-1} = \Delta/2$ for $\omega = 1/\bar{\tau}$ (figure 2.4), and very little dissipation is occurring at small and large frequencies compared to the relaxation time. The explanation is that at low frequencies the material is essentially in equilibrium and very little energy is dissipated, while at high frequencies the material has no time to relax and hence dissipate energy.

The eigenfrequencies found in section 2.1 was derived assuming no dissipation. When using Zener's model for the relation between stress and strain this can be included (equation 2.19 and 2.20), giving the damped eigenfrequencies of

$$\begin{aligned} \omega_n' &= \frac{C_n^2}{L^2}\sqrt{\frac{EI(1-\mathrm{i}/Q)}{\rho\Gamma}}, \quad \left(1-\frac{\mathrm{i}}{2Q}\right)^2 = 1-\frac{2\mathrm{i}}{2Q}-\frac{1}{4Q^2} \approx 1-\frac{\mathrm{i}}{Q} \\ \omega_n' &\approx \left(1-\frac{\mathrm{i}}{2Q}\right)\omega_n\,, \end{aligned} \tag{2.21}$$

where $E = E_{eff}$ is assumed to be constant in the frequency range of interest, and the last part holds in the limit of a large $Q$-factor (if Q≥100 the error on $\omega_n'$ is smaller than $10^{-5}\omega_n$). Putting the eigenfrequencies into the solution to the beam-equation the time dependent amplitude will look like

$$U_n(z,t) = U_n(z)e^{-\mathrm{i}\omega_n' t} = U_n(z)e^{-\mathrm{i}\omega_n t}e^{-\omega_n t/2Q}\,, \tag{2.22}$$

where the real exponent indicates a decay of the amplitude with a characteristic time of $\omega_n/2Q$.

## 2.3 Forces on a Cantilever

In the preceding sections the cantilever has been assumed to vibrate with no external forces other than damping mechanisms. To actually make it vibrate with an amplitude comparable to the dimensions of the cantilever external forces are required. The effect on the beam dynamics of a force acting on the cantilever will be described in the following.

### 2.3.1 Amplitude of a Driven Cantilever

Assuming that the cantilever is driven with a harmonic force with the frequency $\omega_c$, $F(z,t) = f(z)e^{-i\omega_c t}$ per unit length, the beam equation equation 2.1 is modified to

$$\frac{\partial^2 U(z,t)}{\partial t^2}\rho\Gamma + \frac{\partial^4 U(z,t)}{\partial z^4}EI = f(z)e^{-i\omega_c t} \tag{2.23}$$

To solve the equation it is necessary to write the displacement function as a summation over all the eigenfunctions, where it is assumed that the transient is over and all movement depends only on $\omega_c$

$$U(z,t) = \sum_{n=1}^{\infty} a_n U_n(z) e^{-i\omega_c t} \tag{2.24}$$

The position dependent amplitude can now be found by putting the eigenfunction into equation 2.23. Differentiation with respect to time and position gives

$$\frac{\partial^2 U(z,t)}{\partial t^2} = -\omega_c^2 \sum_{n=1}^{\infty} a_n U_n(z) e^{-i\omega_c t} \tag{2.25}$$

$$\frac{\partial^4 U(z,t)}{\partial z^4} = \sum_{n=1}^{\infty} a_n \frac{\mathrm{d}^4 U_n(z)}{\mathrm{d}z^4} e^{-i\omega_c t} \tag{2.26}$$

To determine the derivative with respect to the position of the eigenfunctions it is necessary to use the non-driven beam equation

$$\begin{aligned} &\frac{\partial^2 U(z,t)}{\partial t^2}\rho\Gamma + \frac{\partial^4 U(z,t)}{\partial z^4}EI = 0 \quad \Rightarrow \\ &\frac{\partial^4 U(z,t)}{\partial z^4} = -\frac{\rho\Gamma}{EI}\frac{\partial^2 U(z,t)}{\partial t^2} = \frac{\rho\Gamma}{EI}\omega_n'^2 \sum_{n=1}^{\infty} a_n U_n(z) e^{-i\omega_n' t} \end{aligned} \tag{2.27}$$

The angular frequency involved in the time-dependent part of the solution is replaced by $\omega_c$. Using equation 2.25-2.27 and inserting into equation 2.23 the fol-

lowing can be obtained

$$-\omega_c^2 \sum_{n=1}^{\infty} a_n U_n(z) e^{-\mathrm{i}\omega_c t} \rho\Gamma + \rho\Gamma\omega_n'^2 \sum_{n=1}^{\infty} a_n U_n(z) e^{-\mathrm{i}\omega_c t} = f(z) e^{-\mathrm{i}\omega_c t} \quad \Rightarrow$$

$$\rho\Gamma(\omega_n'^2 - \omega_c^2) \sum_{n=1}^{\infty} a_n U_n(z) = f(z) \tag{2.28}$$

Multiplying with the eigenfunctions on both sides and integrating over the length, an expression involving the individual amplitudes is found

$$\rho\Gamma(\omega_n'^2 - \omega_c^2) \int_0^L \sum_{n=1}^{\infty} a_n U_n(z) U_{n'}(z) \mathrm{d}z = \int_0^L f(z) U_n(z) \mathrm{d}z \quad \Rightarrow$$

$$\rho\Gamma(\omega_n'^2 - \omega_c^2) a_n L = \int_0^L f(z) U_n(z) \mathrm{d}z \,, \tag{2.29}$$

where the normalization and orthogonality of the eigenfunction are used in the derivation of the last line. It is now possible to solve for the position dependent displacement by inserting the definition of the damped eigenfrequencies (equation 2.21)

$$a_n = \frac{1}{m_0} \frac{\int_0^L f(z) U_n(z) \mathrm{d}z}{\omega_n'^2 - \omega_c^2}$$

$$a_n = \frac{1}{m_0} \frac{\int_0^L f(z) U_n(z) \mathrm{d}z}{\omega_n^2 - \omega_c^2 - \mathrm{i}\omega_n^2/Q} \tag{2.30}$$

The complex amplitude means that the cantilever is vibrating out of phase with the applied force. Any given force can be described in terms of the eigenfunctions of the cantilever

$$f_n(z) = \frac{1}{L} \sum_{n=1}^{\infty} f_n U_n(z) \,, \tag{2.31}$$

whereby the amplitude for each mode is

$$a_n = \frac{1}{m_0} \frac{\frac{1}{L}\int_0^L U_n(z) f_n U_n(z) \mathrm{d}z}{\omega_n^2 - \omega_c^2 - \mathrm{i}\omega_n^2/Q} = \frac{f_n}{m_0} \frac{1}{\omega_n^2 - \omega_c^2 - \mathrm{i}\omega_n^2/Q} \tag{2.32}$$

### 2.3.2 Non-linear Forces

If the applied force on the cantilever is dependent on the deflection $F(z, U(z,t), t)$ equation 2.23 will be non-linear. This will result in an artificial spring constant

contributing either positive or negative to the original spring constant and effectively shifting the resonant frequency. Two concrete problems will be solved in the following. Spring softening caused by electrostatic actuation of the cantilever [33, 34, 59] and spring hardening often seen in dynamic AFM due to the tip-surface interaction [60, 61].

### Spring softening

For electrostatic actuation the force on the cantilever is positive and can be approximated with the forces between two plates of a plate capacitor with a distance $d$ (figure 2.5). The force on the cantilever is

$$f(z, U(z,t)) = \frac{\varepsilon_0 hL}{2(d - U(z,t))^2} V_{\mathrm{A}}^2, \quad C_0 = \frac{\varepsilon_0 hL}{d}\,, \tag{2.33}$$

where $C_0$ is the the total capacitance of the actuation-electrode and cantilever with no movement. The force is proportional to the square of the actuation voltage, that is

$$\begin{aligned} V_{\mathrm{A}}^2 &= \left(V_{\mathrm{A},dc} + V_{\mathrm{A},ac}\sin(\omega_c t)\right)^2 \\ &= V_{\mathrm{A},dc}^2 + 2V_{\mathrm{A},dc}V_{\mathrm{A},ac}\sin(\omega_c t) + V_{\mathrm{A},ac}^2\sin^2(\omega_c t) \\ V_{\mathrm{A}}^2 &= V_{\mathrm{A},dc}^2 + \frac{1}{2}V_{\mathrm{A},ac}^2 + 2V_{\mathrm{A},dc}V_{\mathrm{A},ac}\sin(\omega_c t) - \frac{1}{2}V_{\mathrm{A},ac}^2\cos(2\omega_c t) \end{aligned} \tag{2.34}$$

The resulting electrostatic force has a dc component, a component at the drive frequency, and a component at twice the drive frequency. If calculating the vibrating amplitude of the cantilever from equation 2.32 the component at the drive

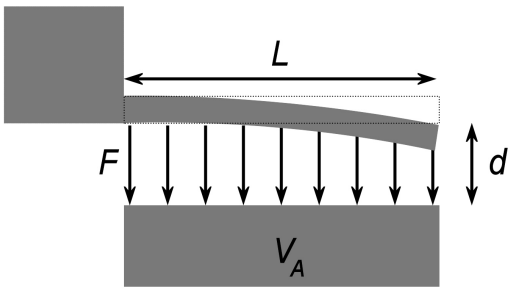


**Figure 2.5:** Schematics of electrostatic actuation of a cantilever. The cantilever has a height $h$ and a length $L$ with a distance to the actuation-electrode of $d$. The actuation-electrode is biased with $V_{\mathrm{A}} = V_{\mathrm{A},ac} + V_{\mathrm{A},dc}$ and the cantilever is grounded.

frequency is to be used. However, when calculating the resonant frequency only the time average of the force and thereby the dc component have an influence.

The static deflection of the cantilever due to the electrostatic forces is given from the static part of equation 2.23 as

$$\frac{\partial^4 U_0(z)}{\partial z^4} EI = \frac{\varepsilon_0 hL}{2(d - U_0(z))^2} \left\langle V_{\mathrm{A}}^2 \right\rangle , \quad \left\langle V_{\mathrm{A}}^2 \right\rangle = V_{\mathrm{A},dc}^2 + \frac{1}{2} V_{\mathrm{A},ac}^2 , \tag{2.35}$$

where $\left\langle V_{\mathrm{A}}^2 \right\rangle$ is the time average of the actuation voltage squared. Turning to the dynamic case, the solution is in the form $U(z,t) = U_0(z) + U_{eff}(z,t)$, and putting this into equation 2.23

$$\begin{aligned}
\frac{\partial^2 U_{eff}(z,t)}{\partial t^2} \rho\Gamma + \frac{\partial^4 \left( U_0(z) + U_{eff}(z,t) \right)}{\partial z^4} EI &= \frac{\varepsilon_0 hL}{2(d - U_0(z) - U_{eff}(z,t))^2} \left\langle V_{\mathrm{A}}^2 \right\rangle \\
\frac{\partial^2 U_{eff}(z,t)}{\partial t^2} \rho\Gamma + \left( \frac{\varepsilon_0 hL}{2(d - U_0(z))^2} \left\langle V_{\mathrm{A}}^2 \right\rangle \right. &+ \\
\left. \frac{\partial^4 U_{eff}(z,t)}{\partial z^4} EI \right) &= \frac{\varepsilon_0 hL}{2(d - U_0(z) - U_{eff}(z,t))^2} \left\langle V_{\mathrm{A}}^2 \right\rangle \\
\frac{\partial^2 U_{eff}(z,t)}{\partial t^2} \rho\Gamma + \frac{\partial^4 U_{eff}(z,t)}{\partial z^4} EI &\approx \frac{2\varepsilon_0 hL}{(d - U_0(z))^3} U_{eff}(z,t) \left\langle V_{\mathrm{A}}^2 \right\rangle
\end{aligned} \tag{2.36}$$

The solution is in the form of equation 2.24 where the angular frequency is $\omega_{eff}$. Assuming that $U_0(z) \ll d$ the effective angular frequency becomes

$$\omega_{eff}^2 \approx \omega_n'^2 - \frac{2C_0}{m_{eff} d^2} \left\langle V_{\mathrm{A}}^2 \right\rangle \tag{2.37}$$

$$k_{eff} \approx k' - k_{spring} = k' - \frac{2C_0}{d^2} \left\langle V_{\mathrm{A}}^2 \right\rangle \tag{2.38}$$

Effectively, the square of the resonant frequency depends on the applied voltage as $V_{\mathrm{A},dc}^2 + 1/2 V_{\mathrm{A},ac}^2$, and the spring softening effect can be used for frequency tuning [62–64].

### Spring hardening

If on the other hand, the force is negative and originating from a surface constraining the cantilever, the resonant frequency will increase. In this case the cantilever is constrained to a maximum amplitude of $a_{con}$ at the tip by a force $f(z) = f_{con}\delta(z - L)$.

Looking at the tip of the cantilever the position can be described as

$$U(L,t) = -2a_n \cos(\omega_n' t)$$

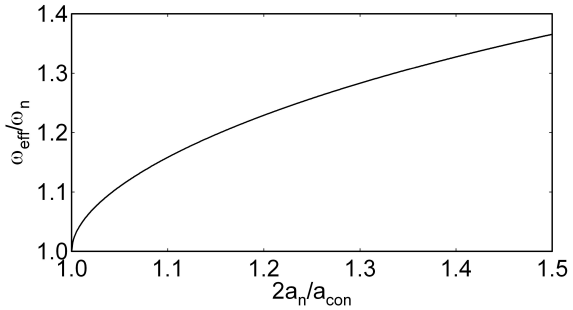


**Figure 2.6:** The effect of spring hardening on the resonant frequency. The apparent resonant frequency in units of the resonant frequency as a function of the ratio between the unconstrained and constrained amplitudes is depicted.

If the cantilever tip is constrained to have a maximum amplitude of $U(L,t) = a_{con}$ then the following equality must hold

$$U(L, T/2) = -2a_n \cos(\omega_n' T/2) \leq a_{con}, \quad T = \frac{2\pi}{\omega_n'}$$

For the case where the unconstrained amplitude would be larger than $a_{con}$ this evaluates to

$$\begin{aligned} \omega_n' \frac{T}{2} &= \arccos\left(-\frac{a_{con}}{2a_n}\right) \quad \Rightarrow \\ \omega_{eff} &= \frac{2\pi}{T} = \omega_n' \frac{\pi}{\arccos\left(-\frac{a_{con}}{2a_n}\right)} \end{aligned} \tag{2.39}$$

In figure 2.6 the relative change in resonant frequency due to a constraint on the cantilever tip can be seen as a function of the unconstrained amplitude. The change is seen to be in the order of 10% for small amplitudes.

## 2.4 Noise

The noise in mechanical systems is an unavoidable factor that influences every measurement. The source of noise present in a system originates from two different kinds of sources. One source is the thermo-mechanical noise, which can be described by the Zener's model, showing the intimate link between dissipation and noise [32]. The other is external noise sources including noise from measurement equipment [65, 66]. The latter depends highly on the system, mode of operation and measurement parameters, and will not be described further here. Other important external noise sources are temperature fluctuation noise, adsorption and

desorption noise. Only noise due to adsorption and desorption will be presented here since it is regarded as being the most important when operating a cantilever based mass sensor at ambient conditions [66].

### 2.4.1 Thermo-mechanical Noise

At thermal equilibrium the mean total energy $\langle\varepsilon\rangle$ of a system will be equal to the thermal energy $k_{\mathrm{B}}T$ and this energy will be distributed in the degrees of freedom available [51]. In the case of a cantilever this is kinetic vibrational energy and potential strain energy.

$$\frac{1}{2}m\langle\dot{x}^2\rangle = \frac{1}{2}k\langle x^2\rangle = \frac{1}{2}k_{\mathrm{B}}T \tag{2.40}$$

Since the energy of a single specific system is not equal to the ensembled average, energy will be exchanged with the surroundings through the available degrees of freedom by random and irreversible processes. The exchange of energy will introduce mechanical noise due to fluctuating forces on the system according to the fluctuation-dissipation theorem [50].

#### Amplitude noise

From the energy of the cantilever it is possible to find the amplitude noise. Assuming that the noise force is proportional to the eigenfunctions, the amplitude of each mode can be described using equation 2.32, where $f_n = f_n(t)$. The spectral density of the amplitude and thereby the amplitude noise for each mode can be found doing a Fourier transform of the amplitude

$$\begin{aligned} S_{a_n}(\omega) &= \frac{1}{2\pi}\int_{-\infty}^{\infty}|a_n|^2 e^{-\mathrm{i}\omega\mathrm{t}}\mathrm{d}t \\ S_{a_n}(\omega) &= \frac{1}{(\omega_n^2-\omega^2)^2+(\omega_n^2/Q)^2}\frac{S_f(\omega)}{m_0^2} \end{aligned} \tag{2.41}$$

$S_f(\omega)$ is the spectral density of the noise force and can be derived looking at the kinetic energy of the cantilever. The average kinetic energy of each degree of freedom and for each mode is calculated from the standard definition $\langle E_{kin}\rangle = 1/2m\left\langle\dot{x}^2\right\rangle$, i.e.

$$\langle E_{kin}\rangle = \frac{1}{2}\int_0^L \rho\Gamma\left|\frac{\partial U_n(z,t)}{\partial t}\right|_{noise}^2 \mathrm{d}z \tag{2.42}$$

Looking at the entire frequency range

$$\left|\frac{\partial U_n(z,t)}{\partial t}\right|^2_{noise} = \int_0^\infty S_{\dot{U}_n}(\omega)\mathrm{d}\omega\,, \tag{2.43}$$

where

$$\begin{aligned} S_{\dot{U}_n}(\omega) &= \frac{1}{2\pi}\int_{-\infty}^{\infty}\left|\frac{\partial U_n(z,t)}{\partial t}\right|^2_{noise} e^{-\mathrm{i}\omega t}\mathrm{d}t \\ &= \frac{1}{2\pi}\int_{-\infty}^{\infty}\omega_n^2 a_n^2 U_n^2 e^{-\mathrm{i}\omega t}\mathrm{d}t \\ S_{\dot{U}_n}(\omega) &= \omega_n^2 U_n^2 S_{a_n}(\omega) \end{aligned} \tag{2.44}$$

Putting this back into equation 2.42 the kinetic energy becomes

$$\begin{aligned} \langle E_{kin}\rangle &= \frac{\rho\Gamma}{2}\int_0^L\int_0^\infty \omega_n^2 U_n^2 S_{a_n}(\omega)\mathrm{d}\omega\mathrm{d}z \\ \langle E_{kin}\rangle &= \frac{m_0 L^2}{2}\int_0^\infty \omega_n^2 S_{a_n}(\omega)\mathrm{d}\omega \end{aligned} \tag{2.45}$$

The integral can be approximated when $Q^{-1} \to 0$, and taking into account that at thermal equilibrium the average kinetic energy is $\langle E_{kin}\rangle = 1/2k_BT$ to be [50]

$$\begin{aligned} \frac{1}{2}k_BT &\approx \frac{1}{4}\frac{QL^2}{\omega_n}\frac{S_f(\omega)}{m_0} \quad \Rightarrow \\ S_f(\omega) &\approx \frac{2k_BTm_0\omega_n}{\pi QL^2} \end{aligned} \tag{2.46}$$

The expression for the spectral density of the noise displacement becomes

$$S_{a_n}(\omega) = \frac{\omega_n}{(\omega_n^2-\omega^2)^2+(\omega_n^2/Q)^2}\frac{2k_BT}{\pi m_0 L^2 Q} \tag{2.47}$$

The spectral density for different values of $Q$ is shown in figure 2.7 for a nano-scale cantilever. The amplitude noise is seen to reach a maximum at resonance in accordance with Zener's model, and off resonance the amplitude noise is decreasing with increasing $Q$-factor.

The relation between off- and on-resonance spectral density of amplitude noise can be calculated from 2.47. At resonance $\omega = \omega_n$ and the amplitude noise is

$$S_{a_n}(\omega_n) = \frac{2k_BT}{\pi m_0 L^2}\frac{Q}{\omega_n^3} \tag{2.48}$$

Off-resonance a similar expression is obtained by setting $\omega \ll \omega_n$

$$S_{a_n}(\omega)\Big|_{\omega\ll\omega_n} \approx \frac{2k_BT}{\pi m_0 L^2}\frac{1}{Q\omega_n^3} \tag{2.49}$$

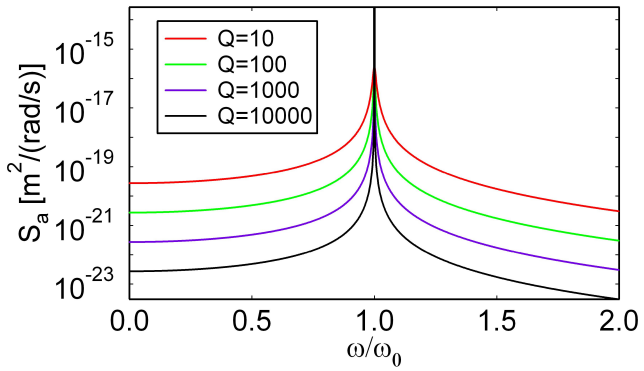


**Figure 2.7:** The thermo-mechanical spectral density of amplitude noise as a function of frequency for different values of $Q$-factor. The spectral noise is calculated for a Si cantilever with the dimensions of $w$=200nm, $h$=220nm, and $L$=3.8$\mu$m. The maximum of the spectral noise is $10^{-7}$m$^2$/(rad/s) for $Q = 1000$ but the axis has been cut off for clarity.

### Frequency noise

The obtained amplitude noise can be rephrased to a frequency noise for frequencies close to the resonant frequency by linearizing the amplitude (equation 2.32), setting

$$a_n(\omega) \approx a(\omega_n) + \alpha(\omega - \omega_n), \quad \alpha = \frac{\partial a_n(\omega)}{\partial \omega} \tag{2.50}$$

This means that the spectral density of the frequency noise can be written as

$$\begin{aligned} S_{a_n}(\omega) &\approx \alpha^2 S_\omega(\omega) \quad \Rightarrow \\ S_\omega(\omega) &\approx \frac{1}{\alpha^2} S_{a_n}(\omega) \end{aligned} \tag{2.51}$$

The derivative of the amplitude is

$$\begin{aligned} \alpha &= \frac{\partial a_n(\omega)}{\partial \omega} = \frac{m_0}{f_n} 2\omega a_n^2(\omega) \\ \alpha &\approx \frac{2\omega}{-i\omega_n^2/Q} a_n(\omega) \quad \Rightarrow \\ \alpha^2 &\approx \left(\frac{2Q}{\omega_n}\right)^2 a_n^2(\omega_n), \quad \omega \approx \omega_n \end{aligned} \tag{2.52}$$

The spectral density of the frequency noise is thereby (for $\omega/\omega_n \approx 1$)

$$S_{\omega,th}(\omega) \approx \left(\frac{\omega_n}{2Q}\right)^2 \frac{S_{a_n}(\omega)}{a_n^2(\omega_n)} \tag{2.53}$$

A similar expression is obtained by Ekinci *et al.* for a cantilever controlled with a phase-locked-loop [51].

### 2.4.2 Adsorption and Desorption Noise

A cantilever will experience noise due to interactions with the surrounding media even if no thermal energy is present in the cantilever. When individual molecules adsorb and desorb to the surface the mass will change and thereby noise will be introduced in the resonant frequency. This source of noise cannot be described using Zener's model since the processes are not dissipative [66].

It turns out that the frequency noise introduced by adsorption and desorption on a resonator is quite large [51, 65, 67]. The important parameters to consider are the desorption rate,

$$r_d = v_d e^{-\frac{E_b}{k_B T}} , \tag{2.54}$$

(considered thermally activated) where $v_d$ is the desorption coefficient and $E_b$ is the binding energy, and the adsorption rate,

$$r_a = \frac{2}{5} \frac{p}{\sqrt{m_m k_B T}} s a_{ads} , \tag{2.55}$$

where $p$ is the pressure, $s$ is the sticking coefficient, $a_{ads}$ is the area per surface site, and $m_m$ is the mass of the molecules impinging on the resonator.

An expression can be obtained for the spectral density of the frequency noise caused by adsorption and desorption processes

$$S_{\omega,A-D}(\omega) = \frac{2\pi\omega_0^2 N_a \sigma_{occ}^2 \tau_{cor}}{1 + (\omega - \omega_0)^2 \tau_{cor}^2} \left( \frac{m_m}{m_{eff}} \right)^2 \tag{2.56}$$

$$\sigma_{occ}^2 = \frac{r_a r_d}{(r_a + r_d)^2} \quad , \quad \tau_{cor} = \frac{1}{r_a + r_d} \tag{2.57}$$

where $N_a$ is the number of binding sites on the surface of the resonator with an effective mass of $m_{eff}$. The spectral density of the frequency noise is depicted in figure 2.8 for different pressures for a nano-scale cantilever. The behavior is seen to differ from that of the thermo-mechanical noise since the minimum amplitude noise off resonance is not occurring for minimum pressure (corresponding to maximum $Q$-factor) but at intermediate pressures. At resonance the minimum amplitude noise is at maximum pressure.

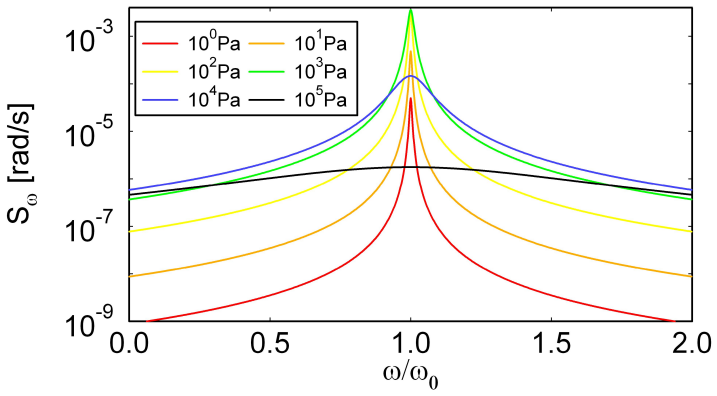


**Figure 2.8:** Pressure dependency of the spectral density of frequency noise induced by adsorption-desorption processes on a cantilever at different pressures. The calculations are on a Si cantilever with the dimensions of $w$=200nm, $h$=220nm, and $L$=3.8$\mu$m.

### 2.4.3 Total Noise

The dominating source of noise will be dependent on the geometry of the cantilever, the intrinsic $Q$-factor, and the pressure. The spectral density of the frequency noise at resonance caused by adsorption-desorption and thermo-mechanical fluctuations can be compared by looking at equation 2.53 and 2.56.

The spectral density of the frequency noise of a cantilever resonating with an amplitude in the order of the width of the cantilever $a_n \sim w$, as a function of pressure for a micro- and nano-scale cantilever is shown in figure 2.9, where the gas $Q$-factor is found from equation 2.17 in case of the nano-scale cantilever and equation 2.16 for the micro-scale cantilever.

From the figure it is seen that the thermo-mechanical noise is larger than the adsorption-desorption noise due to air-molecules. Typical frequency fluctuations due to thermo-mechanical noise at ambient conditions on a nanometer-scale cantilever is in the order of $10^8$rad/s and for a micro-scale cantilever it is $10^3$rad/s. Operating the cantilever at higher modes decreases the frequency noise due to thermo-mechanical fluctuations. If heavier gas molecules or a smaller cantilever was used, the adsorption-desorption noise would have a larger influence.

The absolute frequency noise of the cantilever is evaluated by integration of the spectral density of the frequency noise over the bandwidth, $\Delta f$, of the measurement

$$\Delta\omega_{min} = \left[\int_{\omega_0-\pi\Delta f}^{\omega_0+\pi\Delta f} S_\omega(\omega)\mathrm{d}\omega\right]^{1/2} \approx \left[2\pi\Delta f S_\omega(\omega_0)\right]^{1/2} \tag{2.58}$$

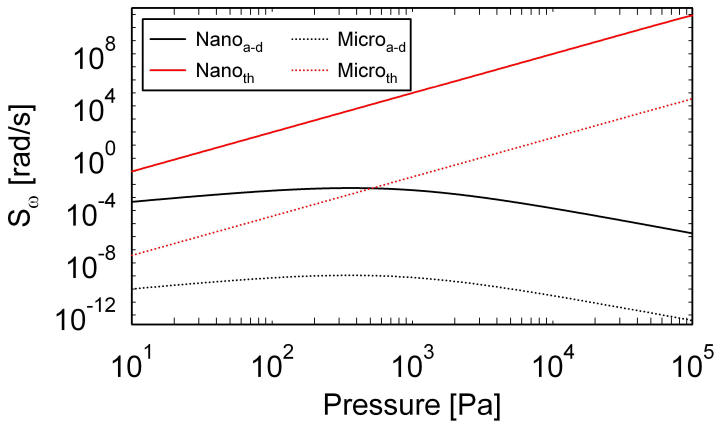


**Figure 2.9:** The spectral density of frequency fluctuations from the desorption-adsorption noise (a-d) and from the thermo-mechanical limit (th) as a function of pressure slightly above resonance ($\omega = (1 + 1/1000)\omega_0$) for a nano-scale cantilever ($w$=200nm, $h$=220nm, and $L = 3.8\mu$m) and a micro-scale cantilever ($w = 2\mu$m, $h = 2.5\mu$m, and $L = 50\mu$m).

## 2.5 Summary

In this chapter general cantilever theory relevant for cantilever based mass sensor was presented. The eigenfrequencies and mode shapes of a cantilever was found, and it was shown that the mass responsivity is a function of the resonant frequency and mass of the cantilever. To increase the mass responsivity, the cantilever needs to be fabricated in a material with a high Young's modulus, and a low density. In addition, the cantilever should also be as small as possible. The mass responsivity can be further increased by operating the cantilever at higher modes.

The final sensitivity of the cantilever based mass sensor also depends on the noise sources and the damping of the cantilever. It was found that the dominant source of dissipation on the cantilever geometries used here was thermo-mechanical damping. The absolute noise then depends on the bandwidth of the measurement. The noise from actuation and readout circuitry can also play a role.

Forces on a cantilever will change the apparent resonant frequency of a cantilever. The exact change depends on the nature of the force.

# Chapter 3

# Theory of Position and Mode Dependence

In standard cantilever based mass sensor-theory the mass is always assumed to be distributed uniformly or attached as a point mass to the end of the cantilever. This approach is not viable if single molecules or single cells are to be measured, since the change in resonant frequency is not only dependent on the mass of the attached particle, but also on the position on the cantilever as it has been shown previously by Dohn *et. al* [47]. In this section the analytical theory supporting these results will be derived.

## 3.1 Position Dependent Responsivity

Consider a cantilever with the mass $m_0$ loaded with a point mass $\Delta m$ positioned at $z_{\Delta m}$ (figure 3.1). If the mass load is much less than the cantilever mass, $\Delta m << m_0$, the cantilever mode-shape will not change significantly, thus the resonant frequency of such a system can be accurately estimated using an energy approach and the Rayleigh-Ritz theorem. According to the Rayleigh-Ritz theorem the time average kinetic energy, $E_{\text{kin}}$, equals the time average strain energy, $E_{\text{strain}}$, at resonance [68].

Assuming a small deflection and thereby neglecting shear stress, the energy of a deflected cantilever is only the energy stored due to the induced strain. For a cantilever with an attached point mass the Rayleigh-Ritz theorem means that

$$E_{strain} = E_{kin} + E_{kin,\Delta m} \tag{3.1}$$

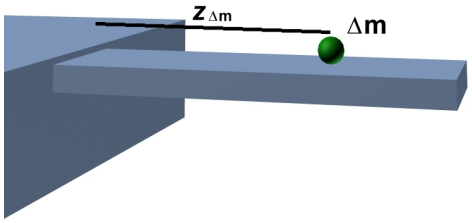


**Figure 3.1:** Schematic of a cantilever with a single bead, having the mass $\Delta m$, positioned at $z_{\Delta m}$.

The kinetic energy for the cantilever is

$$\begin{aligned} E_{kin} &= \int_V \frac{\omega_{\mathrm{n,\Delta m}}^2}{2} \rho U_n^2(z) \mathrm{d}V \\ E_{kin} &= \frac{1}{2} w h \omega_{n,\Delta m}^2 \rho_m \int_0^{\mathrm{L}} U_n^2(z) \mathrm{d}x \\ E_{kin} &= \frac{1}{2} m_0 \omega_{n,\Delta m}^2 \,, \end{aligned} \tag{3.2}$$

where $\omega_n$ is the frequency of motion, $\rho_m$ is the mass density, $U_n$ is the displacement-function of the cantilever (equation 2.4), and $n$ is denoting the modal number. The kinetic energy due to the added point mass at $z_{\Delta m}$ is

$$E_{kin,\Delta m} = \frac{1}{2} \Delta m \omega_{n,\Delta m}^2 U_n^2(z_{\Delta m}) \tag{3.3}$$

Since the mode-shape is assumed unchanged by the attached point mass the strain energy is approximately equal to the kinetic energy of the unloaded cantilever

$$E_{strain} \simeq \frac{1}{2} m_0 \omega_n^2 \tag{3.4}$$

The resonant frequency can be found from equation 3.1, 3.2, 3.3 and 3.4 to be

$$\omega_{n,\Delta m}^2 = \omega_n^2 \left( 1 + \frac{\Delta m}{m_0} U_n^2(z_{\Delta m}) \right)^{-1} \tag{3.5}$$

The corresponding mass responsivity of the cantilever caused by a point mass,

$\Delta m$, positioned at the tip of the cantilever, $z_{\Delta m} = L$, can now be found

$$\begin{aligned}\mathcal{R}_{point} &= \frac{\Delta\omega_n}{\Delta m} = \frac{\omega_{n,\Delta m} - \omega_n}{\Delta m} \\ &= \frac{\omega_n\left(\left(\sqrt{1+\frac{4\Delta m}{m_0}}\right)^{-1} - 1\right)}{\Delta m} \\ \mathcal{R}_{point} &= \frac{\omega_n}{\Delta m}\left(\left(\sqrt{1+\frac{4\Delta m}{m_0}}\right)^{-1} - 1\right) \propto C_n^2 \end{aligned} \tag{3.6}$$

Thus, the mass responsivity of a cantilever evaluated for a point mass are having the same mode dependence as the mass responsivity of a uniform distributed mass (equation 2.13).

## 3.2 Mass and Position From Responsivity

Assuming that the system at hand is perfectly known, i.e. the cantilever mass, $m_0$, and native resonant frequencies, $\omega_n$, of several bending modes of the unloaded cantilever, it is possible to determine the mass of an attached single particle (cell or molecule) and it's position by measuring the resonant frequencies, $\omega_{n,\Delta m}$, of the loaded cantilever. Solving equation 3.5, for the mass ratio we find

$$\frac{\Delta m}{m_0} = \frac{1}{U_n^2(z_{\Delta m})}\left(\frac{\omega_n^2}{\omega_{n,\Delta m}^2} - 1\right), \tag{3.7}$$

The concept can be visualized by plotting $\Delta m/m_0$ from equation 3.7 for a few bending modes. In figure 3.2 this is performed for the first four modes using $\omega_{n,\Delta m}$ from equation 3.5 assuming a mass of $\Delta m = 1/100 m_0$ at three different positions $z_{\Delta m}/L = \{0.3, 0.5, 0.8\}$. The position where all curves are crossing, gives the position and mass. From this theoretical example it is seen that the solution is indeed unique and the crossing corresponds to the positions of $z_{\Delta m}/L$.

The implication of the theory is that by measuring the resonant frequency for the first 3-4 modes of an unloaded cantilever, and repeating this when the cantilever is loaded with a single particle or cell, the position can be found with high accuracy. If $N$ modes, $n = 1, 2 \ldots N$, are measured, then $N$ equations similar to equation 3.7 with identical left hand sides results. A practical procedure for finding the position of the attached particle could be to eliminate $\Delta m/m_0$ and then estimate the most

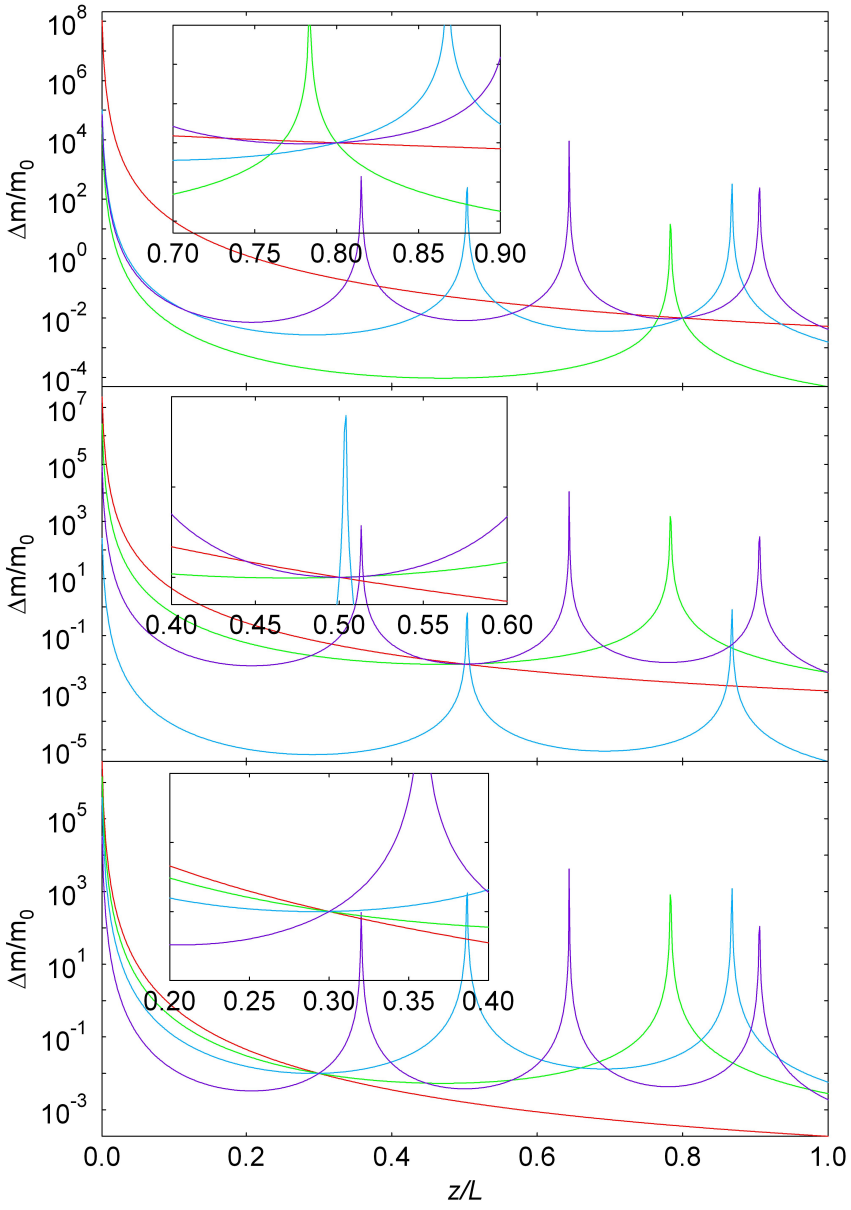


**Figure 3.2:** The calculated ratio of $\Delta m$ to $m_0$ for the first four modes as a function of position, $z$ in units of the length, $L$. Plots have been made for three different positions $z_{\Delta m}/L = \{0.3, 0.5, 0.8\}$ and the mass of the particle is set to $1/100 m_0$. The insets show a closeup of the crossing point.

probable position $\tilde{z}_{\Delta m}$ that minimizes

$$\sum_{n,i}\left(\frac{U_n^2(z_{\Delta m})}{U_i^2(z_{\Delta m})}-\frac{\left(\frac{\omega_n^2}{\omega_{n,\Delta m}^2}-1\right)}{\left(\frac{\omega_i^2}{\omega_{i,\Delta m}^2}-1\right)}\right)^2 \tag{3.8}$$

The corresponding variance is $\sigma_z^2=\sum_{n,i}(z_{n,i}-\tilde{z}_{\Delta m})/(N_{n,i}-1)$, where $z_{n,i}$ minimizes each term of equation 3.8. Finally, solve equation 3.7 with $\tilde{z}_{\Delta m}$ for each mode to find $(\Delta m/m_0)_n$, whereby the most probable value of the attached mass is

$$\frac{\tilde{\Delta m}}{m_0}=\frac{\sum_n\left(\frac{\Delta m}{m_0}\right)_n}{N} \tag{3.9}$$

with the corresponding standard deviation $\sigma_m^2=\sum_n\left[(\Delta m/m_0)_n-\tilde{\Delta m}/m_0\right]^2/(N-1)$. In a practical measurement system, the functions $U_n^2(z_{\Delta m})/U_i^2(z_{\Delta m})$ could be tabulated for ease of evaluation.

To estimate the mass of the attached particle or cell it is necessary to know the mass of the cantilever. The mass of the cantilever can often be estimated from the design dimensions and materials used in fabrication with an uncertainty on the order of a few percent. This will cause the uncertainty in the calculation of the mass of the attached particle to be small as well.

# Chapter 4

# Theory of Hard Contact Readout

The minimum measurable change in resonant frequency, $\Delta\omega_{\text{min}}$, is determined by the noise sources of the system as described in section 2.4. In most applications the noise introduced by the measurement system, $\Delta\omega_{\text{sys}}$, is significant, and in order to reduce this to a minimum it is important that the primary conversion of frequency to an electrical signal results in a large signal. By doing this the unavoidable electronic noise is unimportant in comparison to the other noise sources of the cantilever.

The hard contact method is one such method, since a quite high dc current level ($I \sim 1\mu\text{A}$) is the primary electrical output signal. This is a much much higher current level than seen in electron tunneling detection schemes where $I \sim 1\text{pA}$ [69].

## 4.1 Principle

A schematic of the detection set-up used for hard contact readout is shown in figure 4.1. The cantilever is grounded and actuated by the actuation-electrode using the signal $V_{\text{A}} = V_{\text{A},ac} + V_{\text{A},dc}$ as in ordinary electrostatic actuation setups [33]. Close to the apex of the cantilever an electrode biased through an integrating amplifier with $V_{\text{E}}$ is placed such that the cantilever is capable of hitting the electrode.

The principle behind the hard contact method is depicted in figure 4.2. At sufficiently large vibrational amplitudes the cantilever and electrode contact once every cycle and a unidirectional current pulse train, $I_{\text{in}}(t)$, with a pulse width of $t_{\text{c}}$, and a magnitude of

$$I_{\text{in}} = -\frac{V_{\text{E}}}{R_{\text{C}}}\,, \tag{4.1}$$

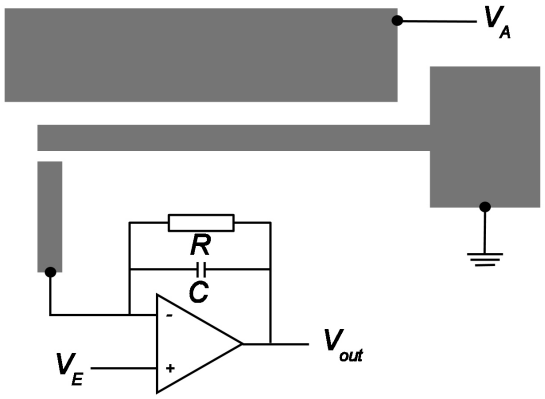


**Figure 4.1:** Schematic of the hard contact readout. The cantilever is grounded and electrostatically actuated using $V_A$ on the actuation-electrode. The readout-electrode is biased by $V_E$ through the integrating amplifier in which a capacitor $C$ determines the amplification and the resistor $R$ discharges the capacitor to obtain a steady-state signal.

is supplied to the amplifier input. $R_C$ is the total resistance of the contact since the resistance of the device can be neglected if high conductivity metals are used (resistivity $\sim 2\ \mu\Omega$cm). The unidirectional current train will be integrated and the output signal from the amplifier is

$$V_o = \frac{1}{C}\int I_{in} dt, \tag{4.2}$$

which in this case is a staircase voltage. If no resistor is put in parallel, the output voltage will rise as long as the input current is supplied. By using the resistor, $R$, the capacitor will discharge and a steady state output voltage will be reached. At steady state the amplifier output voltage reaches a value of

$$V_{o,ss} = V_E - R\overline{I_{in}} = V_E + \frac{R}{R_C}\frac{t_c}{T}V_E\,, \tag{4.3}$$

where $\overline{I_{in}}$ is the time average of the input current, and $T$ the cycle time.

The principle of the hard contact readout is depicted in the frequency domain in figure 4.3 for three different levels of actuation. When the amplitude exceeds a critical value, equal to the equilibrium cantilever to electrode distance, a current will flow. This occurs in a wide frequency span, $\Delta f$, at high cantilever excitation energy and in a narrower frequency span at a lower excitation energy. The reciprocal relative frequency resolution, $f_0/\Delta f$, thereby serves as a convenient measure of the quality of the measurement, and by tuning the actuation energy it is possible to increase this quality.

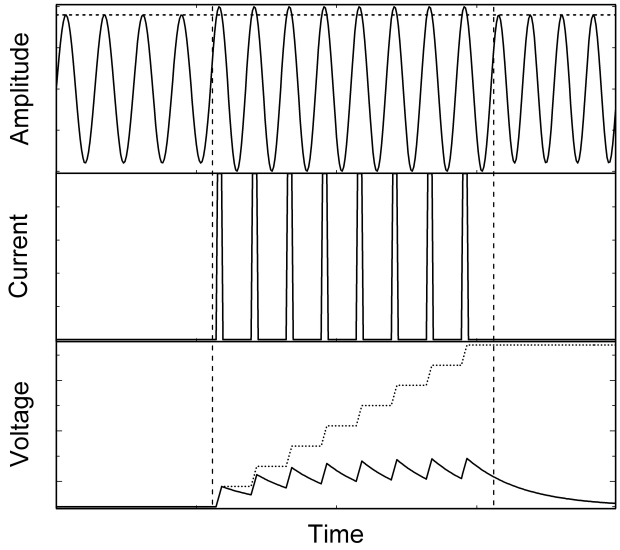


**Figure 4.2:** The principle of hard contact readout in the time domain. When the amplitude is larger than or equal to the distance to the biased readout-electrode, a current will flow. When vibrating this will result in a unidirectional current pulse train in the circuit. This current is integrated and turned into a staircase voltage in the amplifier (dotted line). By putting in a large resistor the capacitor is discharged and a steady-state output voltage is obtained.

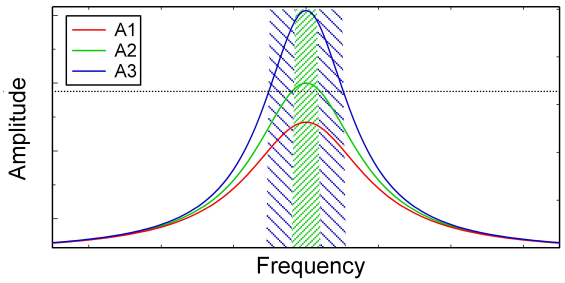


**Figure 4.3:** The principle of hard contact readout in the frequency domain. Three amplitude functions with the same $Q$-factor but different excitation energy levels are sketched. When the amplitude exceeds a critical value (dotted line) equal to the equilibrium cantilever to electrode distance a current will flow. This occurs in a wide frequency span at high cantilever excitation energy (A3 and sparsely hatched area) and in a narrower frequency span at lower excitation energy (A2 and densely hatched area). By tuning the actuation energy it is possible to make a current flow in a very narrow frequency span.

## 4.2 Sticking

In all MEMS or NEMS where contact between surfaces is required or unavoidable, sticking is of serious concern. Assuming that the distance between the readout-electrode and the cantilever is $d_{ec}$, the non-stick condition for the hard contact readout method is that the elastic energy stored in the deflected cantilever exceeds the adhesive energy of the contact area.

The elastic energy of a cantilever deflected the distance $d_{ec}$ is

$$\begin{aligned} E_{strain} &= \frac{1}{2}ky^2 = \frac{3}{2}\frac{EId_{ec}^2}{L^3} \\ E_{strain} &= 8Ewd_{ec}^2\left(\frac{w}{L}\right), \end{aligned} \tag{4.4}$$

The adhesive energy due to a contact area, $A_C$ is $A_C E_{adh}$. $E_{adh}$ depends strongly on the mechanisms involved in the adhesion, but in worst case, where chemical bonds are formed, the order of magnitude is $E_{adh} \sim 1$ J/m$^2$ [70]. These considerations lead to the geometrical design rule

$$\left(\frac{w}{L}\right)^3 \frac{hd_{ec}^2}{A_C} > 8\frac{E_{adh}}{E}, \tag{4.5}$$

that must be fulfilled to unconditionally avoid sticking. For simplicity, a stiction coefficient, $\lambda_{stick}$, can be defined as

$$\lambda_{stick} = \left(\frac{w}{L}\right)^3 \frac{hd_{ec}^2}{8A_C}\frac{E}{E_{adh}} > 1 \tag{4.6}$$

Assuming a blunt wedge like electrode in contact with the cantilever in the full thickness of the cantilever, such that $A_C = h\ell$, the length, $\ell$, of the contact region must scale linearly for linear geometrically scaled devices in order to keep fulfilling the non-stick condition. This pose no problems since the better lithographic tools required to fabricate the devices also improve the wedge sharpness.

## 4.3 Contact-resistance and Contact-time

The average current measured with hard contact readout method depends on the ratio of contact time to cycle time, and the contact resistance. Thus, these parameters are important when considering the scaling behavior of the method.

Assuming $N$ coherent electron channels are formed in the contact, the contact resistance can be estimated to be [71]

$$R_C = \frac{h_p}{2e^2N} \approx 13\ \text{k}\Omega/N, \tag{4.7}$$

where $h_p$ is Planck's constant, and $e$ is the unit charge. The number of electron channels is probably affected by scaling and in an ultimate scaled device a single channel is assumed to remain, which still results in a useful low resistance.

The ratio of contact time to cycle time can be modeled by a phonon- and a mode shape-approach. Looking at the phonon-approach it is assumed that at the time of impact a phonon wave packet will be created at the boundary between the cantilever and the electrode. This phonon wave packet will travel across the cantilever, hit the opposing sidewall and be reflected. If the non-stick condition is fulfilled, the cantilever will free itself from the electrode when the phonon returns to the contact area. The contact time $t_C$ is then given by

$$t_C \simeq \frac{2w}{v_{phonon}}, \tag{4.8}$$

where $v_{phonon}$ is the phonon velocity in the cantilever. Typical values of the contact time for a micro-scale cantilever will be in the order of 0.5-1ns. The cycle time scales inversely with the width, thus the ratio of contact time to cycle time scales with the square of the width $t_c/T \propto w^2$.

Turning to the mode-shape approach, the cantilever motion during the contact time $t_C$, is described by a superposition of modes for a pinned cantilever (can be assumed to be a bridge structure) and a free cantilever. The resonant frequency for a bridge structure is $\omega_{bridge} \approx 5\omega_{cant}$ depending on the mode of operation. Assuming the contact is only for a single cycle and that no higher order modes are excited the ratio of contact time to cycle time is

$$\frac{t_C}{T} \approx \frac{\omega_{cant}}{\omega_{bridge}} = \frac{1}{5}, \tag{4.9}$$

which increases slightly for higher modes. It follows, that the contact time, $t_C$, scales with geometry and material parameters exactly as the cycle time, $T$, does, and as a result the ratio of these is unaffected by geometrical scaling. However, it is highly unlikely that no higher order modes are excited, and the change of exciting higher modes increases with the kinetic energy of the cantilever at the time of impact. If higher modes are excited the ratio will decrease, but the effect is not affected by scaling so the conclusion is still valid.

# Chapter 5

# Design and Fabrication

To test the theoretical predictions presented in chapter 4 on hard contact readout a set of cantilever structures with readout and actuation electrodes needed to be designed and fabricated. Two different fabrication techniques were chosen: UV-lithography and electron beam lithography. The major difference is the minimum feature size accomplishable and thereby the line-pitch - and price of fabrication. The UV-lithography was chosen for the feasibility study, whereas electron beam lithography was only to be used for the final testing of nano-scale cantilevers.

In the following sections the design considerations will be discussed before the final processes are presented. The fabricated cantilevers are made in one of two different materials: Silicon-dioxide ($SiO_2$) and Silicon (Si). The $SiO_2$ cantilevers were fabricated using UV-lithography, whereas the Si cantilevers were fabricated using electron beam lithography.

## 5.1 Design Considerations

The important parameters to consider during the design phase are the width, the resonant frequency and the coating of the cantilever as well as the matter of stiction.

The lower limit to the width of the cantilever is given by the method of lithography. In the case of UV-lithography a line-pitch of 1.5-2$\mu$m is achievable by standard process parameters, where the line-pitch in the case of electron beam lithography is roughly a factor of 10 less, i.e. 150-200nm by standard processing. These numbers have been used in the design of the cantilever based mass sensors to dictate the cantilever width. Pushing this limit can cause difficulties in the fabrication and testing of the device.

The resonant frequency is given by equation 2.11, and scales linearly with the width and quadratically with the inverse length. The maximum resonant frequency is dictated by the maximum frequency of the actuation electronics and the capability of the readout circuitry.

The design rule for sticktion is given by equation 4.5 and a stiction coefficient, $\lambda_{\text{stick}}$, above 1 must be designed for. The important design parameter is the ratio between the width and the length that needs to be as high as possible, with the above considerations in mind. Also, it should be possible to actuate the cantilever to have an amplitude equal to the cantilever-electrode distance, meaning that a low spring constant is desirable.

A high conductivity metal coating needs to be applied to the cantilevers to ensure a low contact resistance and low total resistance of the device. The metal should be hard to oxidize. The coating needs to be applied to the sidewalls of the cantilever. For this three different techniques can be used: 1) deposition during sweep of the sample, 2) deposition while the sample is tilted, or 3) deposition by sputtering. To ensure a stable contact a minimum thickness of the metal must be in the order of nanometers.

### 5.1.1 Design for UV-lithography

Two different UV designs were used in the experiments, both having the same fabrication process. The first generation, UV-type A, is schematically shown in figure 5.1a. In this design several parameters were varied and these are shown in the figure as well.

**Length** $L = \{20, 60, 100\}\mu$m. The difference in lengths allow for wide spread in resonant frequencies and spring constants.

**Actuator-cantilever distance** $d_{ac} = \{1, 1.5, 2\}\mu$m. The distance must be as small as possible to give maximum actuation force, but still leave room for the cantilever to hit the electrode.

**electrode-cantilever distance** $d_{ec} = \{0, 1, 1.5\}\mu$m. Must be as close as possible to the cantilever to avoid non-linear behavior, but the distance should be sufficient to avoid sticktion.

**electrode tip angle** $\theta = \{60, 90\}^{\circ}$. During fabrication a low angle will cause the electrode-cantilever distance to increase, but the electrode needs to have a small contact area.

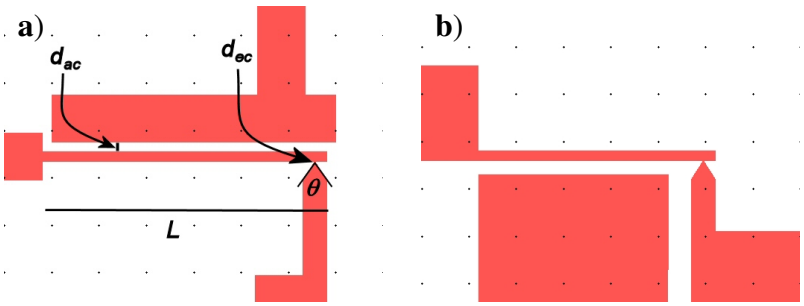


**Figure 5.1:** The design for fabrication of cantilevers using UV-lithography. UV-type A (a) and UV-type B (b). The distance between grid-points is 10$\mu$m.

| Type | $L$ [$\mu$m] | $w$ [$\mu$m] | $h$ [$\mu$m] | $f_0$ [kHz] | $f_{\text{coat}}$ [kHz] | $\lambda_{\text{stick}}$ |
|---|---|---|---|---|---|---|
| A (20) | 20 | 2 | 2.5 | 4555 | 3986 | 18 |
| A (60) | 60 | 2 | 2.5 | 506 | 443 | 0.65 |
| A (100) | 100 | 2 | 2.5 | 182 | 159 | 0.14 |
| B | 50 | 2 | 2.5 | 729 | 638 | 1.1 |

**Table 5.1:** Design dimensions of the devices based on UV-lithography together with the theoretical resonant frequency with and without a Pt coating. The sticktion coefficient is calculated for an amplitude equal to the width and a contact area of $A_c = wh$.

The width was kept fixed at $w = 2\mu$m, whereas the height of the cantilever, $h$, was given by the cantilever substrate thickness.

The design dimensions of devices are listed in table 5.1. Also, the resonant frequency for the first mode is given together with the sticktion coefficient for an amplitude equal to the width of the cantilever (equation 4.6). For the sticktion coefficient it is assumed that the contact area is $A_c = wh$. The resonant frequency for the coated cantilever is with a coating of 35nm Platinum (Pt) on the sides and 70nm Pt on the top. The details on how to calculated the spring constant of a coated cantilever are shown in appendix B.

The sticktion coefficients of UV-type A with lengths of 100$\mu$m and 60$\mu$m indicate that sticktion will occur if contact is formed between the cantilever and readout-electrode. During the initial testing of the devices sticktion was indeed observed when the cantilever was pushed into contact with the readout-electrode. However, no stikction was observed during operation with moderate amplitudes in the case of UV-type A with a length of 60$\mu$m.

From the first processing results and initial measurements, optimal parameters were chosen and a second generation design was made. For the second generation UV design, UV-type B, the position of the readout-electrode was changed to avoid

snap-in of the cantilever to the actuation-electrode (figure 5.1b). The length was reduced to minimize the risk of sticktion to $L = 50\mu$m while the electrode-tip angle was set to $\theta = 60^{\circ}$. Still the electrode-cantilever distance was varied $d_{ec} = \{0, 0.5\}\mu$m with a fixed actuator-cantilever distance of $d_{ac} = 2\mu$m.

### 5.1.2 Design for Electron Beam Lithography

Two different designs have been made for electron beam lithography and are schematically shown in figure 5.2. The major difference between the two is the shape of the readout electrodes, one design having a blunt readout-electrode and the other design having a pointed. The design differentiates itself from the UV-design by having two readout electrodes for each cantilever positioned close to the apex on either side. This was done to double the number of contacts every cycle of the cantilever, thereby maximizing the current flowing during operation.

The width of the cantilever is designed to be $w = 200$nm with a length of $L = 3.8\mu$m. The distance to the electrode is $d_{ec} = \{100, 200, 300\}$nm for the blunt electrodes and $d_{ec} = \{125, 225\}$nm for the pointed electrodes.

The design dimensions of devices are listed in table 5.2. Also, the resonant frequency for the first mode is given together with the sticktion coefficient for an amplitude equal to $d_{ec}$ (equation 4.6). For the sticktion coefficient it is assumed that the contact area is $A_c = wh$ for the blunt electrodes and $A_c = wh/5$ for the pointed electrodes. The resonant frequency for the coated cantilever is with a coating of 5nm Pt on the sides and 17nm Pt on the top.

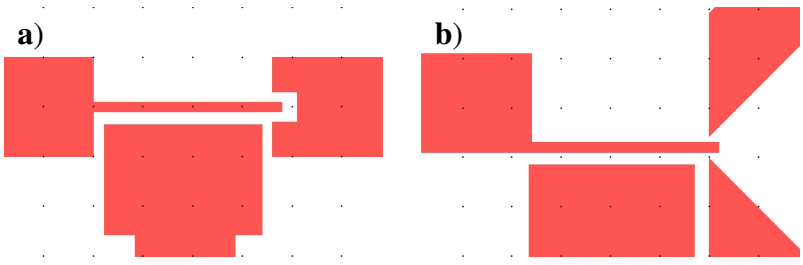


**Figure 5.2:** The design for fabrication of cantilevers using electron beam lithography. Versions with blunt electrodes (a) and pointed electrodes (b) have been designed. The distance between grid-points is $1\mu$m.

| Type | $L$ [$\mu$m] | $w$ [$\mu$m] | $h$ [$\mu$m] | $f_0$ [kHz] | $f_{coat}$ [kHz] | $\lambda_{stick}$ |
|---|---|---|---|---|---|---|
| $EB_{p,125}$ | 3.8 | 0.20 | 0.22 | 18.5 | 12.4 | 1.1 |
| $EB_{p,225}$ | 3.8 | 0.20 | 0.22 | 18.5 | 12.4 | 3.7 |
| $EB_{b,100}$ | 3.8 | 0.20 | 0.22 | 18.5 | 12.4 | 0.15 |
| $EB_{b,200}$ | 3.8 | 0.20 | 0.22 | 18.5 | 12.4 | 0.58 |
| $EB_{b,300}$ | 3.8 | 0.20 | 0.22 | 18.5 | 12.4 | 1.3 |

**Table 5.2:** Design dimensions of the devices based on electron beam lithography together with the theoretical resonant frequency with and without a Pt coating. The subscript refers to the electrode design, where *p* indicates pointed whereas *b* indicates blunt.

## 5.2 Process

Two different processes will be described in the following. The process for creating $SiO_2$ cantilevers and the process for Si cantilevers. The major difference between the two processes is that no wet-chemistry is involved in the fabrication of $SiO_2$ cantilevers whereby sticktion during processing is of no concern.

The process for metal coating of the finished structures is the same for both cantilever materials, and is covered in the final section.

### 5.2.1 Silicon-dioxide Cantilevers

The process sequence for cantilevers fabricated in $SiO_2$ is shown in figure 5.3. The starting point of the process is a $Si/SiO_2$ substrate with a 2.7$\mu$m thermally grown oxide layer, on which a standard AZ5214e-resist is spun to a thickness of 1.5$\mu$m (a). The negative pattern is defined in the resist using UV-lithography (b), and Al is deposited to a thickness of 400nm (c). After a lift-off process the oxide top layer is etched by AOE creating nearly vertical sidewalls (d). The Structures are released by RIE (e) and subsequently the structure sidewalls are coated with metal (f). Details of the process such as process parameters are listed in Appendix C.

The release of the cantilevers was performed by RIE, designed for highly anisotropic dry etches. In a standard RIE-process the undercut (etchant of structure sidewalls underneath the etch-mask) of a structure is in the the order of 1-5% of the total etch-depth. Applying this for the release of the cantilevers an etch time of minimum 100min would be required with a total etch depth of 20-100$\mu$m. Instead, a 10min an-isotropic etch is followed by a 5min isotropic etch, releasing the structures completely.

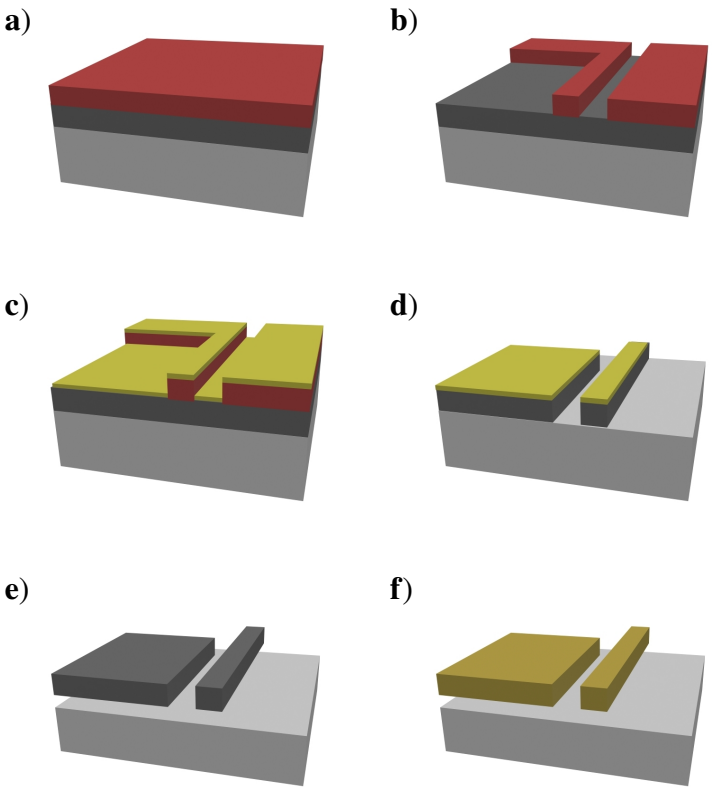


**Figure 5.3:** Process sequence steps for a $SiO_2$ cantilever. Using a simple lift-off process, the resonator pattern is defined in Al (a-c) and etching the structure by AOE the device is formed (d). The release is performed by RIE of the underlying Si substrate (e) and the device sidewalls are covered with metal (f).

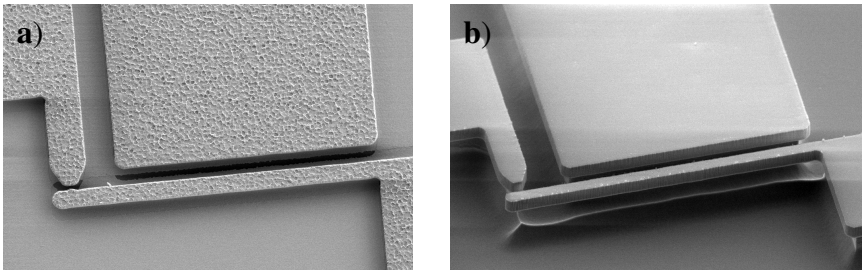


**Figure 5.4:** Two SEM images of finished $SiO_2$ cantilevers. In (b) the release of the cantilever is clearly seen.

Two SEM images of the resulting cantilevers are seen in figure 5.4. The rough top surface of figure 5.4a (similar to that of figure 8.10a) is due to an Al etch mask that was too thin to withstand the AOE etching process and it increases the surface area of the cantilever, which is desirable for gas-detection [72]. In figure 5.4b the release of the cantilever is clearly seen. Typical undercuts of the etch-mask is in the order of 1-5% of the etch-depth, giving a device width of 1.9$\mu$m after processing and before metal-coating.

### 5.2.2 Silicon Cantilevers

The process sequence for cantilevers fabricated in Si are shown in figure 5.5. Only electron beam lithography was used for the fabrication on a commercial available Si on insulator (SOI) wafer having a top-silicion layer thickness of 220nm and a buried oxide (BOX) layer of 400nm. The SOI substrate is diced in squares of 100mm$^2$ on which a standard ZEP520 positive electron beam resist mixed 1:1 with anisole is spun to a thickness of approximately 100nm (a). The negative pattern is defined in the resist using the electron beam writer (b), and Al is deposited to a thickness of 30nm (c). After a lift-off process the top Si layer is etched by RIE creating nearly vertical sidewalls (d). The structures are released by etching the $SiO_2$ in BHF and without allowing the chip to dry, transferring it to acetone and subsequently standard AZ5214e resist (e). After spinning and baking, the resist is removed in an oxygen plasma and the devices are thereby released (f). Subsequently, the structure sidewalls are coated with metal (g). Details of the process such as process parameters are listed in Appendix D.

The entire structure including bondpads has been written with the electron beam writer. In a SOI structure where the top Si-layer has a large sheet resistance due to low doping and/or thin Si-layer, exposure of large structures can cause the resist to boil, due to the joule heating associated with the large current in the area. This will change the properties of the resist in an area around the large structures and removal of the resist will be impossible with standard solvents. Images of such areas are shown in figure 5.6. The solution to the problem is to evaporate a thin layer of Al on top of the resist. The Al will make it easier for the electrons to diffuse and cool the exposed areas slightly. With a 15nm Al layer evaporated by thermal evaporation on top of the resist a significant reduction of the effect has been seen. A drawback of the Al layer is a small scattering of the electrons causing a minor smearing of the mask features.

To release the cantilever structures a resist-release process is used [73] reducing the risk of stiction significantly. After etching the BOX-layer using BHF and subsequent rinsing with water, the chip is transferred to acetone without allowing the chip to dry. The chip is rinsed thoroughly with acetone, and by gradually

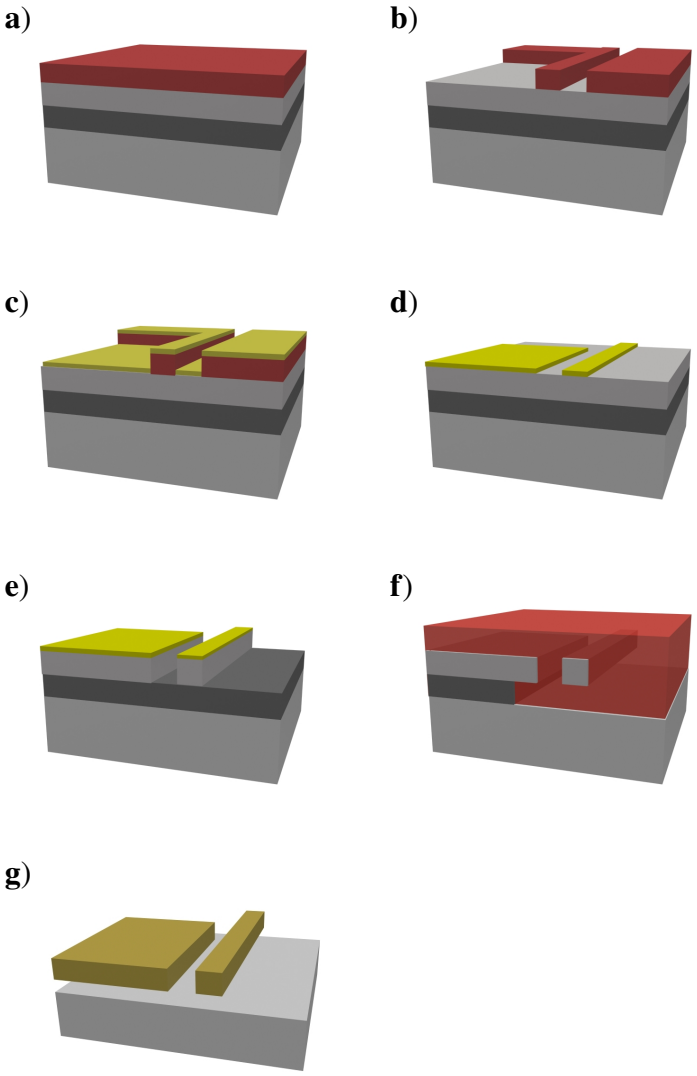


**Figure 5.5:** Process sequence steps for Si cantilevers. Using a simple lift-off process, the resonator pattern is defined in Al (a-d) and etching the structure by RIE the device is formed (e). The release is performed using a resist-release process, where the $SiO_2$ is etched using BHF and the chip is transferred to a photo-resist without allowing it to dry (f). The structures are released by exposing the resist to an oxygen plasma, whereafter the sidewall are coated with metal (g).

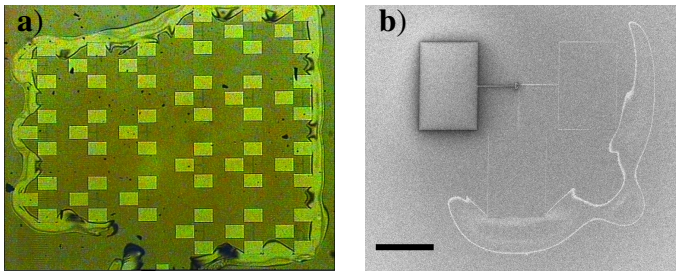


**Figure 5.6:** The effect of charging and heating during electron beam exposure over a large area on a SOI wafer with a thin Si layer (a) and a closeup SEM image of a finished structure (b). The effects is seen around large structures such as bondpads, and removal of the resist is impossible using the standard lift-off process

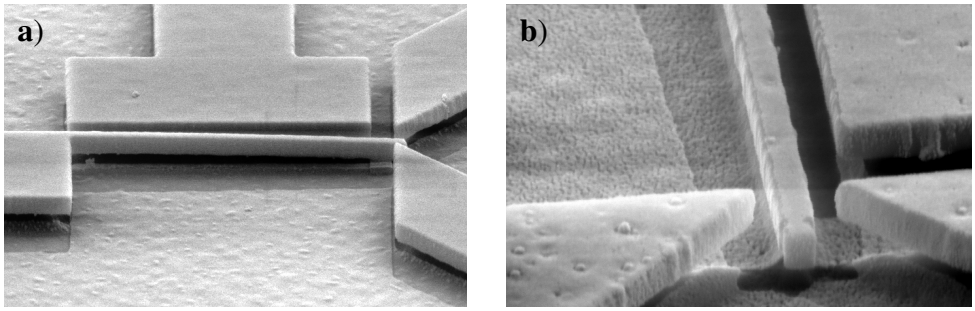


**Figure 5.7:** Two SEM images of finished Si cantilevers produced in single crystalline Si using electron beam lithography. The final cantilever width is 200nm.

exchanging the acetone with AZ5214e resist the structures are encapsulated in resist. Next, the chip is soft-baked and the structures can be released by exposing the chip to an oxygen plasma.

Two SEM images of the resulting cantilevers are seen in figure 5.7. Typical undercuts of the etch-mask is in the order of 1-5% giving a device width of 190nm after processing but before metal-coating.

### 5.2.3 Metal Coating

The metallization of the sidewalls has been performed in several ways: 1) electron beam deposition of metal during sweep of the sample, 2) electron beam deposition while the sample is tilted, and 3) deposition by sputtering.

**Sweep deposition** Deposition is performed while the chip is moved back and forth above the metal source. The movement is perpendicular to the can-

tilever length-direction, whereby metal molecules will hit the sidewalls of the cantilever.

**Tilted deposition** The chip is fixed on a metal holder tilted an angle of 30˚or 45˚to the normal deposition direction. The chip is aligned so the deposition occurs perpendicular to the sidewalls of the cantilever, and the deposition is repeated to cover both the cantilever and readout-electrode sidewalls.

**Sputtering** The sputtering is performed without sweep or tilt of the chip, since the sputtering creates a very isotropic coverage on the target chip. With a standard deposition the sidewall and top thickness are comparable in size.

All the different chips and coatings are summarized in table 5.3, where also the 2p resistance measured with a distance of 0.9mm between probes is listed. The different coatings will be described in detail in the following.

| Chip | Mode | Coating | Thick. [Å] | Rate [Å/s] | R [Ω] |
|---|---|---|---|---|---|
| 1 | Sweep | Ti/Au | 200/500 | 2/5 | 14 |
| 2 | Sweep | Ti/Au | 200/1000 | 2/10 | 7-8 |
| 3 | Sweep | Ti/Au | 200/2000 | 2/10 | 4-5 |
| 4 | Sweep | Ti/Au | 200/2000 | 2/5 | 3-4 |
| 5 | Sweep | Ti/Au | 200/5000 | 2/10 | 3-4 |
| 6 | Sweep | Ti/Pt | 200/2000 | 2/5 | 14 |
| 7 | Sweep | Ti/Pt | 200/2000 | 2/10 | 20 |
| 8 | Sweep | Ti/Pt | 200/3000 | 2/10 | 13-15 |
| 9 | 45˚ | Ti/Au | 100/500 | 2/10 | - |
| 10 | 45˚ | Ti/Au | 100/1000 | 2/10 | - |
| 11 | 45˚ | Ti/Pt | 100/500 | 2/10 | - |
| 12 | 30˚ | Ti/Au | 100/500 | 10/10 | 25-30 |
| 13 | 30˚ | Ti/Au | 100/1000 | 10/10 | 6-7 |
| 14 | 30˚ | Ti/Pt | 100/500 | 10/10 | 10 |
| 15 | 30˚ | Ti/Pt | 100/1000 | 10/10 | 9 |
| 16 | Sputter | TiW | 500 | 2 | 15-20 |
| 17 | Sputter* | TiW | 500 | 0.07 | 15-20 |

**Table 5.3:** Coating and deposition methods for the various chips produced in $SiO_2$. Chip 1-15 is metal coated by electron beam deposition of the metal, and the 'Mode' refers to the deposition mode. *R* is the 2p-resistance between 2 devices. Chip 16 was short circuited between substrate and bondpads, whereas metal was sputtered on chip 17 using the collimator.

The electron beam deposition has been performed using an Alcatel*SCM600* with a deposition rate of 2-10Å/s. Gold (Au) has been used as well as Pt, both with an adhesion layer of Titanium (Ti). The slow deposition rate was used to increase the sidewall metal thickness during sweep deposition and to minimize the built-in stress in the metal film. With sweep mode a total metal thickness of 50nm-300nm have been tested and for tilted deposition on UV-cantilevers a metal thickness of 50-100 (×2), whereas for EB-cantilevers a metal thickness of 10nm Au/Pt on 10nm Ti (×2) have been used.

SEM images of electron beam coated cantilevers fabricated in $SiO_2$ are seen in figure 5.8a-c. In part (a) a cantilever with metal deposited at an angle of 30˚is shown. Areas and edges can be seen on the substrate surface originating from the shadow-effect caused by the structures. From these 'shadows' it is possible to measure the bending of the cantilever due to the built-in stress of the deposited metal or see if the cantilever is not fully released. A cantilever coated at an angle of 45˚is shown in part (b) with a closeup of the contact area on the cantilever in part (c). It can be seen that the entire contact area is not coated with metal, but has been shaded by the nearby electrode, and deposition at angles of 45˚was generally avoided.

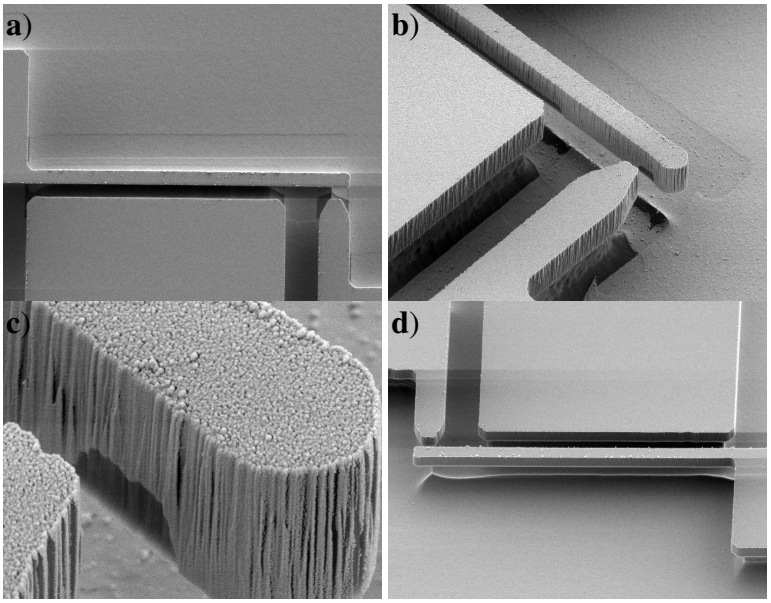


**Figure 5.8:** SEM images of cantilevers with metal deposited by electron beam deposition and sputtering. 30˚deposition (a), 45˚deposition (b), a closeup of the contact area in case of 45˚deposition (c), and sputter coated (d).

The deposition thickness on the sidewalls is easy to calculate in the case of the tilted deposition, from the total deposition thickness and the deposition angle. In the other cases the metal layer on the sidewalls will be very thin compared to that on the top, but the precise ratio is very difficult to measure.

The sputtering has been performed with a target of Titanium-Tungsten (TiW) in a Wordentec*QCL800*. This particular material was chosen since it has proven very wear-resistant, hard to oxidize and relative cleanroom compatible [74]. The metal was sputtered with power=150W and pressure=$1.310^{-2}$mbar. With a standard sputter-deposition the metal will also cover the backside of the cantilever, and thereby short-circuit the electrodes and make operation of the cantilever impossible (chip 16 in table 5.3). A special collimator has been fabricated consisting of a 2cm thick metal honeycomb structure with hole diameters of 3mm. It is placed between the sputtering target and the chip thereby reducing the deposition rate about 95%, but eliminates the deposition on the backside of the structures. A total thickness of 50nm of TiW has been deposited. SEM images of a sputter-coated cantilever fabricated in $SiO_2$ is seen in figure 5.8d. On the substrate surface no effects of shading can be seen, as was the case of the tilted deposition.

## 5.3 Summary

The design considerations and a process for fabricating devices to test the hard contact readout method were presented.

Several design considerations have been listed and the most important is related to the sticktion of the cantilever to the readout-electrode. The ultimate limit on the width of the cantilever is given by the limit to the lithography technique. Both standard UV-lithography and electron beam based lithography have been used, with either a 2$\mu$m or 200nm designed width of the cantilever. The ratio of length to width of the cantilever has to be designed in accordance with the design rule to avoid sticktion during operation.

Two different cantilever materials have been used, and standard processing techniques have been applied to fabricate the final devices. Issues regarding process-related sticktion were solved using a resist-release process, and observed effects caused by heating of the electron beam resist were solved using a thin Al layer on top of the resist during electron beam exposure.

The metal coating of the cantilever sidewalls as well as the readout-electrode was solved using three different techniques: 1) deposition during sweep of the sample, 2) deposition while the sample is tilted, or 3) deposition by sputtering.

# Chapter 6

# Experimental Setup

The experimental setup used in the various measurements is described in the following sections. This chapter is divided into three sections covering the equipment used for measuring the position dependent responsivity, characterizing the hard contact readout, and manipulating beads on the surface of cantilevers.

## 6.1 Position and Mode Dependence

The setup used for measurements on the position specific responsivity of cantilever based mass sensor consists of three parts: Actuation, readout and an environmental chamber. The entire setup has been fabricated by Ph.D. Rasmus Sandberg [75, 76]. In the following sections the different parts will be presented.

The cantilevers used for the experiments were processed by Danchip cleanroom technicians from a fabrication recipe developed by Petersen *et al.* [77]. The cantilevers was fabricated in $SiO_2$ on a Si base, and a Ti/Au coating of 10/100nm is applied after processing. No actuation or readout mechanism is designed on the chip, and the cantilevers are ordered in arrays on a single chip, where either the width or the length is varied.

### 6.1.1 Actuation

The cantilevers used in the experiment were actuated externally by a piezo-actuator (figure 6.1a). The piezo-actuator is a Noliac A/S piezo-electric ceramic linear transducer element (PZT), which expands when a voltage is applied to opposing sides. The cantilever chip is glued to a printed circuit board (PCB) (figure 6.1b),

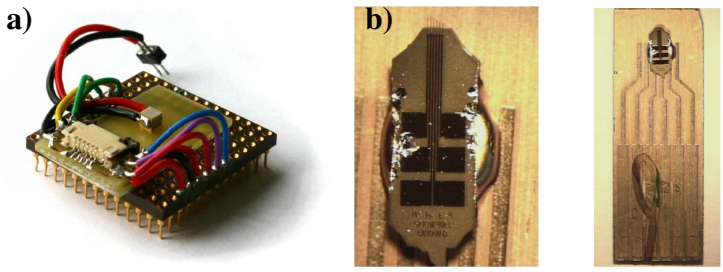


**Figure 6.1:** Piezo-actuator used for external actuation of cantilevers (a) and a PCB with a cantilever chip glued to the surface (b). The PZT is capable of making the cantilevers out of plane by clamping the PCB to the PZT. Reproduced from [75].

and by clamping the PCB to the surface of the PZT, an out-of plane actuation of the cantilevers can be achieved.

The obvious drawback of this method is that not only the cantilevers are excited, but mechanical resonant modes of several structures (holder, cantilever chip, wires etc.) can interfere with the desired signal. A rather precise estimate of the resonant frequency is therefore necessary as well as a suitable reference during the measurements.

### 6.1.2 Readout

The readout of the cantilever frequency response is performed by a laser-optical system. The principle is similar to that found in a standard AFM system first described by Meyer *et al.* [15] (figure 6.2). A laser beam is focused onto the cantilever, and the beam is reflected at an angle depending on the deflection of the cantilever. A position sensitive photo-detector (PSD) is measuring the position of the reflected laser beam whereby the deflection of the cantilever can be deduced.

By driving the PZT with the frequency output of a GPA (In this case a HP4194A), and connecting the PSD output to the GPA input, the frequency response of the cantilever can be measured. If a resonant mode of the cantilever is excited, it will ideally show up on the detected signal as a positive amplitude peak accompanied by a phase shift.

To minimize signals from mechanical resonance and vibrations of parts other than the cantilevers a reference measurement is performed on the cantilever chip in the frequency range of interest. This frequency response is then subtracted during measurements, and identification of the resonant peaks are thus more straightforward.

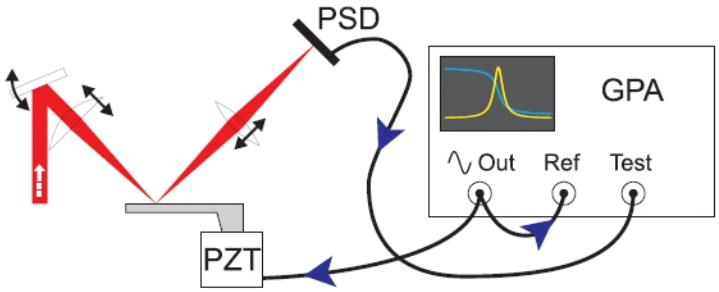


**Figure 6.2:** Schematics of the optical readout setup used in the measurements of cantilevers with no integrated actuation mechanism. The PSD measures the position of the the reflected laser-beam, and the output signal is connected to the input of a GPA, which also actuates the PZT. In this way the frequency response of the cantilever is obtained. Reproduced from [75].

### 6.1.3 Controlled Environment Chamber

The entire readout and actuation system is integrated in a sealed chamber attached to a membrane vacuum-pump capable of maintaining a vacuum of 0.5mBar (figure 6.3). The chamber has several connections allowing for control of the gaseous environment and an external heating coil makes it possible to control the temperature.

Besides the standard connections to the chamber several vacuum flanges can be used for electrical connections. For aligning the optical readout to the cantilever chip an external CCD camera is installed.

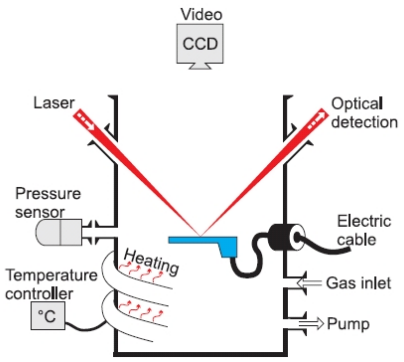


**Figure 6.3:** Schematics of the chamber containing actuation and optical readout. The chamber has transparent openings allowing use of the laser-optical readout system of figure 6.2. Heating and pressure control is integrated as well as electrical feed-trough. Reproduced from [75].

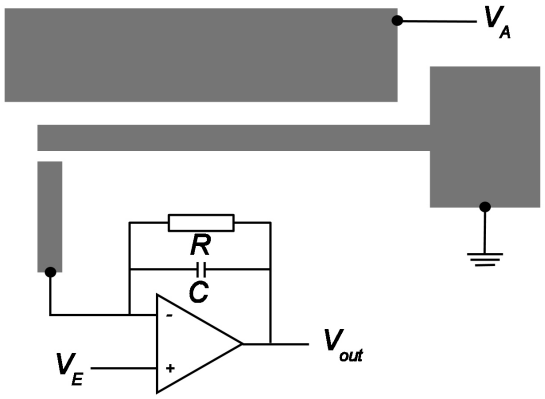


**Figure 6.4:** Schematic of the hard contact readout. Also shown in section 4

## 6.2 Hard Contact Readout

The setup used for characterization of the hard contact readout method consists of two major parts, the actuation electronics and the readout circuitry (figure 6.4). In the following sections the realization of the two parts will be presented.

To allow for easy integration and exchange of devices the cantilever chips were glued and wire-bonded to a pin grid array (PGA) having 121 pins (figure 6.5). The use of a PGA gives the advantage of easy exchange between several experimental setups having the same footprints - in this case the setup for ambient measurements and the setup for measurements in the SEM.

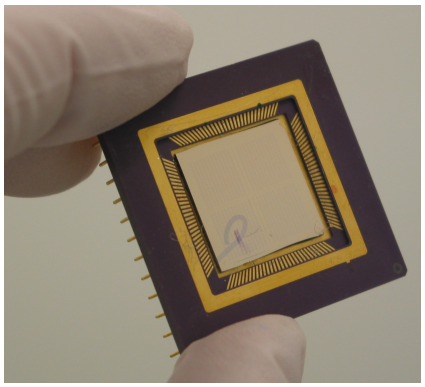

**Figure 6.5:** Pin grid array on which the cantilever chips were glued and wire-bonded. Some of the pins can be seen emerging from the backside, and on the frontside the bondpads are clearly visible in a square around the chip.

### 6.2.1 Actuation

The cantilever was operated in dynamic mode by applying an actuation voltage, $V_A = V_{A,ac} + V_{A,dc}$, consisting of an ac and dc component to the actuation-electrode and grounding the cantilever. For the characterization it was important to have complete control of the voltage levels, and computer control of the signals was desirable. For the dc component a TTI*QL355TP* computer controlled voltage supply was used and for the ac component a likewise computer controlled Tabor*8550* frequency generator was used.

Both voltage sources were computer controlled via a LabView interface, allowing for complete control of all measurement parameters as well as log-files for every measurement.

The Tabor*8550* frequency generator has a maximum output signal of $V_{ac,max} = 30V_{pp}$ and this turned out not to be sufficient when operating the cantilevers at ambient conditions. An EIN310L RF Power Amplifier was used to amplify the ac component of the signal at ambient conditions. The frequency response of the RF amplifier is shown in figure 6.6a, and it is clearly not completely linear in the wide range of frequencies tested. The amplification is linear as a function of input voltage at 600kHz (figure 6.6b), which is the approximate resonant frequency of the devices used in the measurements. The non-linearity can pose a problem if frequency sweeps are performed in wide frequency ranges.

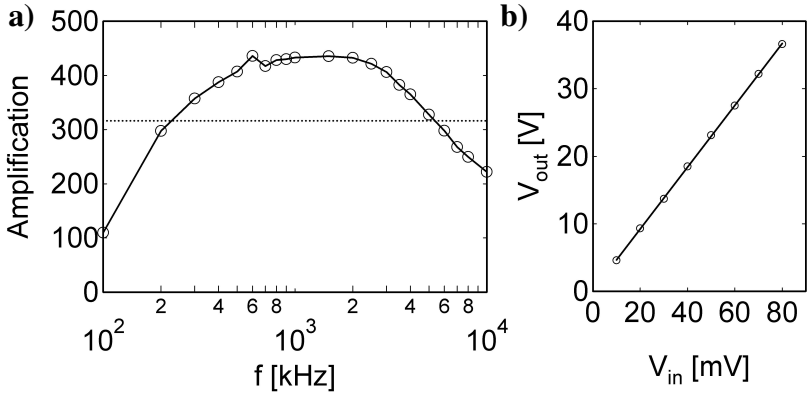


**Figure 6.6:** The output from the EIN*310L* RF Power Amplifier used in the experiments as a function of frequency (a) and as a function of input voltage at f=600KHz (b). The amplifier is supposed to amplify with 50dB (dotted line), but the frequency response is not constant in the entire range of interest. The amplification as a function of input voltage is on the other hand linear in the range of interest.

### 6.2.2 Readout

For the hard contact readout a small dc voltage, $V_E$, was applied to the readout-electrode close to the apex of the cantilever through an integrating transconductance amplifier. The dc voltage was supplied by a TTI*QL355TP* computer controlled voltage supply (also supplying the dc component of the actuation voltage). The dc voltage, $V_E$, was also controllable by the LabView interface and logged in every measurement.

The integrating transconductance amplifier is based on a Burr Brown OPA228P operational amplifier driven by ±15V. The OPA228P features very fast slew rates, wide bandwidth, and low noise characteristics. For the remaining components a capacitor of $C = 1$pF and a resistor of $R = 20$MΩ was chosen, facilitating a large integration constant and a slow discharge of the capacitor.

The dc-output of the integrating transconductance amplifier is measured with a computercontrolled Keithley*2000* multimeter, controllable by a LabView interface logging all parameters and data in every measurement.

#### Ambient

At ambient conditions the readout circuitry should be able to fit underneath a standard microscope making visual inspection during measurements possible. At the same time, a complete shielding of the circuitry should be possible, so the complete device was enclosed in a metal box. The schematics and an optical image of the finished amplifier are shown in figure 6.7.

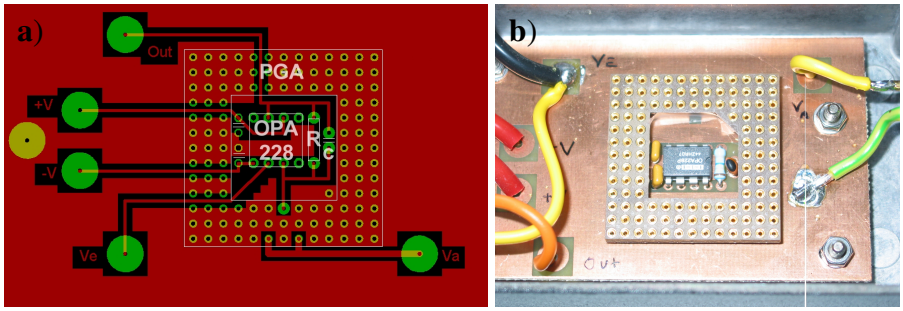


**Figure 6.7:** Hard contact readout amplifier schematics (a) and realized (b) for measurements at ambient conditions. The amplifier is based on a Burr Brown OPA228P operational amplifier with $C = 1$pF and $R = 20$MΩ

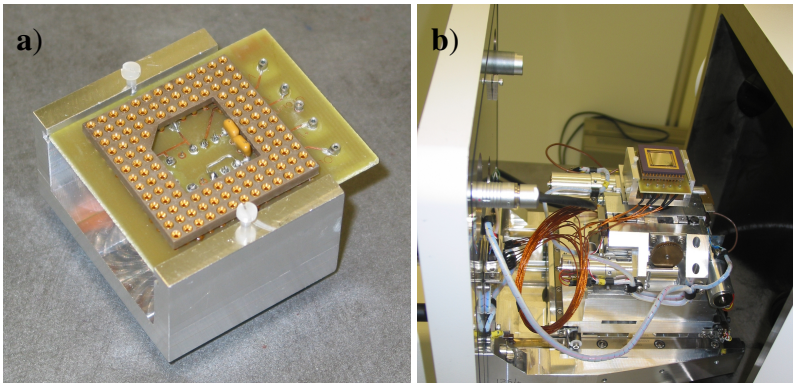


**Figure 6.8:** Images of the transconductance amplifier PCB in the SEM-holder (a) and in the SEM-chamber fitted with wires for connection to the outside.

### SEM and environmental chamber

A modified LEO*1550* SEM with electrical feedthroughs to the chamber facilitate electrical connection to the cantilever chip through shielded cables. For low pressure characterization and measurements in the SEM a different amplifier was needed. The components and layout were kept the same as in the ambient case, but the dimensions were changed so that the PCB could fit into the chamber. In figure 6.8 the PCB mounted in the SEM holder and in the SEM chamber is seen.

Operation in the SEM has the advantage compared to both ambient and the environmental chamber described in section 6.1.3, that the electron beam can be used for doing readout of the cantilever frequency response in a way similar to that of a laser beam in an AFM system [78, 79]. The electron beam is focused to a spot on the cantilever in an area with high contrast, and the secondary electron signal is monitored with a GPA also driving the cantilever. By sweeping the actuation frequency the frequency response of the cantilever is obtained, and the method has been applied on structures with resonant frequencies in the low MHz range [79]. This method of readout will in the following be called electron beam readout.

With the SEM it is also possible to do accurate, visual measurements of the vibrational amplitude. This can be used for determining the resonant frequency as well as the amplitude.

### Amplifier characterization

In order to characterize and test the integrating transconductance amplifier a test circuit has been designed and fabricated. The test circuit consist of a DG612DJ high speed analog switch controlled by an external voltage supply. The switch is

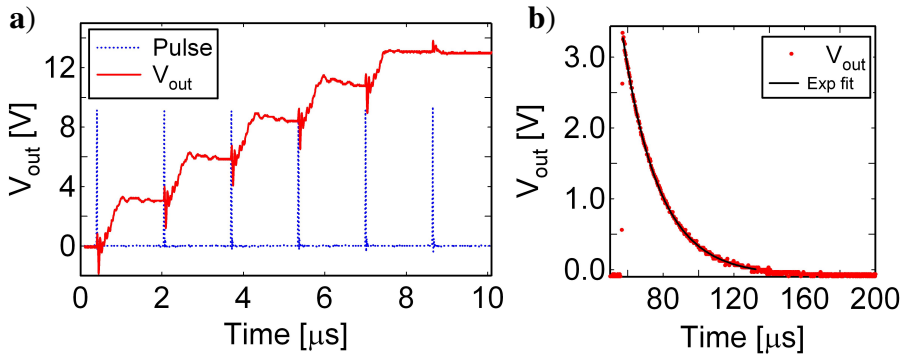


**Figure 6.9:** Test of the integrating transconductance amplifier using the test circuit. The output voltage as a function of time pulsed with 15ns current pulses (a) and the output voltage as a function of time after a single 15ns pulse (b). The output voltage decays exponentially with a characteristic time of $\approx 20\mu s$.

capable of switching-times down to 12ns in a wide range of frequencies.

The footprint and dimensions of the test circuit is made in a way that the PCB fits to the PGA of the amplifier. In this way the test-circuit is fitted directly on top of the amplifier as in the case of a real circuit. The amplifier has been tested down to the limit of 15ns pulses. The output of the integrating transconductance amplifier is shown in figure 6.9, where 100$\mu$A current pulses with a width of 15ns is applied with a frequency of 600kHz (a) and a single pulse is applied to visualize the decay of the output signal (b). The applied pulses correspond to an average input current of $\bar{I_{in}} \approx 1\mu$A, and only 5 pulses are needed to obtain a maximum output signal from the amplifier. From the figure it is apparent that the output signal is rising even after the 15ns pulse have stopped. This is probably due to stray capacitances that are charged during the pulse and discharges after the pulse, making a current flow into the amplifier.

The output voltage decays exponentially with a characteristic time of $\sim 20\mu s$, and is in good accordance with the characteristic time of the $RC$-value $RC = 20\mu$s which is the theoretical characteristic time of discharge.

## 6.3 Manipulation

For manipulation and positioning of beads on cantilever surfaces a high-resolution optical microscope system based on a Mitutoyo 50x objective is used (figure 6.10). In combination with a Navitar UltraZoom lens system this offers up to 228 times magnification, corresponding to a view field of 20$\mu$m×15$\mu$m with a 1/3" CCD

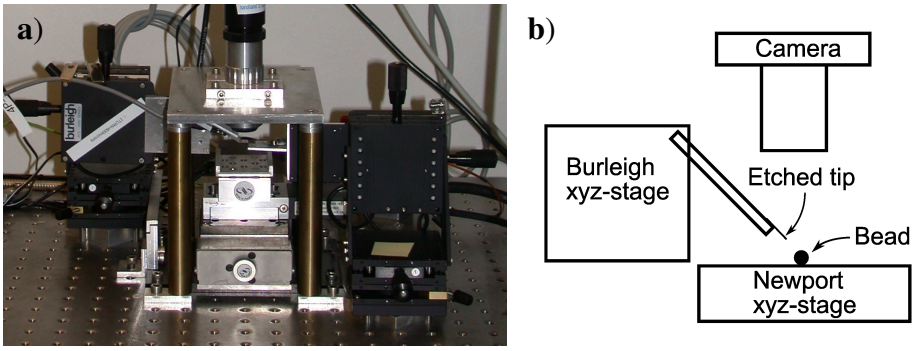


**Figure 6.10:** Photo (a) and schematic (b) of the setup used for manipulating beads on the cantilevers. Only one manipulator is used in the experiments.

camera. The large working distance of 13mm obtained with this setup eases sample handling and manipulation.

Beneath the optical setup a Newport *zyx*-stage capable of moving ±3mm in the *xy*-plane and ±3mm in the *z*-direction with a resolution of 100nm is positioned. The *xyz*-stage is controlled by a Newport motion-controller which in turn can be operated by joystick or controlled by computer. The Newport *zyx*-stage serves as the 'table' on which the cantilever is fixed alongside the bead-sample.

For manipulation a Burleigh PCS-5400 manipulator system consisting of three

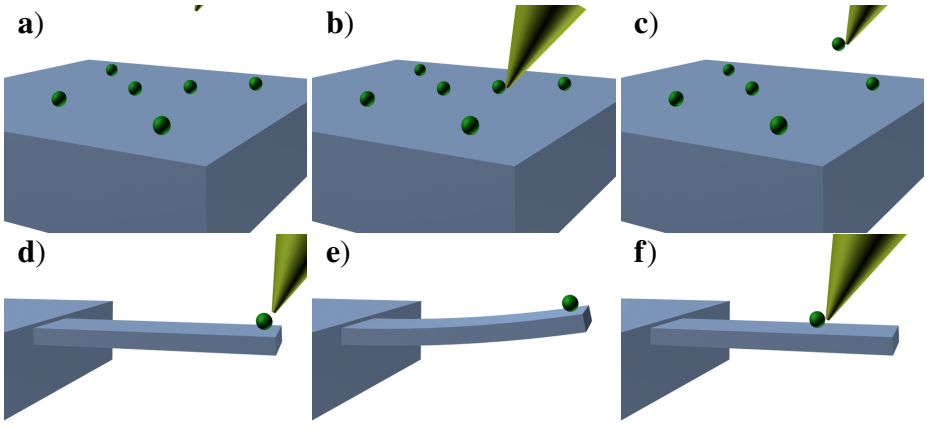


**Figure 6.11:** Schematic of the manipulation procedure. The beads are dispersed on a surface (a) and contacted using an etched tip (b). Adhesion forces allow the beads to be picked up (c) and placed on a cantilever surface (d), before the resonant frequency is determined (e). The bead can be manipulated on the cantilever and moved to a new position (f).

linear, piezoelectric stages, each with a resolution of roughly 30nm and a travel distance of 300$\mu$m, combined with a manual coarse control is used. Equipping the manipulator system with an electrochemically etched tungsten tip with a tip diameter of roughly 1$\mu$m facilitates three-dimensional manipulation of beads using adhesion forces to stabilize the bead on top of the micro-cantilevers. The system permits to pickup, transfer, and manipulate beads, nanowires and nanotubes in a reproducible manner to the desired position on the target structure (figure 6.11) as also demonstrated by Dohn *et al.* [80] and Kjelstrup-Hansen *et al.* [81].

### 6.3.1 Beads for Mass Loading

Two different kinds of beads have been used for mass loading of the micro-cantilevers: gold and polystyrene beads. Both kinds of beads are commercial available and have been bought through Sigma-Aldrich (gold beads) and Kisker (polystyrene beads).

The gold beads have a diameter of 1.5-3$\mu$m and a gold purity of 99.9%. They are spherical in shape (figure 6.12a), but the exact size needs to be determined by SEM investigations in every measurement. The mass of the beads are $m_{\mathrm{Au,bead}} \approx 34 - 270\mathrm{pg}$ assuming a density of $\rho_{\mathrm{Au}} = 19300\mathrm{kg/m^3}$.

The polystyrene beads have a diameter of 992nm (given by the manufacturer). The beads are completely spherical in shape, but it is unknown if they have a hollow core. The density of polystyrene is $\rho_{\mathrm{Poly}} = 1.05 \cdot 10^3\mathrm{kg/m^3}$ giving a mass of $m_{\mathrm{Poly,bead}} \approx 0.5\mathrm{pg}$, assuming a solid core.

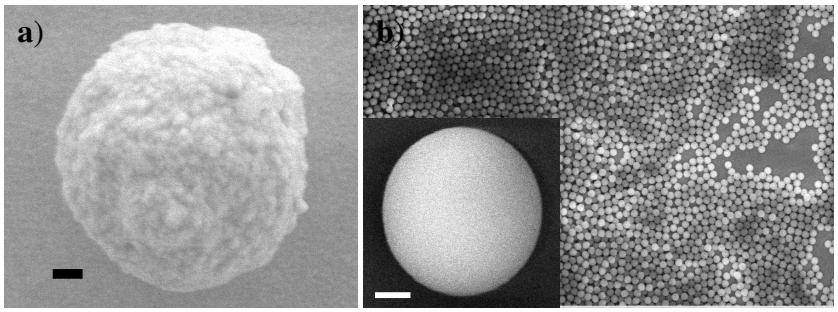


**Figure 6.12:** SEM image of a gold bead (a) and polystyrene beads (b) used to mass load cantilevers. The rough surface of the gold bead is clearly seen, whereas the polystyrene beads are extremely uniform in size and have a smooth surface. Both scale bars have a length of 200nm.

## 6.4 Summary

The experimental setups needed for the experiments on the position dependent mass responsivity and the characterization of the hard contact readout method have been presented.

For actuation of the cantilevers used in the experiments on the mass responsivity, the cantilever chip is clamped to a PZT driven by a GPA. The readout is performed using a laser optical setup in a way similar to that of an AFM, where a PSD measures the position of the reflected laser beam, and the signal is put into the GPA. In this way the frequency response of the cantilever can be measured.

The mass loading and manipulation of beads on the cantilever are performed using a manipulation setup equipped with an etched tungsten tip. With the tip a bead of desired size and weight is picked up from a surface and moved to the cantilever, where it can be moved around.

For characterization of the hard contact readout method a readout circuitry has been fabricated based on an integrating transconductance amplifier. Two different amplifiers have been designed for use in a SEM and at ambient conditions, but sharing the same PGA so cantilever chips can be moved from one system to the other. In the SEM it is possible to do readout using the electron beam and measure the secondary electron signal with a GPA also actuation the cantilever.

# Chapter 7

# Characterization of Position and Mode Dependence

A common problem with cantilever based mass sensor when doing single particle detection is that the position of the attached mass needs to be known in order to estimate the mass. This chapter describes the experiments performed on a cantilever to test the possibility of finding the position as well as the exact mass of an attached particle or cell. Also the mass responsivity of the first four bending modes as a function of the attached mass position have been found.

## 7.1 Responsivity

To test the theoretical findings on the position dependent mass responsivity derived in section 3, experiments were performed on a micrometer-sized cantilever fabricated in $SiO_2$ and coated on the topside with 10 nm Ti and 100nm Au (For details on the fabrication process see the work of Petersen *et. al* [77]). The cantilever dimensions was measured using a SEM, yielding a length, width and thickness of approximately 153$\mu$m, 11$\mu$m and 1.05$\mu$m respectively. The total mass of the cantilever is from the measured dimensions $m_0 \simeq 7$ng.

To measure the frequency response of the cantilever the laser-optical detection system and environmental chamber described in section 6.1 was used, while evacuated to a pressure of 0.5mBar. The resonant frequency for the first four bending modes of the unloaded cantilever are listed at the top of table 7.1 along with the theoretical predicted values. The material properties used in the calculations of the resonant frequency can be found in Appendix F. A good correspondence between the calculated and measured values can be seen.

| Mode | 1 | 2 | 3 | 4 |
|---|---|---|---|---|
| $f_{\text{exp}}$ [Hz] | 30712 | 192493 | 539060 | 1056640 |
| $f_{\text{sim}}$ [Hz] | 31734 | 198815 | 556486 | 1089920 |
| $\Delta f_{\text{max}}$ [Hz] | 480 | 2541 | 6059 | 9864 |
| $\mathcal{R}_n/\mathcal{R}_1$ | 1 | 5.3 | 12.6 | 20.6 |
| $Q$ | 284±91 | 827±101 | 1054±127 | 1470±485 |
| $RMS\,(f_{fit})$ [Hz] | 0.6 | 0.8 | 1.7 | 2.4 |
| $\Delta m_{min,1}/\Delta m_{min,n}$ | 1 | 4 | 4.5 | 5.1 |
| $C_n/C_1$ | 1 | 2.5 | 4.2 | 5.8 |
| $(C_n/C_1)^2$ | 1 | 6.3 | 17.6 | 34.4 |

**Table 7.1:** The resonant frequency measured, $f_{\text{exp}}$, and calculated, $f_{\text{sim}}$, for the first four bending modes of the cantilever. The experimentally observed maximum change in resonant frequency, $\Delta f_{\text{max}}$, and experimentally observed relative mass responsivity, $\mathcal{R}_n/\mathcal{R}_1$. The RMS value of the fit to the resonant peaks, $RMS\,(f_{fit})$, for all measurements are listed and from this the relative sensitivity, $\Delta m_{min,1}/\Delta m_{min,n}$, of the cantilever for the first four modes are calculated. At the bottom the ratio of $C_n$ to $C_1$ is listed.

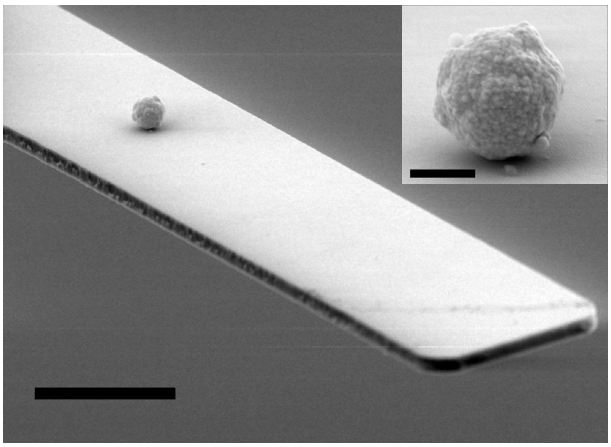

**Figure 7.1:** SEM image showing part of a cantilever with a gold bead positioned close to the apex. The scale bar is 5$\mu$m long. The inset shows a close-up of the gold bead, where no damage can be seen as a result of the manipulation. The scale bar of the inset is 500nm long.

A single gold bead with a radius of 0.9$\mu$m, corresponding to a mass of $\Delta m \approx 60$pg, is positioned on the cantilever using the manipulation setup described in section 6.3. The position of the gold bead is determined from optical images with an estimated accuracy of $\pm 1\mu$m. A SEM image of the cantilever apex with the gold bead is shown in figure 7.1.

After positioning the gold bead, the resonant frequencies for the first four bending modes are recorded and the gold bead is moved to a new position. Typical examples of the recorded amplitude resonant peaks for the second bending modes are seen in figure 7.2. The resonant frequency is seen to decrease significantly when the gold bead is positioned close to the tip of the cantilever and almost no change is seen when the gold bead is positioned at a node. The fitted amplitude peaks all have a standard deviation of less than 0.002%, and if doing successive measurements without moving the bead, the measured resonant frequencies are within this limit.

The change in resonance frequency for the first four bending modes of the cantilever for 16 bead position along the length axis has been measured. The observed relative change in resonance is compared to the values obtained by calculations (from equation 3.5) and excellent agreement is obtained for all bending modes as shown in figure 7.3.

For all four bending modes the highest change in frequency, $\Delta f_{max}$, is obtained when the gold bead is positioned at the tip of the cantilever (listed in table 7.1). The absolute change in frequency and thereby the mass responsivity, $\mathcal{R} \approx \Delta\omega_n/\Delta m$, increases with the mode number giving a mass responsivity of ~164Hz/pg in the fourth mode for the added mass of 60pg. The relative mass responsivity $\mathcal{R}_n/\mathcal{R}_1$ is also listed in table 7.1 and the responsivity is seen to increase by a factor of ~21 using the fourth mode compared to the fundamental mode (table 7.1).

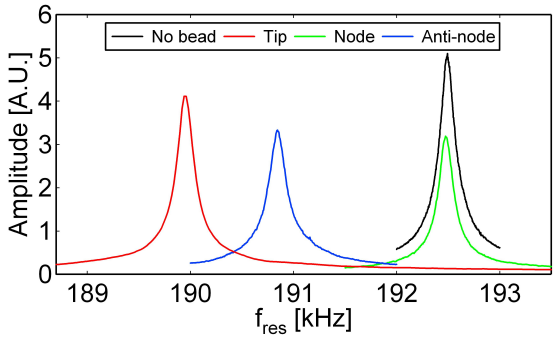


**Figure 7.2:** Resonant peaks for the second bending mode for different positions. Only part of the recorded second bending modes peaks are shown for clarity, and their names refer to the position of the gold bead.

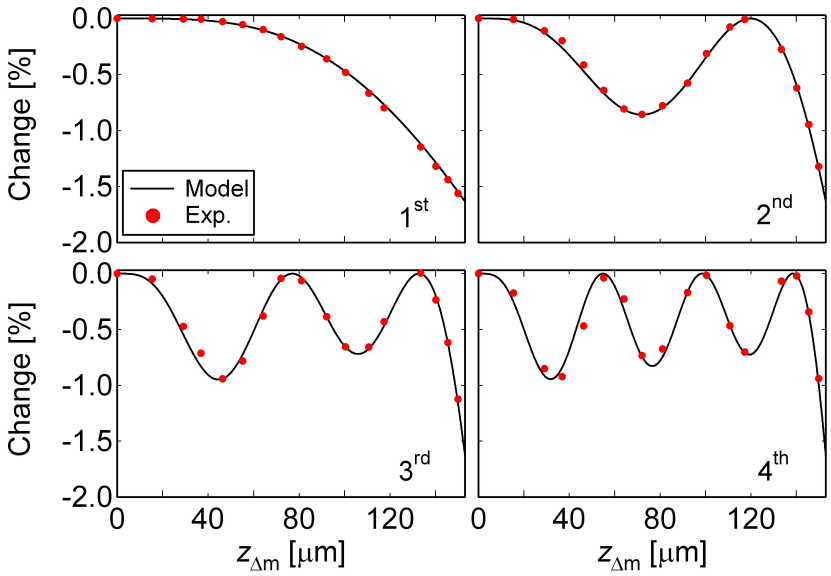


**Figure 7.3:** The change in resonant frequency as a function of gold bead position, $z_{\Delta m}$ for the first four bending modes together with the analytical results.

From measurements at all positions an average $Q$-factor was calculated (listed in table 7.1). The $Q$-factor increases almost a factor of 3 going from the first to the second bending mode and the fourth mode has a $Q$-factor that is more than 5 times larger than the first mode. There is no significant difference between the $Q$-factor of the unloaded and loaded cantilever. The uncertainty in $Q$-factor is increasing with the mode number.

The root-mean-square value of the uncertainty in the fit to the measured frequency responses, $RMS(f_{fit})$, are also listed in the table. This value increases with increasing mode numbers, but the minimum detectable mass, $\Delta m_{min} = \mathcal{R}^{-1}\Delta\omega_{min}$, still decreases with increasing mode number due to the increase in mass responsivity. The sensitivity of the fourth mode corresponds to a minimum detectable mass of $\Delta m_{min} = 15$fg and is roughly 5 times larger than obtained in the first mode of operation.

## 7.2 Mass and Position Determination

The measured data presented in the former section can be used to verify the theory of prediction of the mass and position from measurements of the resonant frequency of several bending modes. $\omega_n$ and $\omega_{n,\Delta m}$ is taken from the measurements presented in the former section and using equation 3.7 derived in section 3

$$\frac{\Delta m}{m_0} = \frac{1}{U_n(z_{\Delta m})^2}\left(\frac{\omega_n^2}{\omega_{n,\Delta m}^2} - 1\right),$$

$\Delta m/m_0$ is calculated.

In figure 7.4 the calculated $\Delta m/m_0$ is plotted for measurements at three different positions using all four measured modes. It is seen that in each of the three cases, the four different graphs intersect at a single point marked with an arrow. From the intersection the position of the attached mass can be found as well as the mass.

The results of the proposed fitting procedure (equation 3.8) is shown in figure 7.5 where the calculated position, $\tilde{z}_{\Delta m}$, as a function of the measured position, $z_{\Delta m}$, is plotted together with the calculated mass ratio. From the figure it is seen that the calculated positions are within a $\mu$m of the measured value, except for a single point closest to the base of the cantilever. This single measurement point returns a slightly wrong position and wrong mass, due to the very small frequency changes for all modes at this position. The spread in positions are for most points smaller than the uncertainty in position determined by the optical setup ($\pm 1\mu$m). This indicates that the position determined using the proposed method are more accurate than the visual detection method used in the measurements.

The average mass ratio is $\widetilde{\Delta m}/m_0 = 0.0084$, when the point closest to the cantilever base is omitted. The calculated mass of the gold-bead is then

$$m_{bead} = \Delta m = 7\text{ng} \cdot 0.0084 \simeq 60\text{pg}, \tag{7.1}$$

which is in perfect agrement with the expected value.

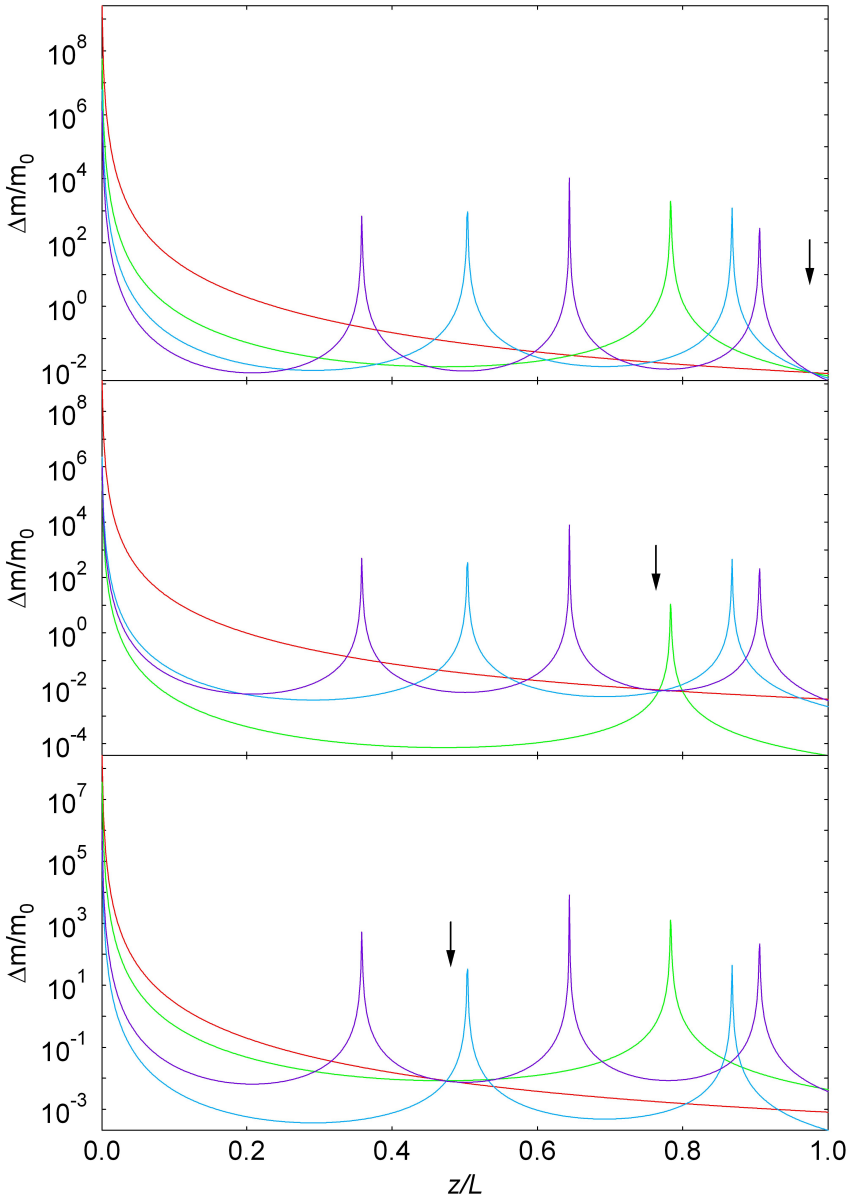


**Figure 7.4:** From the measurements with a point mass, the ratio of $\Delta m$ to $m_0$ is calculated for the first four modes as a function of position, $z$ in units of the length, $L$. The mass and position can be deduced visually from the intersection of the graphs for each bending mode. Three examples are shown, with the intersection marked with an arrow.

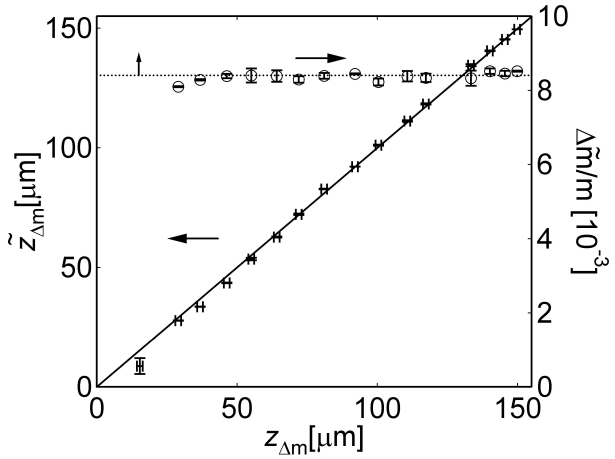


**Figure 7.5:** The calculated position, $\tilde{z}_{\Delta m}$, is shown as a function of the measured position together with the calculated mass ratio, $\Delta\tilde{m}/m_0$. The calculated mass ratio for the measurement at position $z_{\Delta m} \approx 16\mu m$ is not shown, since the calculated value deviates an order of magnitude.

## 7.3 Summary and Discussion

In this chapter it was shown by measurements on the first four bending modes of a cantilever, that the highest mass responsivity of a cantilever is obtained at the highest mode of operation. From the dimensions of the cantilever and unloaded resonant frequencies of several modes it was possible to determine the position of the attached bead within a few $\mu$m and estimate the mass of the attached bead.

The $Q$-factor is seen to increase with mode number. This is contrary to the predictions of Ekinci *et al.* [51], but in accordance with the findings of several groups [47, 57, 58, 82]. The increase is likely due to the smaller centre of mass movement [32] and the decrease in momentum exchange at higher frequencies [25]. The model for the dissipation caused by molecular damping given by Blom *et al.* (equation 2.16) predicted that $Q \propto C_n$ and comparing the ratios of $C_n/C_1$ given in table 7.1 to the increase in $Q$-factor, this is indeed seen to be the case.

The rather low $Q$-factor observed for the cantilever is due to the metal coating [83], and similar uncoated cantilevers have Q-factors that are 10 times higher. The increasing uncertainty in $Q$-factor with mode number is most likely due to the readout system. The laser spot on the cantilever is quite large, $r \approx 25\mu$m, and is thereby covering both nodes and anti-nodes.

The increase in mass responsivity of the cantilever with mode of operation is

in reasonable accordance with the theory presented in chapter 3 where a $\propto C_n^2$ is expected (values of $(C_n/C_1)^2$ are given in table 7.1 for comparison). The increase in mass responsivity with mode of operation is together with the increase in $Q$-factor responsible for the observed increase in sensitivity. Thus, operation at higher modes is a straightforward way to improve both the mass responsivity and the sensitivity of a cantilever based mass sensor in the used system.

The estimated mass of the attached bead was from the measurements in perfect agreement with the expected value. A single measurement point returned a false position and mass, due to the very small frequency changes for all modes at this position. This indicates that the method is most accurate for masses attached to the outer 4/5 of the cantilever.

# Chapter 8

# Characterization of Hard Contact Readout

This chapter describes the experiments performed on cantilever based mass sensors using hard contact readout. Several aspects have been explored such as lifetime, mass measurements and down-scaling. Each section is followed by a short summary and discussion of the obtained results.

## 8.1 Initial Characterization

To test the ability to do read-out using the hard contact readout method, a cantilever of UV-type B with Pt coating (chip 14) wire-bonded to a PGA, was placed in a SEM along with readout electronics. The SEM was pumped to a vacuum of $5 \cdot 10^{-6}$mbar, to make use of the imaging capabilities as well as electron beam readout.

The frequency response of the cantilever was initially found using electron beam readout, and is shown in figure 8.1. From a Lorentzian fit to the amplitude the resonant frequency is found to be $\sim$ 653kHz with a $Q$-factor of 2000. To actuate the cantilever actuation levels of $V_{\mathrm{A},dc}$=2V and $V_{\mathrm{A},ac}$=1.25V were used.

On the same device, hard contact readout with the integrated readout system was tested. The output of the integrating transconductance amplifier, $\Delta V_{\mathrm{o,ss}} - V_{\mathrm{E}}$ was recorded while the excitation frequency was scanned in discrete steps near and at the resonant frequency found using electron beam readout. The frequency response at vacuum (still inside the SEM-chamber) and at ambient conditions after the SEM measurements are seen in figure 8.2. Both measurements have a significant output signal in a frequency range, $\Delta f$ of a few kHz, and assuming the

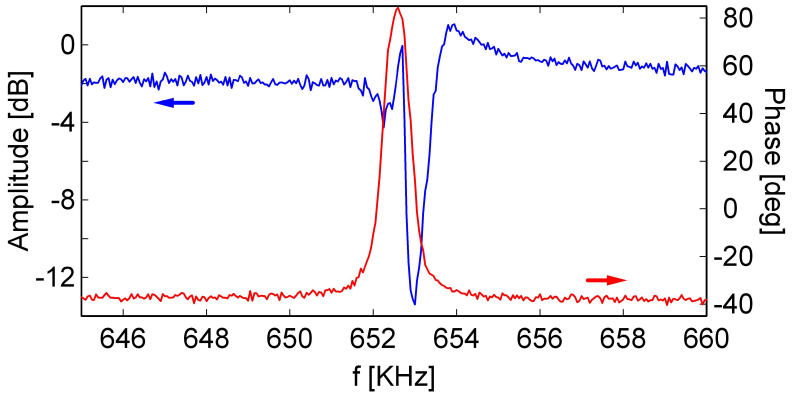


**Figure 8.1:** The frequency response of a cantilever, UV-type A with a Pt coating (chip 14) obtained using electron beam readout. The frequency response shows a valley and not a peak at resonance and is an artefact of the electron beam readout method. The resonant frequency is at ~ 653kHz. For actuation values of $V_{A,dc}$=2V and $V_{A,ac}$=1.25V was used. The $Q$-factor is around 2000.

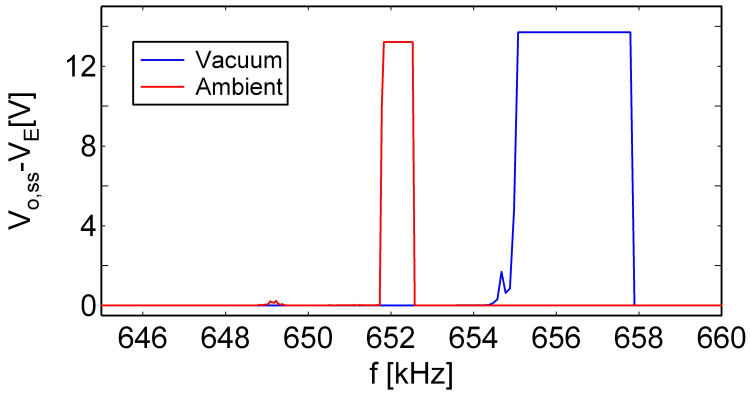


**Figure 8.2:** The measured voltage $\Delta V_{o,ss} - V_E$ obtained using hard contact readout. For actuation at vacuum $V_{A,dc}$=5V, $V_{A,ac}$=4V and $V_E$=0.5V and at ambient $V_{A,dc}$=30V, $V_{A,ac}$=14V and $V_E$=1V. The difference in maximum level is due to a difference in the $V_E$.

resonant frequency, $f_0$, of the cantilever to be in the center of these, the measured resonant frequencies are 652kHz (ambient) and 656kHz (vacuum). The reciprocal relative frequency resolution, $f_0/\Delta f$ ~ 800 at ambient and ~ 200 at vacuum for these particular measurements.

For actuation $V_{A,dc}$=5V, $V_{A,ac}$=4V and $V_E$=0.5V was used at vacuum and $V_{A,dc}$=30V, $V_{A,ac}$=14V and $V_E$=1V was used at ambient conditions. The actuation voltages

are not similar for the two measurements due to the increase in damping going from vacuum to ambient. A bigger actuation force is thus needed to make contact between electrode and cantilever at ambient conditions.

The steady state voltage, $V_{\mathrm{o,ss}}$, saturates at the amplifier maximum during the measurements. A minimum average current of $\overline{I_{\mathrm{in,min}}} \simeq 1\mu\mathrm{A}$ and maximum contact resistance of $R_{\mathrm{C},max} \simeq 1\mathrm{k}\Omega$ can thus be deduced from the measurements using equation 4.3 and a value of $R$ =20MΩ and assuming $t_c \simeq 1\mathrm{ns}$.

### 8.1.1 Effects of Actuation Voltage

The effect of actuation voltage and thereby force on the impact between electrode and cantilever was investigated on a second cantilever, UV-type A (chip 8), at ambient conditions (figure 8.3). In all measurements $V_{\mathrm{A},ac} = 10\mathrm{V}$ and $V_{\mathrm{E}} = 1\mathrm{V}$, while $V_{\mathrm{A},dc}$ was varied to adjust the vibration amplitude. $V_{\mathrm{o,ss}}$ was measured while the excitation frequency was scanned in discrete steps near and at the resonant frequency. This was repeated at decreasing levels of $V_{\mathrm{A},dc}$, until the resonant peak disappeared in the output signal, $V_{\mathrm{o,ss}}$ (figure 8.3a). The frequency span with a significant output signal, $\Delta V_{\mathrm{o},ss} > 0.1\mathrm{V}$, decreases with decreasing $V_{\mathrm{A},dc}$, is minimized at $V_{\mathrm{A},dc} = 19.2\mathrm{V}$, and vanishes at $V_{\mathrm{A},dc} = 19.1\mathrm{V}$. From the measured voltages, the time averaged current is estimated to be in the order of $\overline{I_{in}} \approx 10 - 50\mathrm{nA}$ when the maximum signal is obtained.

In figure 8.3b the reciprocal relative frequency resolution $f_0/\Delta f$ corresponding to the measurements is shown. From $V_{\mathrm{A},dc} = 20\mathrm{V}$ to $V_{\mathrm{A},dc} = 19.2\mathrm{V}$, the reciprocal relative frequency resolution increases from $f_0/\Delta f = 300$ to $f_0/\Delta f \simeq 8.000$. Note, at $V_{\mathrm{A},dc} = 19.2\mathrm{V}$ the resolution is limited by the resolution in applied frequencies.

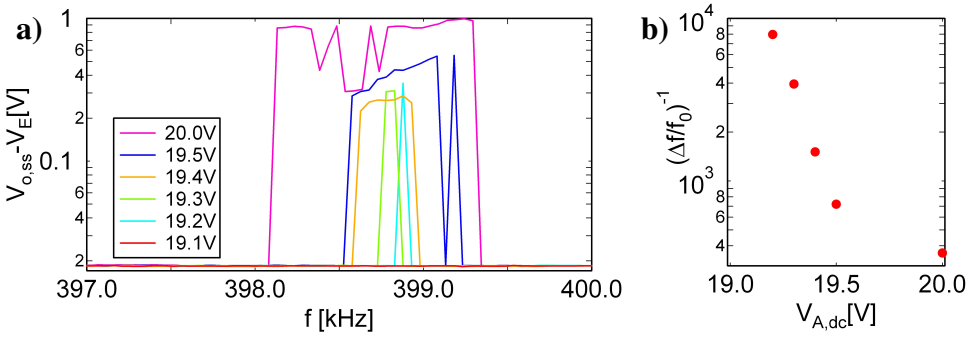


**Figure 8.3:** The measured voltage $\Delta V_{\mathrm{o,ss}} - V_{\mathrm{E}}$ as a function of frequency at different levels of $V_{\mathrm{A},dc}$ (a). The reciprocal relative frequency resolution $f_0/\Delta f$ in the measurements (b).

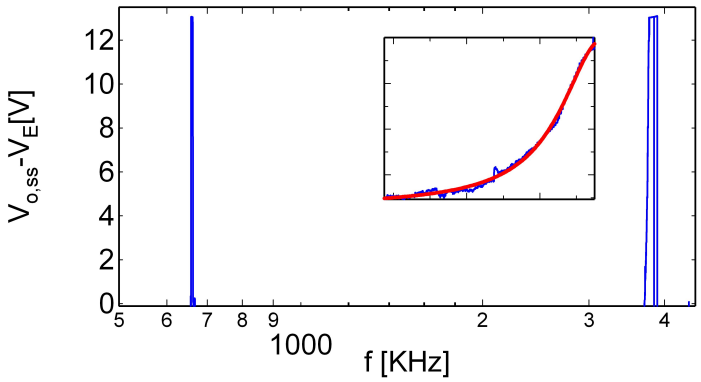


**Figure 8.4:** Measurement on the $1^{st}$ and $2^{nd}$ bending mode using hard contact readout. The inset shows a closeup of the $2^{nd}$ mode signal increasing to maximum with a Lorentzian fit. The measured resonant frequency for the $1^{st}$ and $2^{nd}$ bending mode are ~660KHz and ~3.8MHz respectively. The actuation voltages are $V_{A,dc}$=35V and $V_{A,ac}$=35V with $V_E$=1V in both cases.

| Readout | $V_{A,ac}$ [V] | $V_{A,dc}$ [V] | $V_E$ [V] | $f_1$ [KHz] | $f_2$ [MHz] |
|---|---|---|---|---|---|
| Hard contact readout | 35 | 35 | 1 | 660 | 3.8 |
| Electron beam readout | 0.5 | 1.5 | - | 657 | - |
| Electron beam readout | 1.25 | 25 | - | - | 4.1 |

**Table 8.1:** Device resonant frequencies found using both hard contact readout (Ambient) and electron beam readout (vacuum).

### 8.1.2 Second Mode Operation

The ability of the hard contact readout method to do measurements of higher bending modes has been investigated on UV-cantilevers at ambient conditions. The frequency response is shown in figure 8.4, and contains two measurements to cover the frequencies of both the first and the second bending mode.

The first mode resonant frequency measured using hard contact readout was 660kHz whereas the second mode resonant frequency was 3.8MHz. The theoretical second mode resonant frequency is $(C_2/C_1)^2$ times larger than the first mode frequency corresponding to a theoretical frequency of 4.1MHz. The measured second mode resonance is 3.8MHz and thereby around 7% lower than the theoretical value. The resonant frequency of the two first modes for the particular device was also found using electron beam readout. The obtained data is shown in table 8.1 together with the values obtained by hard contact readout. By electron beam readout the difference in first and second mode frequencies are in good agrement with

theory. The measured first mode resonant frequencies from electron beam readout and hard contact readout are within 3kHz, but for the second mode a difference of 300kHz is seen.

From a fit to the slope of the $2^{nd}$ mode signal obtained by hard contact readout a $Q$-factor of 100 is obtained, whereas the reciprocal relative frequency resolution $f_0/\Delta f$ for the two modes are 100 (first) and 20 (second).

### 8.1.3 Summary and Discussion

In this section it was shown possible to measure the resonant frequency of the first and second bending mode of a micro-scale cantilever using the hard contact readout method. It was also shown that the reciprocal relative frequency resolution $\underline{f_0/\Delta f}$ could be tuned with the actuation voltage. A minimum average current of $\underline{I_{\text{in,min}}} \sim 1\mu$A was estimated from the measurements.

None of the devices of UV-type B were seen to stick to the readout electrode during measurements. This is in accordance with the proposed design rule (equation 4.5).

Comparing the resonant frequency found using electron beam readout and hard contact readout agreement within ~5kHz was observed for the first mode. The difference in resonant frequencies is most likely due to the difference in actuation voltage, causing a change in the spring softening effect [59, 62–64] or the spring hardening effect [60, 61], due to the cantilever-electrode contact.

The theoretical spring softening effect caused by the change in actuation voltage can be calculated from equation 2.37. A -4kHz shift in resonant frequency is measured going from vacuum to ambient (figure 8.2), whereas the calculated effect from the change in actuation voltage is $\Delta f_{eff}$ ~-20kHz. The observed effect is thereby smaller than the theoretically predicted effect. In the second mode, a similar change in voltage causes a shift of 300kHz, observed when comparing electron beam readout and hard contact readout (table 8.1). The calculated change in resonant frequency is 150kHz, so in this case the observed change is smaller than expected.

The reciprocal frequency resolution was seen to be tunable, and reciprocal frequency resolution of 8000 was observed at ambient conditions, and was limited by the resolution in applied frequencies. The reciprocal frequency resolution can be regarded as a measure of the $Q$-factor for the measurement. For comparison the $Q$-factor obtained for the cantilever at vacuum was 2000. The $Q$-factor of 2000 at a pressure of $5 \cdot 10^{-6}$mbar indicates that the limiting dissipation is not momentum exchange (section 2.2, figure 2.3) but rather losses due to the metal-coating [25], and is thereby the maximum $Q$-factor obtainable for these cantilevers regardless

of the pressure.

## 8.2 Surface Failure

Several different coating thicknesses, deposition angles and materials has been tested. It has only been possible to measure a signal using hard contact readout from a part of these chips. The resonant frequency of all chips was found by visual inspection or using electron beam readout, and are listed in table 8.2 along with the maximum obtained output voltage using hard contact readout. Also the estimated average number of successive measurements on the same device giving similar results are listed.

From the table it can be seen that the signal levels obtained using hard contact readout is increasing with metal thickness when sweep mode was used for deposition. This is in contrast to the findings of tilted deposition where a deposition thickness of 500Å is better than a deposition thickness of 1000Å. The number of measurements on a device, giving an output signal similar to the maximum, is the highest if Pt is used as metal coating. In the following sections the data presented are from measurements on either chip 8 or chip 14 which showed the best durability and signal levels.

The signal measured from the cantilevers disappears after a number of measurements on the device and the actuation levels will then have to be raised in order to achieve similar signals again. In figure 8.5 a test of the lifetime of a cantilever from chip 14 is shown. The frequency is increased in discreet steps till an output

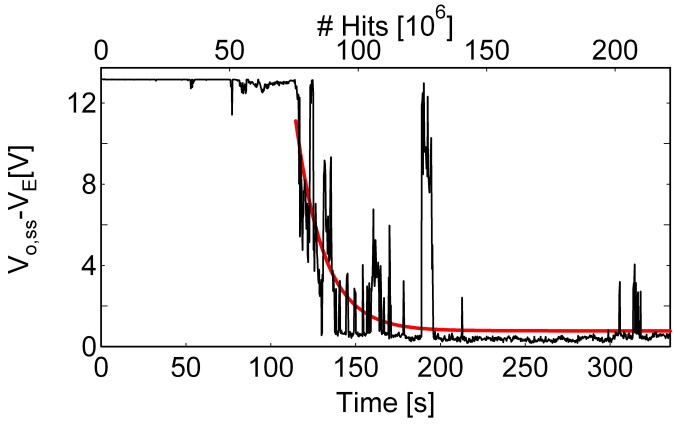


**Figure 8.5:** Lifetime measurements on a Pt coated cantilever from chip 14 using hard contact readout. The red line is a exponential fit to the decay having a characteristic time of 17s.

voltage above 10V is measured, and the frequency is then kept fixed and the output is measured 4 times a second. The output is stable for ~120s, or $\sim 8 \cdot 10^7$ hits, whereafter it decreases exponentially with a characteristic time of 17s, or $\sim 10^7$ hits (red line).

A failure of the device could be caused by 1) fracture of the cantilever or part of it or 2) an increase in contact resistance.

### 8.2.1 Sources of Failure - Fracture

To make sure that the cantilever was still moving and hitting the electrode a device from chip 14, where a signal could no longer be obtained using hard contact readout was put into a SEM. The resonant frequency was determined using electron beam readout (figure 8.6) to be $\sim$ 650kHz, and the vibration was visually confirmed using the SEM standard imaging system (figure 8.7a and b).

From a series of images like that of figure 8.7b, the resonating amplitude as a function of actuation voltage $V_{A,ac}$ was plotted to determine the voltage required for contact (figure 8.7c). A clear break in the amplitude is observed between $V_{A,ac} = 4$V and $V_{A,ac} = 5$V indicating that the electrode is hitting the electrode for $V_{A,ac} \geq 5$V. Measurements on the device with $V_{A,ac} > 5$V and unchanged $V_{A,dc}$ still gave no signal at or near resonance.

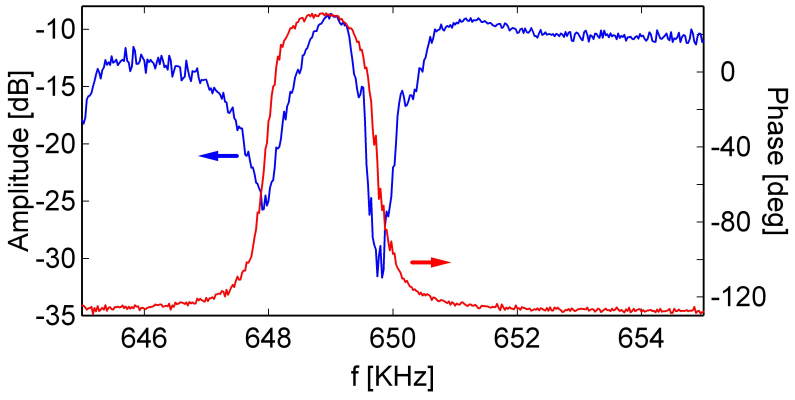


**Figure 8.6:** The frequency response of a cantilever from chip 14 obtained using electron beam readout. The resonant frequency is at $\sim$ 650kHz, with actuation voltages of $V_{A,dc}$=2V and $V_{A,ac}$=1.25V.

| Chip | Mode | Coating | Thick. [Å] | Rate [Å/s] | R [Ω] | $f_{res}$ [KHz] | $V_{o,ss}$ [V] | Repeat [#] |
|---|---|---|---|---|---|---|---|---|
| 1 | Sweep | Ti/Au | 200/500 | 2/5 | 14 | 710 | None | - |
| 2 | Sweep | Ti/Au | 200/1000 | 2/10 | 7-8 | 700 | None | - |
| 3 | Sweep | Ti/Au | 200/2000 | 2/10 | 4-5 | 670 | None | - |
| 4 | Sweep | Ti/Au | 200/2000 | 2/5 | 3-4 | 630 | $10^{-4}$ | 1-5 |
| 5 | Sweep | Ti/Au | 200/5000 | 2/10 | 3-4 | 590 | None | - |
| 6 | Sweep | Ti/Pt | 200/2000 | 2/5 | 14 | 625 | $10^{-3}$ | 1-5 |
| 7 | Sweep | Ti/Pt | 200/2000 | 2/10 | 20 | 650 | $10^{-3}$ | 1-5 |
| 8 | Sweep | Ti/Pt | 200/3000 | 2/10 | 13-15 | 400 | 1 | 10-20 |
| 9 | 45° | Ti/Au | 100/500 | 2/10 | - | 515 | Full | 1-5 |
| 10 | 45° | Ti/Au | 100/1000 | 2/10 | - | 480 | None | - |
| 11 | 45° | Ti/Pt | 100/500 | 2/10 | - | 510 | $10^{-2}$ | 5-10 |
| 12 | 30° | Ti/Au | 100/500 | 10/10 | 25-30 | 590 | Full | 1-5 |
| 13 | 30° | Ti/Au | 100/1000 | 10/10 | 6-7 | 560 | None | - |
| 14 | 30° | Ti/Pt | 100/500 | 10/10 | 10 | 650 | Full | 10-20 |
| 15 | 30° | Ti/Pt | 100/1000 | 10/10 | 9 | 630 | None | - |
| 16 | Sputter | TiW | 500 | 2 | 15-20 | - | - | - |
| 17 | Sputter* | TiW | 500 | 0.07 | 15-20 | 620 | None | - |

**Table 8.2:** A summary of hard contact readout results from device coatings. A full $V_{o,ss}$ means maximum amplitude of the amplifier. Chip 16 was short-circuited during the normal sputter-deposition and could not be tested. Chip 8 is of UV-type A whereas the rest are of UV-type B. Chip 9-11 is from a batch different than the rest resulting in different resonant frequencies of these structures.

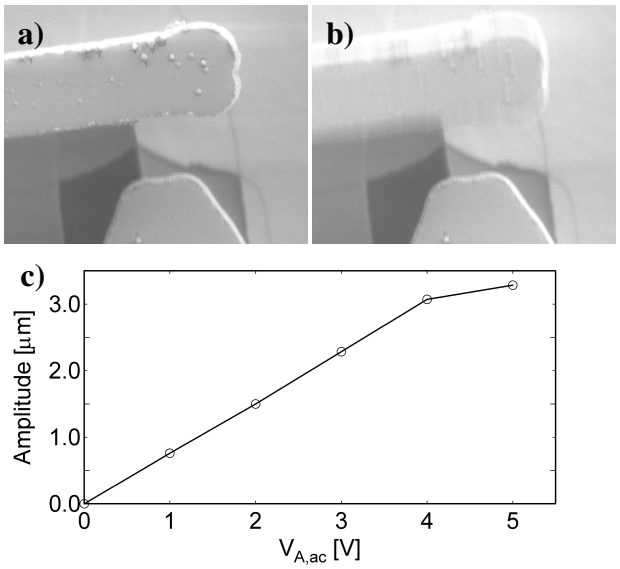


**Figure 8.7:** SEM images of a cantilever from chip 14 off resonance, 649kHz (a) and approximately on resonance, 650.5kHz (b). The measured amplitude for different levels of $V_{A,ac}$ and $V_{A,dc}$ = 5V on resonance (c).

### 8.2.2 Sources of Failure - Increase in $R_c$

It was established that the cantilever was indeed touching the electrode during the measurements and the cantilever showed no signs of cracking. Then, the cause of failure had to be due to an increase in contact resistance.

The surface in the contact area of both the cantilever and the electrode was carefully examined in a SEM. Typical images can be seen in figure 8.8, where no sign of peeling or wear of the metal coating is evident.

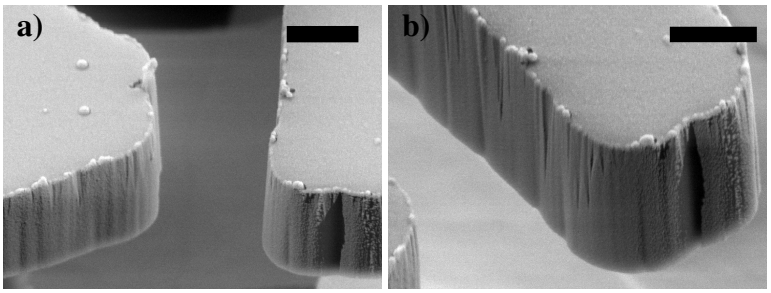


**Figure 8.8:** The contact area on the readout-electrode (a) and cantilever (b) after measurements, where the output signal has disappeared. No signs of peeling or damage can be seen in the SEM. The scale bar is 1$\mu$m in both images.

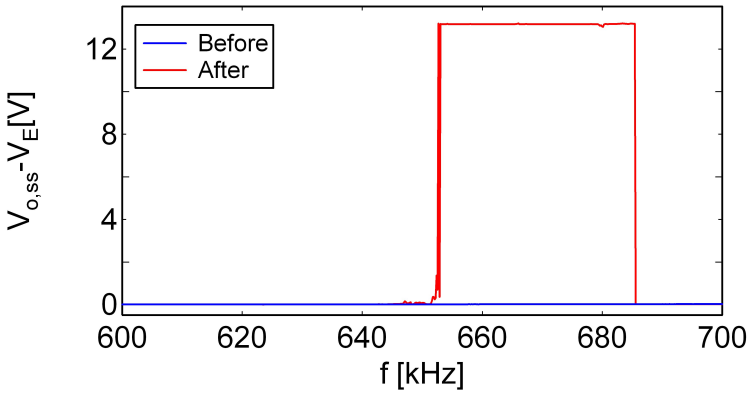


**Figure 8.9:** Measurements prior to and after a 15minutes UV/Ozone cleaning with the same measurement parameters. Before the cleaning no signal was obtained during measurements, but afterwards a signal is obtained in a wide frequency range.

Chip 14 containing the cantilever from figure 8.7 was exposed to a UV/Ozone cleaning for 15minutes. Immediately after the cleaning a measurement was performed, and a large signal was detected at the resonant frequency. The frequency response before and after UV/Ozone cleaning is shown in figure 8.9.

### 8.2.3 Summary and Discussion

In this section, the surface coatings were reviewed and the best coating tested was found to be Pt deposited at an angle of 30° with a thickness of 500Å or deposited using sweep deposition with a thickness of 3000Å. The measured voltage using hard contact readout was seen to decay exponentially with a characteristic rate of $\sim 10^7$ hits, effectively giving the cantilevers a limited lifetime. No sign of cracks on the cantilever or peeling of the metal was observed and the signal could be fully restored using UV/Ozone cleaning of the chip.

The effect of limited lifetime is also seen in RF-MEMS switches [84–86], and a likely cause is that the water-film on the surface contains contaminations adsorbed from the air [87, 88]. The high field in the contact area of the electrode and cantilever will attract the contaminants, and over time effectively insulate the contact area. UV/Ozone cleaning removes oil, grease, and contamination adsorbed during prolonged exposure to air [89]. That the signal is restored after UV/Ozone cleaning is a strong indication of contaminants on the device surface.

The difference observed between a Au and Pt surface in terms of output signal measured, indicates a difference in the surface properties. Au and Pt have similar

wetting properties, so the difference is probably to be found in the hardness of the metal. That Pt tended to be the most durable is in line with the findings of Bae *et al.* [90] who compared Au and Pt field emitters and found the Pt-emitters to be the most stable. The reason for the many metal coatings that was not able to work with hard contact readout could be found in the different surface properties caused by differences in deposition parameters.

## 8.3 Mass Measurements

To demonstrate the ability of the hard contact readout method to do mass sensing a cantilever with the dimension of $w = 1.8\mu$m, $h = 1.5\mu$m, and $L = 60\mu$m was used (chip 8). For mass loading of the cantilever $\sim 1\mu$m diameter polystyrene beads with an expected mass of $\Delta m = 0.5$pg were used.

The polystyrene beads were positioned on the cantilever using the manipulation setup described in section 6.3. Here, two polystyrene beads were placed on the cantilever one after the other. The SEM image in figure 8.10a shows the apex of the cantilever with both polystyrene beads in place. The polystyrene spheres were deformed by the manipulation but they remained intact.

The frequency responses with none, one, and two polystyrene beads are shown in figure 8.10b. The frequency response of the unloaded cantilever was measured in two successive measurements both having a significant output signal at exactly the same applied frequency (both shown in the figure). The change in resonant frequency for each added polystyrene sphere was $\sim -1.1$kHz, and the reciprocal

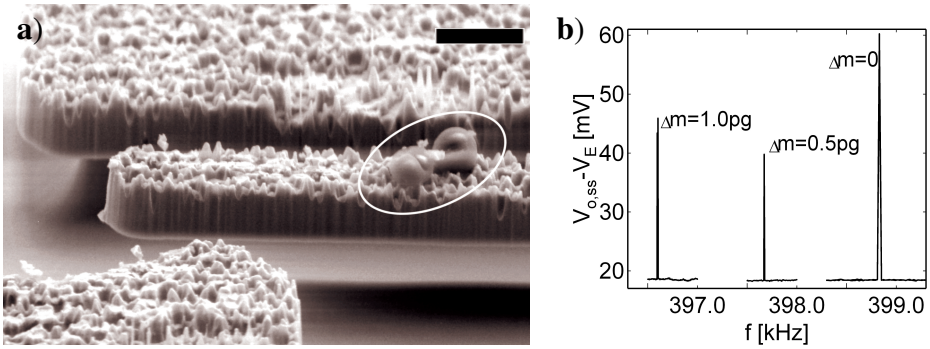


**Figure 8.10:** SEM image of the cantilever apex with two polystyrene beads added (a). The two polystyrene beads are marked with a white ring and are positioned $\sim 7\mu$m from the apex. The scale-bar is 2 $\mu$m long. The frequency response with none, one, and two polystyrene beads on the cantilever found using hard contact readout (b).

relative frequency resolution was 20000< $f_0/\Delta f$ ≤80000. In all measurements $V_{A,ac}$ = 10V and $V_E$ = 1V, while $V_{A,dc}$ = 19.15V.

### 8.3.1 Summary and Discussion

In this section, it was shown possible to measure the mass of individual attached polystyrene beads with a mass of 0.5pg showing a change in resonant frequency of -1.1kHz. The actuation voltage was fine tuned to have a reciprocal relative frequency resolution of 20000< $f_0/\Delta f$ ≤80000, and two successive measurements on the unloaded cantilever gave a significant signal at the same applied frequency.

From the calculated mass responsivity of the cantilever, a frequency shift of $\Delta f_{\Delta m}$ ≈-1kHz is expected from a change in mass of 0.5pg making the change in resonant frequency 10% larger than anticipated. This discrepancy can be caused by a lower effective mass density of the cantilever due to the very rough surface with rather deep holes etched into the cantilever material.

Assuming a totally noiseless system, the hard contact readout method giving a significant signal at only one frequency corresponds to a resonant frequency within $\pm\Delta f_{\text{step}}/2$, where $\Delta f_{\text{step}}$ is the frequency step in the applied frequencies. In these measurements $\Delta f_{\text{step}}$ =20Hz.

The spectral density of the amplitude noise from thermo-mechanical fluctuations of the cantilever can be calculated from equation 2.47 to be $S_{a_n}(\omega_n) \approx 2.6 \cdot 10^{-17}\text{m}^2/(\text{rad/s})$ at a $Q$-factor of 200. From equation 2.53 the spectral density of the frequency noise is calculated to be $S_{\omega_n}(\omega_n) \approx 1.3 \cdot 10^3(\text{rad/s})^2/(\text{rad/s})$, with the cantilever-electrode distance, $d_{ec}$, set equal to the amplitude $a_n(\omega_n) = 1.8\mu$m. In the measurements a step time 300ms was used, so the absolute frequency noise at resonance is from equation 2.58 $\Delta\omega_{min} \approx$ 160rad/s≈25Hz.

The actual noise of the system is thereby comparable to the frequency step in the applied frequencies, and the thermo-mechanical noise seems to be the limiting factor in determination of the frequency in the measurements using hard contact readout.

## 8.4 Scaling Down

The capability of the hard contact readout method to perform readout from nano-scale cantilevers were tested on two different devices called EB-A and EB-B. The silicon based cantilevers fabricated with electron beam lithography are shown in figure 8.11. Both devices have a length of 3.8$\mu$m, and device EB-A is Au coated having a finished width of 225nm and an electrode-cantilever distance of

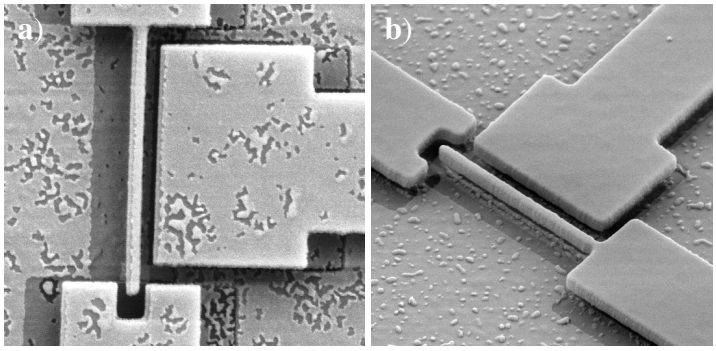


**Figure 8.11:** SEM images of the Si cantilevers used in experiments on hard contact readout. Device EB-A (a) and EB-B (b).

100nm, whereas device EB-B is Pt coated having a finished width of 230nm and an electrode-cantilever distance of 240nm. The cantilevers are not fabricated on the same chip, thus the difference in width.

Measurements were performed in the SEM at a vacuum of $5 \cdot 10^{-6}$mbar using electron beam readout to locate the resonant frequency and subsequently hard contact readout. When testing hard contact readout on EB-A the cantilever stuck to the readout-electrode, but measurements were performed using electron beam readout prior to the sticktion.

For the initial measurement on EB-B with electron beam readout an actuation level of $V_{A,dc}$=7.5V, $V_{A,ac}$=0.5V were used, and a resonant frequency of 11.287MHz were found (figure 8.12a) with a $Q$-factor of ~350. Using $V_{A,dc}$=7.5V, $V_{A,ac}$=1.2V, and $V_E$=0.2V on EB-B the frequency responses were obtained using hard contact readout (figure 8.12b). The resonant frequency was ~ 11.30MHz with a reciprocal relative frequency shift of ~1000. The resonant frequency measured using hard contact readout is thus ~10kHz higher than measured using electron beam readout.

A full output signal is seen in the frequency response using hard contact readout although the signal level is not stable. The maximum output voltage corresponds to a minimum average current of $\overline{I_{\text{in,min}}} \simeq 1\mu$A and a maximum contact resistance of $R_{C,max} \simeq$1.6kΩ can be deduced from the measurements using equation 4.3 and a value of $R$ =20MΩ and assuming $t_c \simeq$ 0.1ns. A similar measurement in a wide range of frequencies on the same device using actuation levels of $V_{A,dc}$=7.5V, $V_{A,ac}$=1.3V and $V_E$=0.2V is shown in figure 8.13. The resonant frequency measured in this case is $f_{res}$ = 11.55MHz, with a signal to noise ratio (SNR) of

$$SNR = \left(\frac{V_{signal,RMS}}{V_{noise,RMS}}\right)^2 = \left(\frac{10V}{1mV}\right)^2 = 10^8 \tag{8.1}$$

in the 1MHz frequency span. For comparison the measurement on the same device using electron beam readout shown in figure 8.12a has a SNR of 2500 despite the high $Q$-factor (For clarity it is put into figure 8.13).

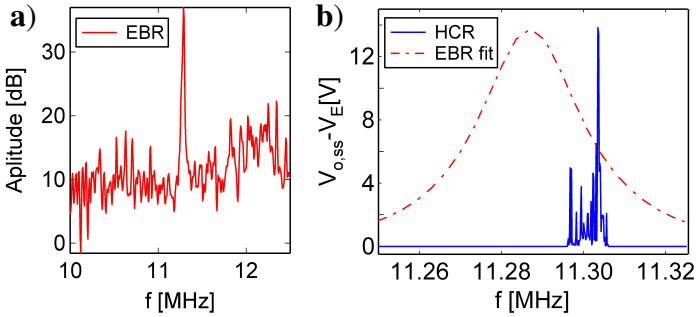


**Figure 8.12:** The frequency response of EB-B obtained using electron beam readout (a). The resonant frequency is 11.287MHz with a $Q$-factor of ~350. The frequency response of EB-B obtained using hard contact readout with the fit of the electron beam readout in red (b). The resonant frequency is 11.3MHz. Actuation levels were $V_{A,dc}$=7.5V, $V_{A,ac}$=1.2V and $V_E$=0.2V for hard contact readout and $V_{A,dc}$=7.5V, $V_{A,ac}$=0.5V for electron beam readout.

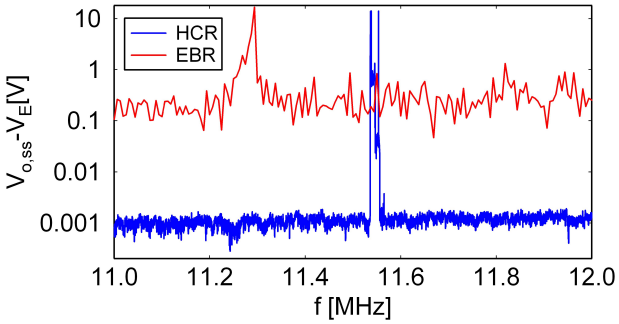


**Figure 8.13:** The frequency response of EB-B using hard contact readout ($V_{A,dc}$=7.5V, $V_{A,ac}$=1.3V and $V_E$=0.2V) compared to that of electron beam readout in a wide frequency range (The electron beam readout signal is scaled to have the same maximum as the hard contact readout signal). The SNR of the hard contact readout measurement in the 1MHz frequency span is $10^8$. In case of electron beam readout it is 2500.

### 8.4.1 Non-linearities

The effect of actuation voltage on the resonant frequency has been investigated on EB-A and EB-B. On EB-A electron beam readout was used to investigate the effect of actuation voltage with no contact between cantilever and readout-electrode, whereas hard contact readout was used on EB-B to investigate the effect of actuation voltage when the amplitude exceeds the cantilever-electrode distance. The results are plotted in figure 8.14.

In figure 8.14a, the square of the resonant frequency of device EB-A is seen to decrease linearly with the time averaged voltage squared, $\left\langle V_{\mathrm{A}}^2 \right\rangle$ in accordance to the theory of spring softening (section 2.3). The slope of the fit is $\sim -10^{10}\mathrm{Hz}^2/\mathrm{V}^2$ with a no-voltage frequency of 10.836MHz, corresponding to a change in resonant frequency of ~-11kHz in the range of $\left\langle V_{\mathrm{A}}^2 \right\rangle$ measured.

In figure 8.14b, the resonant frequency of device EB-B is seen to increase with the applied actuation voltage. The point at $2V_{\mathrm{A},dc}V_{\mathrm{A},ac}$=7.5V$^2$ is obtained using electron beam readout. The theoretical effect on the resonant frequency due to spring hardening scaled down to 7.5% (equation 2.39) is shown with the measured data, and it is assumed that the unconstrained amplitude is $a_n \propto V_{\mathrm{A},dc}V_{\mathrm{A},ac}$. Fitted with a linear function (not shown in the figure), the slope of the fit is $\sim$ 50kHz/V$^2$ with a no-voltage frequency of 10.5MHz.

On the nano-scale cantilevers a difference in resonant frequency and signal is seen depending on the sweep direction. In figure 8.15 the frequency response of EB-B using hard contact readout sweeping both up and down with the same actuation signals is shown. When sweeping upwards, the maximum signal is high and reached after a rather long ramp-up period compared to when sweeping down, where the maximum signal is much smaller. The signal when sweeping down are similar to the ramp-up period seen when sweeping up. The effect is highly repro-

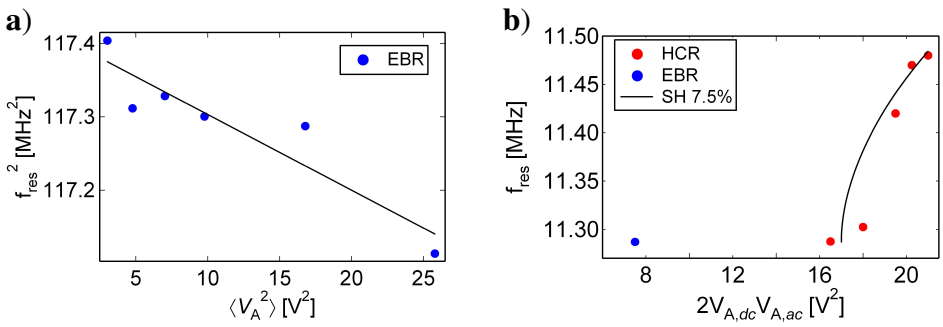


**Figure 8.14:** The resonant frequency of EB-A found by electron beam readout as a function of the time averaged voltage squared, $\left\langle V_{\mathrm{A}}^2 \right\rangle$ (a). The resonant frequency of EB-B found using hard contact readout as a function of $2V_{\mathrm{A},dc}V_{\mathrm{A},ac}$ (b).

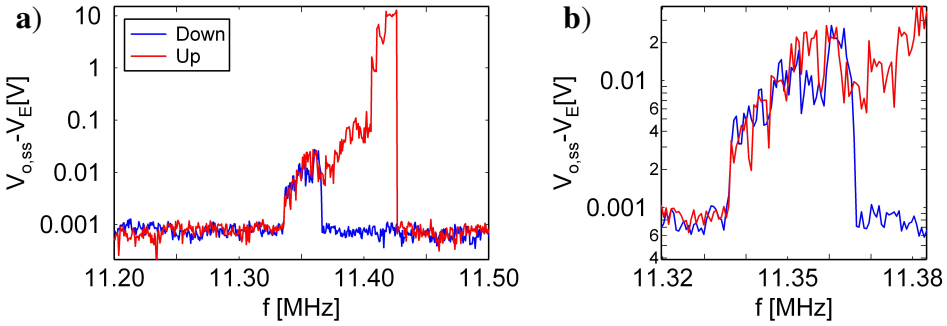


**Figure 8.15:** hard contact readout measurements with different sweep direction on EB-B (a) and a closeup of the sweeping down maximum (b) ($V_{A,dc}$=7.5V, $V_{A,ac}$=1.3V and $V_E$=0.2V). When sweeping up, a large maximum signal is seen with a rather long period of ramping up. When sweeping down, the maximum signal i smaller but is reached immediately, and the signal level equal to that of the sweeping up.

ducible and can also be seen visually in the SEM as a longer period of resonance when sweeping up compared to when sweeping down.

The difference in resonant frequency as a function of sweep direction was also tested using electron beam readout on EB-B. With actuation levels of $V_{A,dc}$=7.5V and $V_{A,ac}$=1.25V the resonant frequency when sweeping upwards was 6-7±1kHz higher than when sweeping down.

### 8.4.2 Summary and Discussion

It was shown possible to do readout from nano-scale cantilevers using hard contact readout. A wide frequency sweep gave a full signal output indicating a minimum average current of $\sim 1\mu$A with a SNR of $10^8$. A decrease in resonant frequency with the applied voltage was observed when the maximum amplitude was smaller than the cantilever-electrode distance. An increase was observed when the cantilever had an amplitude equal to the cantilever-electrode distance. The resonant frequency was seen to depend on the sweep direction.

Device EB-A were seen to stick to the electrode during measurements using hard contact readout. The sticktion coefficient of this device was far less than 1, and thereby expected from the proposed design rule (equation 4.5). On the other hand, device EB-B was not seen to stick even though the designed sticktion coefficient was only 0.58, but this is due to the fact that the width of the finished device was somewhat bigger than designed for thereby effectively increasing the sticktion coefficient.

The decrease in apparent resonant frequency with applied voltage seen when doing electron beam readout, is related to the spring softening effect caused by the position dependent actuation force. The theoretical effect of the actuation voltage can be calculated from equation 2.37 to be -150kHz going from $\left\langle V_{\mathrm{A}}^2 \right\rangle$=3V$^2$ to $\left\langle V_{\mathrm{A}}^2 \right\rangle$=26V$^2$. This is more than 10 times larger than the observed effect. However, the measured change is in good agreement with results obtained by others [34,62].

The increase in apparent resonant frequency observed when doing hard contact readout, is more than an order of magnitude larger than the effect of spring softening. The calculated spring hardening effect was fitted to the measured data points and had to be scaled down to 7.5% for a nice fit. The measurements points are to few and scattered to conclude if the effect on the resonant frequency is behaving as proposed in section 2.3. However, it is reasonable to conclude that at contact the resonant frequency is shifted considerably when the force at impact is high. A carefully tuning of the actuation voltage is thus necessary to minimize the spring hardening effect.

The difference in resonant frequency measured using electron beam readout and the difference in signal level using hard contact readout for different sweep directions, is due to the non-linear forces on the cantilever. The behavior is described by the Duffing spring behavior in non-linear systems [50, 62, 64, 91, 92]. The non-linear forces on the cantilever leads to a hysteretic frequency response, and if the spring hardening effect is dominating the resonant frequency is shifted upwards with increasing amplitude. When reversing the sweep direction the very high amplitude is newer achieved, and the force at impact is smaller leading to a smaller hard contact readout signal. The same phenomena can be caused by the nonlinear nature of the capacitive actuation [59, 62–64], but in this case the resonant frequency is shifted downwards.

# Chapter 9

# Conclusion and Outlook

The aim of this Ph.D. project was to develop a readout method suitable for a portable device and to investigate the possibility of enhancing the functionality of cantilever based mass sensors. During the project 7 articles (4 as a first author) have been published in peer reviewed international journals as well as 10 publications in proceedings.

The theory of dynamic cantilever sensing has been presented and the effect of forces on the cantilever has been discussed including non-linearities in the frequency response arising with non-linear forces. The effect of dissipation on the $Q$-factor as well as noise has been discussed in the context of sensitivity of the cantilever based mass sensor.

A theory for the position dependent mass responsivity of cantilever based mass sensors has been developed. It was shown theoretical possible to use this for accurate determination of both mass and position of attached particles applicable to single molecule detection.

The theory and principles behind a novel approach to do readout from cantilever based mass sensors have been presented. It was shown theoretically that the approach can be used on the micro- as well as the nano-scale level since the output signal has no or very little dependence on the resonant frequency.

### Position and Mode Dependence

It was found that the sensitivity of a cantilever based mass sensor increases with the mode of operation, and operation at higher modes is thereby a simple way to improve the sensitivity of a cantilever based mass sensor. This could be used as a complementary tool to scaling down the cantilever.

In addition, the mass and position of an attached particle could be found with high

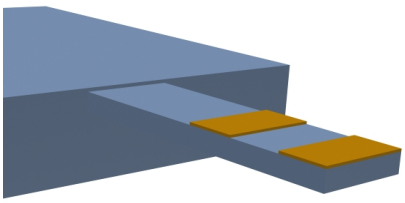

**Figure 9.1:** A nano-nose on a single cantilever is a possible application of the ability to determine the position of the attached mass. A cantilever based mass sensor with several coated areas for sensing of specific but different target molecules (2 areas are shown).

accuracy, and the method could very well be applied to single-cell measurements, where a very exact mass of the particle is needed without determining the position. This could equally well be used for determining the mass of cells or particles flowing inside the cantilever as demonstrated by Burg *et al.* [48].

The method could prove very useful for enhancing the functionality of cantilever based mass sensor. This could be achieved by having several areas on the cantilevers coated for sensing of specific and different target molecules as shown in figure 9.1. By measuring on several modes during operation, the binding of desired targets in one area could be differentiated from binding in other areas. In principle, this would make it possible to design an artificial nose [4, 5] using only a single cantilever.

### Hard Contact Readout

Hard contact readout was used with success for the measurements of the resonant frequency of cantilevers on both the micro- and nano-scale. Resonant frequencies up to 11.5MHz were measured with a full output signal, and masses of 0.5pg were measured to cause a frequency shift of -1.1kHz. Issues of sticktion were seen to be avoidable if the proposed design rule were used.

Values of the reciprocal frequency resolution as high as 80000 was obtained as well as a large SNR of $10^8$. The result is an almost digital readout, which in turn simplifies the detection of the resonant frequency considerably. This property could prove extremely useful in real cantilever based mass sensor applications, where the cantilever is coated with a metal on which the functionalization takes place. The metal coating decreases the $Q$-factor of the device considerably, but

using hard contact readout the determination of the resonant frequency is straightforward. However, even though the readout is almost digital, the intrinsic sensitivity of the cantilever is not improved by this method.

Severe non-linear effects were observed during measurements, caused by the large actuation voltages, the large cantilever deflections, and the electrode-cantilever contact. The observed non-linear effects seem reproducible. By maintaining the same actuation levels and sweep direction for all measurements, these effects will not pose a problem, and hard contact readout could be applicable to reliable mass measurements.

The lifetime of the cantilevers were seen to be limited, due to a decrease in output voltage. Pt coated surfaces tended to be the most durable and the functionality of the cantilevers could be fully restored by UV/Ozone cleaning, indicating that surface contaminants are the main cause of failure. A solution to the problem of surface contaminants could be to coat the clean and dry cantilever surface with a conducting molecule that is highly hydrophobic. Even with no coating, hard contact readout could be suitable for single measurements where the signal is not to be measured over longer periods of time. If to be used for long period measurements a cleaning system should be integrated.

Compared to other electronic readout methods the main advantage of the hard contact method is that a large dc current is measured. Therefore, simple low-bandwidth off-chip electronics can be used and unavoidable parasitic/stray capacitances do not affect the frequency resolution. Hence, scaling to very high resonant frequency NEMS cantilevers is straightforward. Since delicate alignment of the cantilever chip to the detection system is not required, system integration is easily facilitated, especially for portable systems where the cantilever chip is a consumable. In such applications, this method may compete favorably with optical detection methods.

A portable system based on the hard contact method combined with readout at higher bending modes [47] operated in ambient conditions could prove very sensitive and economical. A proposed system is shown in figure 9.2 where the actuation is performed using out-of-plane electrostatic actuation [79] and the readout-electrode is positioned below the cantilever. The device should be fabricated on a SOI wafer, coating the backside and $SiO_2$ tip with TiW using sputter-deposition. Every fabrication step could be performed using standard wet-chemistry whereby it is possible to batch fabricate the device.

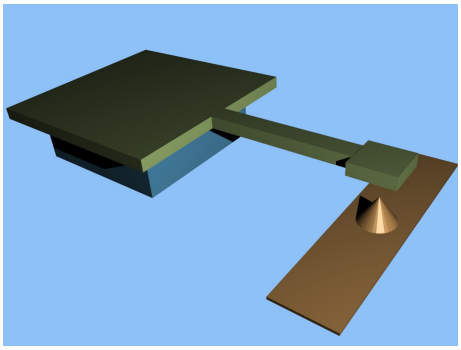

**Figure 9.2:** A possible future cantilever based mass sensor with integrated readout by hard contact readout.

### General

The ultimate goal of this work, have been to make cantilever based mass sensor the method of choice for sensitive mass sensors. However, which sensing method that is the best is highly dependent on the area of interest. There exists plenty of alternatives to the cantilever based mass sensor that could be better at some applications. For instance when there are high concentrations of the target (surface acoustic wave sensors [93], quartz crystal microbalance [23]) or the measurement will take place in water (quartz crystal microbalance [23], bulk-resonators [94], static mode cantilever based sensors [95], surface plasmon resonance sensors [96]).

The one area where the unbeatable sensitivity of the cantilever based mass sensor will be able to make a difference, is in single molecule detection and demonstration and investigation of Quantum mechanical effects [97]. A combination of the hard contact readout and operation at higher bending modes could prove to be very competitive for particle sensors operated at ambient conditions. The method of operation could be utilized for real-time mass distribution measurements of nano-particles with a diameter down to 1nm - a measurement type that is currently not achievable in any other way. By operating the cantilevers in massive arrays the sensors could also prove useful for high sensitivity detection of highly volatile compounds such as explosives and nerve gasses where the target molecules are usually present in air at extremely low concentrations.

Still the issue of achieving selectivity by surface modification or coating is to be solved before cantilever based mass sensors can be used as true reliable bio/chemical sensors.

# Bibliography


[1] G. F. Amelio, M. F. Tompsett, and G. E. Smith. Experimental verification of charge coupled device concept. *Bell System Technical Journal*, 49(4):593–+, 1970.

[2] M. Mullenborn, P. Rombach, U. Klein, K. Rasmussen, J. F. Kuhmann, M. Heschel, M. A. Gravad, J. Janting, J. Branebjerg, A. C. Hoogerwerf, and S. Bouwstra. Chip-size-packaged silicon microphones. *Sensors and Actuators A-Physical*, 92(1-3):23–29, 2001.

[3] P. Rombach, M. Mullenborn, U. Klein, and K. Rasmussen. The first low voltage, low noise differential silicon microphone, technology development and measurement results. *Sensors and Actuators A-Physical*, 95(2-3):196–201, 2002.

[4] H. P. Lang, M. K. Baller, R. Berger, C. Gerber, J. K. Gimzewski, F. M. Battiston, P. Fornaro, J. P. Ramseyer, E. Meyer, and H. J. Guntherodt. An artificial nose based on a micromechanical cantilever array. *Analytica Chimica Acta*, 393(1-3):59–65, 1999.

[5] M. K. Baller, H. P. Lang, J. Fritz, C. Gerber, J. K. Gimzewski, U. Drechsler, H. Rothuizen, M. Despont, P. Vettiger, F. M. Battiston, J. P. Ramseyer, P. Fornaro, E. Meyer, and H. J. Guntherodt. A cantilever array-based artificial nose. *Ultramicroscopy*, 82(1-4):1–9, 2000.

[6] M. Roukes. Nanoelectromechanical systems face the future. *Physics World*, 14(2):25–31, 2001.

[7] H. B. Peng, C. W. Chang, S. Aloni, T. D. Yuzvinski, and Y. Zhang. Ultrahigh frequency nantoube resonator. *Physical Review Letters*, 97:087203, 2006.

[8] S. J. Oshea, M. E. Welland, T. A. Brunt, A. R. Ramadan, and T. Rayment. Atomic force microscopy stress sensors for studies in liquids. *Journal of Vacuum Science & Technology B*, 14(2):1383–1385, 1996.

[9] J. Fritz, M. K. Baller, H. P. Lang, H. Rothuizen, P. Vettiger, E. Meyer, H. J. Guntherodt, C. Gerber, and J. K. Gimzewski. Translating biomolecular recognition into nanomechanics. *Science*, 288(5464):316–318, 2000.

[10] J. K. Gimzewski, C. Gerber, E. Meyer, and R. R. Schlittler. Observation of a chemical-reaction using a micromechanical sensor. *Chemical Physics Letters*, 217(5-6):589–594, 1994.

[11] J. R. Barnes, R. J. Stephenson, M. E. Welland, C. Gerber, and J. K. Gimzewski. Photothermal spectroscopy with femtojoule sensitivity using a micromechanical device. *Nature*, 372(6501):79–81, 1994.

[12] R. Berger, C. Gerber, J. K. Gimzewski, E. Meyer, and H. J. Guntherodt. Thermal analysis using a micromechanical calorimeter. *Applied Physics Letters*, 69(1):40–42, 1996.

[13] G. Binnig, C. F. Quate, and C. Gerber. Atomic force microscope. *Physical Review Letters*, 56(9):930–933, 1986.

[14] E. Forsen. *Nano-cantilevers fully integrated with CMOS for ultrasensitive mass detection*. Thesis/dissertation, Department of Micro and Nanotechnology, 2005.

[15] G. Meyer and N. M. Amer. Novel optical approach to atomic force microscopy. *Applied Physics Letters*, 53(12):1045–1047, 1988.

[16] G. Y. Chen, T. Thundat, E. A. Wachter, and R. J. Warmack. Adsorption-induced surface stress and its effects on resonance frequency of microcantilevers. *Journal of Applied Physics*, 77(8):3618–3622, 1995.

[17] T. Thundat, E. A. Wachter, S. L. Sharp, and R. J. Warmack. Detection of mercury-vapor using resonating microcantilevers. *Applied Physics Letters*, 66(13):1695–1697, 1995.

[18] T. Ono, X. X. Li, H. Miyashita, and M. Esashi. Mass sensing of adsorbed molecules in sub-picogram sample with ultrathin silicon resonator. *Review of Scientific Instruments*, 74(3):1240–1243, 2003.

[19] B. Ilic, D. Czaplewski, M. Zalalutdinov, H. G. Craighead, P. Neuzil, C. Campagnolo, and C. Batt. Single cell detection with micromechanical oscillators. *Journal of Vacuum Science & Technology B*, 19(6):2825–2828, 2001.

[20] K. L. Ekinci, X. M. H. Huang, and M. L. Roukes. Ultrasensitive nanoelectromechanical mass detection. *Applied Physics Letters*, 84(22):4469–4471, 2004.

[21] Y. T. Yang, C. Callegari, X. L. Feng, K. L. Ekinci, and M. L. Roukes. Zeptogram-scale nanomechanical mass sensing. *Nano Letters*, 6(4):583–586, 2006.

[22] M. L. Roukes. Very-high-frequency nanocantilevers: Advances, physics, & applications. In *International workshop on Nanomechanical Sensors*, 2006.

[23] M. rodahl, F. Hook, A. Krozer, P. Brzezinski, and B. Kazemo. Quartz-crystal microbalance setup for frequency and q-factor measurements in gaseous and liquid environments. *Review of Scientific Instruments*, 66(7):3924–3930, 1995.

[24] F. R. Blom, S. Bouwstra, M. Elwenspoek, and J. H. J. Fluitman. Dependence of the quality factor of micromachined silicon beam resonators on pressure and geometry. *Journal of Vacuum Science & Technology B*, 10(1):19–26, 1992.

[25] R. Sandberg, K. Molhave, A. Boisen, and W. Svendsen. Effect of gold coating on the q-factor of a resonant cantilever. *Journal of Micromechanics and Microengineering*, 15(12):2249–2253, 2005.

[26] C. A. J. Putman, B. G. Degrooth, N. F. Vanhulst, and J. Greve. A detailed analysis of the optical beam deflection technique for use in atomic force microscopy. *Journal of Applied Physics*, 72(1):6–12, 1992.

[27] R. G. Beck, M. A. Eriksson, M. A. Topinka, R. M. Westervelt, K. D. Maranowski, and A. C. Gossard. Gaas/algaas self-sensing cantilevers for low temperature scanning probe microscopy. *Applied Physics Letters*, 73(8):1149–1151, 1998.

[28] A. N. Cleland and M. L. Roukes. External control of dissipation in a nanometer-scale radiofrequency mechanical resonator. *Sensors and Actuators A-Physical*, 72(3):256–261, 1999.

[29] H. Jensenius, J. Thaysen, A. A. Rasmussen, L. H. Veje, O. Hansen, and A. Boisen. A microcantilever-based alcohol vapor sensor-application and response model. *Applied Physics Letters*, 76(18):2615–2617, 2000.

[30] Y. Zhang and M. P. Blencowe. Intrinsic noise of a micromechanical displacement detector based on the radio-frequency single-electron transistor. *Journal of Applied Physics*, 91(7):4249–4255, 2002.

[31] S. Ghatnekar-Nilsson, E. Forsen, G. Abadal, J. Verd, F. Campabadal, F. Perez-Murano, J. Esteve, N. Barniol, A. Boisen, and L. Montelius. Resonators with integrated cmos circuitry for mass sensing applications, fabricated by electron beam lithography. *Nanotechnology*, 16(1):98–102, 2005.

[32] G. Stemme. Resonant silicon sensors. *Journal of Microelectromechanical Engineering*, 1:113–125, 1991.

[33] Z. J. Davis, G. Abadal, O. Kuhn, O. Hansen, F. Grey, and A. Boisen. Fabrication and characterization of nanoresonating devices for mass detection. *Journal of Vacuum Science & Technology B*, 18(2):612–616, 2000.

[34] E. Forsen, G. Abadal, S. Ghatnekar-Nilsson, J. Teva, J. Verd, R. Sandberg, W. Svendsen, F. Perez-Murano, J. Esteve, E. Figueras, F. Campabadal, L. Montelius, N. Barniol, and A. Boisen. Ultrasensitive mass sensor fully integrated with complementary metal-oxide-semiconductor circuitry. *Applied Physics Letters*, 87(4), 2005.

[35] T. Itoh, T. Ohashi, and T. Suga. Noncontact scanning force microscopy using a direct-oscillating piezoelectric microcantilever. *Journal of Vacuum Science & Technology B*, 14(3):1577–1581, 1996.

[36] C. K. Lee, T. Itoh, R. Maeda, and T. Suga. Characterization of micromachined piezoelectric pzt force sensors for dynamic scanning force microscopy. *Review of Scientific Instruments*, 68(5):2091–2100, 1997.

[37] H. A. C. Tilmans, M. Elwenspoek, and J. H. J. Fluitman. Micro resonant force gauges. *Sensors and Actuators A-Physical*, 30(1-2):35–53, 1992.

[38] R. R. A. Syms. Long-travel electrothermally driven resonant cantilever microactuators. *Journal of Micromechanics and Microengineering*, 12(3):211–218, 2002.

[39] J. D. Zook, D. W. Burns, W. R. Herb, H. Guckel, J. W. Kang, and Y. C. Ahn. Optically excited self-resonant microbeams. *Sensors and Actuators A-Physical*, 52(1-3):92–98, 1996.

[40] T. Kouh, D. Karabacak, D. H. Kim, and K. L. Ekinci. Diffraction effects in optical interferometric displacement detection in nanoelectromechanical systems. *Applied Physics Letters*, 86(1), 2005.

[41] D. Karabacak, T. Kouh, and K. L. Ekinci. Analysis of optical interferometric displacement detection in nanoelectromechanical systems. *Journal of Applied Physics*, 98(12), 2005.

[42] D. Karabacak, T. Kouh, C. C. Huang, and K. L. Ekinci. Optical knife-edge technique for nanomechanical displacement detection. *Applied Physics Letters*, 88(19), 2006.

[43] A. N. Cleland and M. L. Roukes. Fabrication of high frequency nanometer scale mechanical resonators from bulk si crystals. *Applied Physics Letters*, 69(18):2653–2655, 1996.

[44] P. Mohanty, D. A. Harrington, K. L. Ekinci, Y. T. Yang, M. J. Murphy, and M. L. Roukes. Intrinsic dissipation in high-frequency micromechanical resonators. *Physical Review B*, 66(8), 2002.

[45] T. Kemp and M. Ward. Tunable response nano-mechanical beam resonator. *Sensors and Actuators A-Physical*, 123-24:281–284, 2005.

[46] J. Teva, G. Abadal, F. Torres, J. Verd, F. Perez-Murano, and N. Barniol. A femtogram resolution mass sensor platform based on soi electrostatically driven resonant cantilever. part ii: Sensor calibration and glycerine evaporation rate measurement. *Ultramicroscopy*, 106(8-9):808–814, 2006.

[47] S. Dohn, R. Sandberg, W. Svendsen, and A. Boisen. Enhanced functionality of cantilever based mass sensors using higher modes. *Applied Physics Letters*, 86(23), 2005.

[48] T. P. Burg and S. R. Manalis. Suspended microchannel resonators for biomolecular detection. *Applied Physics Letters*, 83(13):2698–2700, 2003.

[49] W. C. Young, R. G. Budynas, and R. J. Roark. *Roark's formulas for stress and strain*. McGraw-Hill., Boston, 7 edition, 2002.

[50] A N. Cleland. *Foundations of Nanomechanics*. Springer, Berlin, 2003.

[51] K. L. Ekinci, Y. T. Yang, and M. L. Roukes. Ultimate limits to inertial mass sensing based upon nanoelectromechanical systems. *Journal of Applied Physics*, 95(5):2682–2689, 2004.

[52] K. Y. Yasumura, T. D. Stowe, E. M. Chow, T. Pfafman, T. W. Kenny, B. C. Stipe, and D. Rugar. Quality factors in micron- and submicron-thick cantilevers. *Journal of Microelectromechanical Systems*, 9(1):117–125, 2000.

[53] R. Lifshitz and M. L. Roukes. Thermoelastic damping in micro- and nanomechanical systems. *Physical Review B*, 61(8):5600–5609, 2000.

[54] D. M. Photiadis and J. A. Judge. Attachment losses of high q oscillators. *Applied Physics Letters*, 85(3):482–484, 2004.

[55] M. Calleja, M. Nordstrom, M. Alvarez, J. Tamayo, L. M. Lechuga, and A. Boisen. Highly sensitive polymer-based cantilever-sensors for dna detection. *Ultramicroscopy*, 105(1-4):215–222, 2005.

[56] J. L. Yang, T. Ono, and M. Esashi. Energy dissipation in submicrometer thick single-crystal silicon cantilevers. *Journal of Microelectromechanical Systems*, 11(6):775–783, 2002.

[57] J. L. Yang, T. Ono, and M. Esashi. Mechanical behavior of ultrathin microcantilever. *Sensors and Actuators A-Physical*, 82(1-3):102–107, 2000.

[58] J. W. M. Chon, P. Mulvaney, and J. E. Sader. Experimental validation of theoretical models for the frequency response of atomic force microscope cantilever beams immersed in fluids. *Journal of Applied Physics*, 87(8):3978–3988, 2000.

[59] S. K. De and N. R. Aluru. Full-lagrangian schemes for dynamic analysis of electrostatic mems. *Journal of Microelectromechanical Systems*, 13(5):737–758, 2004.

[60] J. Berg and G. A. D. Briggs. Nonlinear dynamics of intermittent-contact mode atomic force microscopy. *Physical Review B*, 55(22):14899–14908, 1997.

[61] S. I. Lee, S. W. Howell, A. Raman, and R. Reifenberger. Nonlinear dynamic perspectives on dynamic force microscopy. *Ultramicroscopy*, 97(1-4):185–198, 2003.

[62] J. J. Yao and N. C. Macdonald. A micromachined, single-crystal silicon, tunable resonator. *Journal of Micromechanics and Microengineering*, 5(3):257–264, 1995.

[63] D. Scheibner, J. Mehner, D. Reuter, U. Kotarsky, T. Gessner, and W. Dotzel. Characterization and self-test of electrostatically tunable resonators for frequency selective vibration measurements. *Sensors and Actuators A-Physical*, 111(1):93–99, 2004.

[64] I. Kozinsky, H. W. C. Postma, I. Bargatin, and M. L. Roukes. Tuning nonlinearity, dynamic range, and frequency of nanomechanical resonators. *Applied Physics Letters*, 88(25), 2006.

[65] J. R. Vig and Y. Kim. Noise in microelectromechanical system resonators. *Ieee Transactions on Ultrasonics Ferroelectrics and Frequency Control*, 46(6):1558–1565, 1999.

[66] A. N. Cleland and M. L. Roukes. Noise processes in nanomechanical resonators. *Journal of Applied Physics*, 92(5):2758–2769, 2002.

[67] Y. K. Yong and J. R. Vig. Modeling resonator frequency fluctuations induced by adsorbing and desorbing surface molecules. *Ieee Transactions on Ultrasonics Ferroelectrics and Frequency Control*, 37(6):543–550, 1990.

[68] S. D. Senturia. Energy methods. In *Microsystem Design*, book chapter 10, pages 239–265. Kluwer Academic Publishers, 4 edition, 2002.

[69] A. Erbe, R. H. Blick, A. Tilke, A. Kriele, and J. P. Kotthaus. A mechanically flexible tunneling contact operating at radio frequencies. *Applied Physics Letters*, 73(25):3751–3753, 1998.

[70] W. P. Maszara, G. Goetz, A. Caviglia, and J. B. Mckitterick. Bonding of silicon-wafers for silicon-on-insulator. *Journal of Applied Physics*, 64(10):4943–4950, 1988.

[71] S. Datta. *Electronic Transport in Mesoscopic Systems*. Cambridge University Press, 1995.

[72] A. G. Hansen, M. W. Mortensen, J. E. T. Andersen, J. Ulstrup, A. Kühle, J. Garnæs, and A. Boisen. Stress formation during self-assembly of alkanethiols on differently pre-treated gold surfaces. *Probe microscope*, 2:139–149, 2001.

[73] E. Forsen, Z. J. Davis, M. Dong, S. G. Nilsson, L. Montelius, and A. Boisen. Dry release of suspended nanostructures. *Microelectronic Engineering*, 73-74:487–490, 2004.

[74] L. Gammelgaard, S. Dohn, R. J. Wojtecki, Boisen A., and P. Bøggild. Wafer scale fabrication of suspended tiw nanowires. In *Micro- and Nano- Engineering*, Sep 2006.

[75] R. Sandberg. *Characterization of the Resonant Properties of Multi-layer Cantilever Sensors*. Thesis/dissertation, Department of Micro and Nanotechnology, 2005.

[76] R. Sandberg, A. Boisen, and W. Svendsen. Characterization system for resonant micro- and nanocantilevers. *Review of Scientific Instruments*, 76(12), 2005.

[77] C. L. Petersen, T. M. Hansen, P. Boggild, A. Boisen, O. Hansen, T. Hassenkam, and F. Grey. Scanning microscopic four-point conductivity probes. *Sensors and Actuators A-Physical*, 96(1):53–58, 2002.

[78] E. Buks and M. L. Roukes. Stiction, adhesion energy, and the casimir effect in micromechanical systems. *Physical Review B*, 63(3):art–033402, 2001.

[79] Z. J. Davis and A. Boisen. Aluminum nanocantilevers for high sensitivity mass sensors. *Applied Physics Letters*, 87(1):013102–1–013102–3, 2005.

[80] S. Dohn, J. Kjelstrup-Hansen, D. N. Madsen, K. Mølhave, and P. Bøggild. Multiwalled carbon nanotubes integrated in microcantilevers for application of tensile strain. *Ultramicroscopy*, 105:209–214, 2005.

[81] J. Kjelstrup-Hansen, S. Dohn, D. N. Madsen, K. Molhave, and P. Boggild. Versatile method for manipulating and contacting nanowires. *Journal of Nanoscience and Nanotechnology*, 6(7):1995–1999, 2006.

[82] L. B. Sharos, A. Raman, S. Crittenden, and R. Reifenberger. Enhanced mass sensing using torsional and lateral resonances in microcantilevers. *Applied Physics Letters*, 84(23):4638–4640, 2004.

[83] R. Sandberg, W. Svendsen, K. Molhave, and A. Boisen. Temperature and pressure dependence of resonance in multi-layer microcantilevers. *Journal of Micromechanics and Microengineering*, 15(8):1454–1458, 2005.

[84] C. L. Goldsmith, Z. M. Yao, S. Eshelman, and D. Denniston. Performance of low-loss rf mems capacitive switches. *Ieee Microwave and Guided Wave Letters*, 8(8):269–271, 1998.

[85] F. M. Guo, Z. Q. Zhu, Y. F. Long, W. M. Wang, S. Z. Zhu, Z. S. Lai, N. Li, G. Q. Yang, and W. Lu. Study on low voltage actuated mems rf capacitive switches. *Sensors and Actuators A-Physical*, 108(1-3):128–133, 2003.

[86] R. Chan, R. Lesnick, D. Becher, and M. Feng. Low-actuation voltage rf mems shunt switch with cold switching lifetime of seven billion cycles. *Journal of Microelectromechanical Systems*, 12(5):713–719, 2003.

[87] S. T. Patton and J. S. Zabinski. Fundamental studies of au contacts in mems rf switches. *Tribology Letters*, 18(2):215–230, 2005.

[88] S. T. Patton and J. S. Zabinski. Failure mechanisms of capacitive mems rf switch contacts. *Tribology Letters*, 19(4):265–272, 2005.

[89] J. R. Vig. Uv ozone cleaning of surfaces. *Journal of Vacuum Science & Technology A-Vacuum Surfaces and Films*, 3(3):1027–1034, 1985.

[90] S. C. Bae and S. Y. Choi. Improvement of the field emission characteristics of an oxidized porous polysilicon using annealed pt/ti surface emitter electrode. *Microelectronics Journal*, 37(2):167–173, 2006.

[91] V. Kaajakari, T. Mattila, A. Oja, and H. Seppa. Nonlinear limits for single-crystal silicon microresonators. *Journal of Microelectromechanical Systems*, 13(5):715–724, 2004.

[92] J. H. Zhao, G. E. Bridges, and D. J. Thomson. Direct evidence of "spring softening" nonlinearity in micromachined mechanical resonator using optical beam deflection technique. *Journal of Vacuum Science & Technology A*, 24(3):732–736, 2006.

[93] J. W. Grate and M Klusty. Surface acoustic-wave vapor sensors based on resonator devices. *Analytical Chemistry*, 63(17):1719–1727, 1991.

[94] T. Mattila, J. Kiihamaki, T. Lamminmaki, O. Jaakkola, P. Rantakari, A. Oja, H. Seppa, H. Kattelus, and I. Tittonen. A 12 mhz micromechanical bulk acoustic mode oscillator. *Sensors and Actuators A-Physical*, 101(1-2):1–9, 2002.

[95] R. Raiteri, M. Grattarola, H. J. Butt, and P. Skladal. Micromechanical cantilever-based biosensors. *Sensors and Actuators B-Chemical*, 79(2-3):115–126, 2001.

[96] J. Homola, S. S. Yee, and G. Gauglitz. Surface plasmon resonance sensors: review. *Sensors and Actuators B-Chemical*, 54(1-2):3–15, 1999.

[97] K. C. Schwab and M. L. Roukes. Putting mechanics into quantum mechanics. *Physics Today*, 58(7):36–42, 2005.

# Appendix A

# List of Publications

## Articles in International Journals

- **S. Dohn**, O. Hansen, and A. Boisen. Cantilever based mass sensor with hard contact readout. *Applied Physics Letters*, 88(26), 2006.

- J. Kjelstrup-Hansen, **S. Dohn**, D. N. Madsen, K. Molhave, and P. Boggild. Versatile method for manipulating and contacting nanowires. *Journal of Nanoscience and Nanotechnology*, 6(7):1995–1999, 2006.

- S. Sadewasser, G. Abadal, N. Barniol, **S. Dohn**, A. Boisen, L. Fornseca, and J. Esteve. Integrated tunneling sensor for nanoelectromechanical systems. *Applied Physics Letters*, 89(173101):173101–1–173101–3, 2006.

- **S. Dohn**, K. Molhave, and P. Boggild. Direct measurement of resistance of multiwalled carbon nanotubes using micro four-point probes. *Sensor Letters*, 3(4):300–303, 2005.

- **S. Dohn**, R. Sandberg, W. Svendsen, and A. Boisen. Enhanced functionality of cantilever based mass sensors using higher modes. *Applied Physics Letters*, 86(23), 2005.

- **S. Dohn**, J. Kjelstrup-Hansen, D. N. Madsen, K. Mølhave, and P. Bøggild. Multiwalled carbon nanotubes integrated in microcantilevers for application of tensile strain. *Ultramicroscopy*, 105:209–214, 2005.

- K. Molhave, D. N. Madsen, **S. Dohn**, and P. Boggild. Constructing, connecting and soldering nanostructures by environmental electron beam deposition. *Nanotechnology*, 15(8):1047–1053, 2004.

## Abstracts in Peer Reviewed Proceedings

- **S. Dohn**, O. Hansen, and A. Boisen. Cantilever readout by hard contact. In *Micro- and Nano- Engineering*, pages 399–399, MNE 2006 Barcelona, Spain.
- **S. Dohn**, O. Hansen, and A. Boisen. Hard contact readout. In *International Workshop on Nanomechanical Sensors 2006*, International Workshop on Nanomechanical Sensors 2006 Copenhagen, Denmark.
- L. Gammelgaard, **S. Dohn**, R. J. Wojtecki, Boisen A., and P. Bøggild. Wafer scale fabrication of suspended tiw nanowires. In *Micro- and Nano- Engineering*, pages 81–82, MNE 2006 Barcelona, Spain.
- **S. Dohn**, R. Sandberg, W. Svendsen, and A. Boisen. Enhanced functionality of cantilever based mass sensors using higher modes and functionalized particles. In *Solid-State Sensors, Actuators and Microsystems, 2005. Digest of Technical Papers. 1*, pages 636–639, Transducers 2005 Soul, Korea.
- **S. Dohn**, R. Sandberg, W. Svendsen, and A. Boisen. Mass sensitivity of cantilever based mass sensors as a function of mass-position. In *Materials Research Society Symposium - Proceedings*, MRS 2005 San Francisco, USA.
- **S. Dohn**, K. Molhave, D. N. Madsen, R. Mateiu, P. Boggild, A. M. Rasmussen, M. Brorson, and C. J. H. Jacobsen. Soldering of carbon nanotube bridges using electron beam deposited gold. In *Materials Research Society Symposium - Proceedings*, volume 772, pages 153–158, MRS 2003 San Francisco, USA.
- **S. Dohn**, R. Sandberg, W. Svendsen, and A. Boisen. Enhanced functionality of cantilever based mass sensors using higher modes and functionalized particles. Abstract, Transducers 2005 Soul, Korea.
- J. Kjelstrup-Hansen, **S. Dohn**, D. N. Madsen, K. Molhave, and P. Boggild. Microcantilever with integrated carbon nanotube strain sensor. Abstract, MRS 2005 San Francisco, USA.
- **S. Dohn**, D. N. Madsen, K. Molhave, and P. Boggild. Cantilever based strain-sensor using a multiwalled carbon nanotube as piezo-resistive material. Abstract, SPM 2004 Beijing, China.
- **S. Dohn**, J. Kjelstrup-Hansen, D. N. Madsen, and P. Boggild. Investigation of the electro-mechanical properties of multiwalled nanotubes using microcantilevers. Abstract, DFS 2004 Nyborg, Denmark.

# Appendix B

# Coated Cantilevers

When calculating the area moment of inertia in section 2.1 equation 2.10 it was assumed that the cantilever is homogenous in both the length and the cross-section. If, on the other hand, the cantilever is coated with a metal or similar material having a thickness comparable to the dimensions of the cantilever, the coating must be accounted for. A rectangular beam with the dimensions shown in figure B.1 coated with a second material on the top and sides has a spring constant of

$$k = \frac{3\sum_n E_n I_{x,n}}{\mathrm{L}^3}, \tag{B.1}$$

where the summation is over all parts of the cantilever. So the moment area of inertia is calculated for each part and added after multiplication with Young's modulus for the specific part. The coating gives an extra term of

$$\begin{aligned} I_{coat} &= 2\int_0^h \int_{w/2+dw}^{w/2} y^2 dy dx + \int_h^{h+dh} \int_{-w/2-dw}^{w/2+dw} y^2 dy dx \\ &= 2\int_0^h \left[\frac{1}{3}y^3\right]_{w/2+dw}^{w/2} dx + \int_h^{h+dh} \left[\frac{1}{3}y^3\right]_{-w/2-dw}^{w/2+dw} dx \\ &= \frac{h\,(w+2dw)^3 - hw^3 + dh\,(w+2dw)^3}{12} \\ I_{coat} &= \frac{1}{12}(w+2dw)^3\,(h+dh) - \frac{1}{12}hw^3 \end{aligned} \tag{B.2}$$

Giving a total spring constant of

$$k = k_{cant} + k_{coat} = \frac{E_{coat}\,(w+2dw)^3\,(h+dh) + (E_{cant} - E_{coat})hw^3}{4\mathrm{L}^3} \tag{B.3}$$

The effect on the spring constant $k$ of a platinum coating on a silicon or silicon-dioxide cantilever is plotted in figure B.2, assuming that the coating has twice

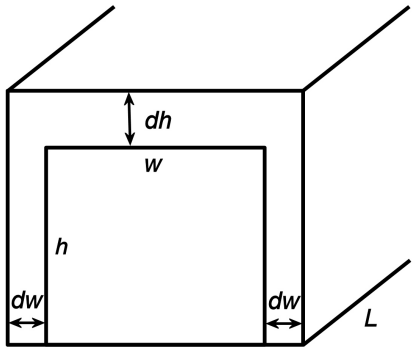


**Figure B.1:** Schematic of a coated cantilever.

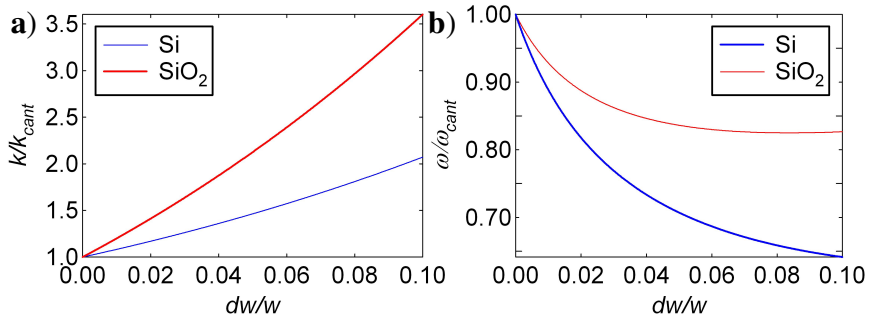


**Figure B.2:** The effect of a platinum-coating on the spring constant (a) and resonant frequency (b) of a cantilever made in Si and $SiO_2$ both with the dimensions of $w$=200nm, $h$=250nm and arbitrary length.

the thickness on the top as on the sides $dw$=2$dh$. In the case of Pt which is rather heavy, the resonant frequency will decrease despite the increase in spring constant. The exact behavior depends highly on the material parameters of the coating and cantilever. Besides the effect on the spring constant a metal coating will increase the dissipation considerably [25].

# Appendix C

# $SiO_2$ Cantilever Process Sequence

1. Starting out with a standard TN108 wafer a thermal oxide is grown at $1150^0$C in a flow of 3slm of H and 2.5slm of O for 12 hours giving a oxide thickness of 2.6$\mu$m.

2. The wafers are pre-treated with a Hexa-dimethylene-di-siloxane at 150˚for 30 minutes to increase the resist adhesion to the oxide.

3. The wafer is spin-coated with a standard az521 resist and baked for 60s at 90˚C creating a 1.5$\mu$m resist layer.

4. The device pattern is transferred to the resist in a negative lithography step involving a reverse-bake at 120˚for 120s, flood exposure for 30s, and a development for 60s followed by a 5 minute rinse in DI-water

5. 400nm Al is deposited using electron-beam evaporation equipment.

6. The remaining resist is removed in a acetone bath, and in this lift-off process the desired device pattern is left on the wafer surface.

7. The device is etched an-isotropically in a AOE in a gas of $C_4F_8$ flowing with 25sccm at a power of 1100W giving an etch rate of approximately 350-400nm/min giving a total etch time of 7 minutes.

8. The remains of the Al etch mask is removed in solution of $H_3PO_4$:$H_2O$.

9. The devices are partly released by two steps of RIE. The first an-isotropic step: 32sccm $SF_6$, 8sccm $O_2$, pressure=80mTorr and power=35W for 10min. The etch rate is 200nm/min with a 1-5% undercut in single crystalline Si. The second isotropic step of RIE: 40sccm $SF_6$, 0sccm $O_2$, pressure=80mTorr and power=35W for 5min.

10. The structures are coated by either tilting the sample to an angle of 30-45˚and coated on both sides of the cantilevers, or by sweeping the sample in front of the metal target during deposition.

# Appendix D

# Si Cantilever Process Sequence

1. Starting out with a commercial available SOI wafer having a top-silicion layer thickness of 220nm and a BOX layer of 450nm

2. The wafer is spin-coated with a ZEP:Anisole 1:1 resist at 3000rpm for 30s and baked for 60s at $160^o$ creating an approximately 100nm resist layer.

3. The device pattern is transferred to the resist in a negative lithography step followed by development for 60s and iso propanol (IPA) rinse.

4. 30nm Al is deposited using electron-beam evaporation equipment.

5. The remaining resist is removed with N1156 Nano-remover, and in this lift-off process the desired device pattern is left on the chip surface.

6. The device is etched an-isotropically by RIE: 32sccm $SF_6$, 8sccm $O_2$, pressure=80mTorr and power=35W. The process have an etch rate in single crystalline silicon of approximately 200nm/min giving a total etch time of 60s.

7. The devices are partly released by exposure to BHF for 4min having a etch rate of 75nm/min.

8. Without allowing the chip to dry it is immersed in acetone and after several rinsing cycles, the chip is transferred to AZ5214e resist. The chip is spun at 3000rpm for 30s followed by a soft-bake at 90˚for 30s.

9. The resist is removed in a oxygen plasma: 99sccm $O_2$, 20sccm $N_2$, pressure 300mTorr and power=60W. The etch rate is 400nm/min.

10. The structures are coated by either tilting the sample to an angle of 30-45˚and coated on both sides of the cantilevers, or by sweeping the sample in front of the metal target during deposition.

# Appendix E

# List of Abbreviations

**AFM** atomic force microscope

**AOE** advanced oxide etching

**BOX** buried oxide

**GPA** gain phase analyzer

**IPA** iso propanol

**MEMS** micro-electro-mechanical system

**NEMS** nano-electro-mechanical system

**PCB** printed circuit board

**PGA** pin grid array

**PSD** position sensitive photo-detector

**PZT** piezo-electric ceramic linear transducer element

$Q$**-factor** quality factor

**RIE** reactive ion etching

**SEM** scanning electron microscope

**SNR** signal to noise ratio

**SOI** Si on insulator

# Appendix F

# Constants

The following table contains the constants used in calculations throughout the thesis. If not stated specifically otherwise, all values are for Si at room temperature.

| **Description** | **Symbol** | **Value** |
|---|---|---|
| Adsorption coefficient (N on Si) | $s$ | 0.1 |
| Adsorption site area | $a_{ads}$ | 0.25nm$^2$ |
| Binding energy (N on Si) | $E_b$ | 42kJ/mol |
| Boltzmann's constant | $k_b$ | $1.380{\cdot}10^{-23}$J/K |
| Damping coefficient | $k_m$ | $3.6{\cdot}10^{-3}$s/m |
| Density Air | $\rho_{air}$ | 1.299kg/m$^3$ |
| Density Au | $\rho_{Au}$ | 19300kg/m$^3$ |
| Density Poly | $\rho_{Poly}$ | 1050kg/m$^3$ |
| Density Pt | $\rho_{Pt}$ | 2144kg/m$^3$ |
| Density Si | $\rho_{Si}$ | 2330kg/m$^3$ |
| Density $SiO_2$ | $\rho_{SiO_2}$ | 2150kg/m$^3$ |
| Density Ti $_2$ | $\rho_{Ti}$ | 4500kg/m$^3$ |
| Desorption coefficient (N on Si) | $v_d$ | $10^{13}$/s |
| Molar weight Air | $m_m$ | $28.964{\cdot}10^{-3}$kg/mol |
| Sound speed | $c_s$ | 5860m/s |
| Vacuum permittivity | $\epsilon_0$ | $8.85{\cdot}10^{-12}$F/m |
| Viscosity Air | $\mu$ | $1.73{\cdot}10^{-5}$N-s/m$^2$ |
| Young's modulus Au | $E_{Au}$ | $57{\cdot}10^9$N/m$^2$ |
| Young's modulus Si | $E_{Si}$ | $170{\cdot}10^9$N/m$^2$ |
| Young's modulus $SiO_2$ | $E_{SiO_2}$ | $70{\cdot}10^9$N/m$^2$ |
| Young's modulus Pt | $E_{Pt}$ | $170{\cdot}10^9$N/m$^2$ |
| Young's modulus Ti | $E_{Ti}$ | $110{\cdot}10^9$N/m$^2$ |
| Young's modulus (Relaxed) Si | $E_R \approx E$ | N/m$^2$ |

# Appendix G

# Selected Articles and Proceedings

# Cantilever based mass sensor with hard contact readout

S. Dohn[a)]
*Department of Micro- and Nanotechnology, NanoDTU, Building 345E, DK-2800 Lyngby, Denmark*

O. Hansen
*Danish National Research Foundation's Center for Individual Nanoparticle Functionality (CINF), Department of Micro- and Nanotechnology, NanoDTU, Building 345E, DK-2800 Lyngby, Denmark*

A. Boisen
*Department of Micro- and Nanotechnology, NanoDTU, Building 345E, DK-2800 Lyngby, Denmark*

(Received 20 December 2005; accepted 12 May 2006; published online 29 June 2006)

We present a method for microcantilever resonant frequency detection. We measure the direct current from an intermittent contact once every vibration cycle between the conducting cantilever and a counterelectrode at a low bias voltage with respect to the cantilever, while the excitation frequency and amplitude are varied. The result is an almost "digital" detection of the resonant frequency. A relative frequency resolution $\Delta f/f$ of 1/80 000 with high signal to noise ratio in ambient conditions is demonstrated. The detection method can be applied to portable sensor systems with very high frequency nanoelectromechanical cantilevers using simple off-chip electronics. © *2006 American Institute of Physics*. [DOI: 10.1063/1.2217161]

Micro- and nanoelectromechanical systems (NEMS) have become important in sensing applications.[1] Cantilever based mass sensing, relying on a resonant frequency shift induced by the added mass,[2] has a potential for very high mass resolution as demonstrated by the reported detection of masses in the $10^{-18}$ g range.[3] The resonant frequency shift can be detected using optical[3] or electronic[4] detection methods. Most high-resolution systems, however, rely on optical detection.

A great challenge still at hand is to make portable sensor systems working in ambient conditions with such high sensitivity. This could probably be realized using optical detection; however, delicate alignment of the detection optics to the cantilever chip is required. Electronic detection relaxes the alignment requirements, but low signal levels and high sensitivity to stray and parasitic capacitance make integration of elaborate electronics and readout systems on the cantilever chip necessary.[5]

In this letter we show that it is possible to detect the resonant frequency of a cantilever based sensor by measuring the time average current flowing from an electrode to the cantilever during hard contact occurring once every cycle of the cantilever vibration. The electronic detection method provides very high resolution in ambient conditions using simple low-bandwidth off-chip electronics. Moreover, the detection method does not suffer from the common problem in electronic detection methods, where the strong actuation signals often contaminate the detected signal. Previous work on a similar design[6] did not focus on the sensor applications but rather on the ability to transfer single electrons by tunneling.

The resonant frequency of the cantilever is given by $f_0 \equiv \omega_0/(2\pi) = \sqrt{K/m^*}/(2\pi)$, where $K$ is the spring constant and $m^*$ is the effective vibrational mass of the cantilever. The cantilever mass responsivity is defined by $\mathcal{R} \equiv \partial\omega_0/\partial m = -\omega_0/2m^* \approx \delta\omega_0/\delta m$, where $\delta\omega_0$ is the resonant frequency shift caused by an added mass $\delta m$.[7] Thus a high resonant frequency $f_0$ and a low effective mass $m^*$ are required for a high-resolution mass sensing cantilever.

The mass resolution of the cantilever is affected by energy losses,[8] as the loss mechanisms add noise. The losses are accounted for by the quality factor $Q_d$ defined by the ratio of energy stored in the cantilever and energy lost per cycle. Several loss mechanisms, intrinsic and extrinsic, affect the quality factor of the cantilever,[9] but for microcantilevers operated in ambient conditions viscous damping from the surrounding medium is dominant resulting in quite low quality factors.

The minimum measurable change in resonant frequency, $\delta\omega_{0,\min}$, is determined by thermomechanical noise,[4] but in most applications the noise introduced by the measurement system, $\delta\omega_{0,\mathrm{sys}}$, is far larger. In order to reduce $\delta\omega_{0,\mathrm{sys}}$ to a minimum, it is important that the primary conversion of frequency to an electrical signal results in a large signal, then the unavoidable electronic noise becomes less important in comparison to the thermomechanical noise of the cantilever. The hard contact method we describe here is one such method, since a quite high dc level (~10 nA) is the primary electrical output signal, much higher current levels than seen in electron tunneling[6] detection schemes (~1 pA). A schematic of the detection setup used for hard contact readout is shown as overlay to the actual device in Fig. 1(a).

The cantilever was operated in dynamic mode by applying an actuation voltage, $V_A = V_{A,\mathrm{ac}} + V_{A,\mathrm{dc}}$, consisting of an ac (HP 33120A) and dc (Keithley 2400) voltage to the actuation electrode and grounding the cantilever. A small dc (HP E3611) voltage $V_E$ was applied to the electrode close to the apex of the cantilever through an integrating transconductance amplifier based on a Burr Brown OPA277P ($C = 1$ pF and $R = 22$ MΩ).

At sufficiently large vibrational amplitudes, the cantilever and electrode contact once every cycle, and a unidirectional current pulse train $I_{\mathrm{in}}(t)$, with a pulse width of $t_c$ and a magnitude of $I_{\mathrm{in}} = -V_E/R_C$, is supplied to the amplifier input [Fig. 1(a)]. Here $R_C$ is the total resistance of the contact. At steady state, the amplifier output voltage reaches a value of

[a)]Electronic mail: sd@mic.dtu.dk

 

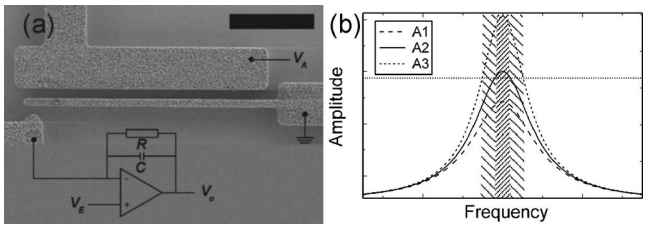


FIG. 1. The hard contact cantilever resonant frequency readout setup schematic is shown as an overlay on a SEM image of the cantilever (a). The scale bar is 20 $\mu$m long. The hard contact readout principle (b). Three amplitude functions with the same quality factor but different excitation energy levels are sketched. When the amplitude exceeds a critical value (dotted line) equal to the equilibrium cantilever to electrode distance $a_0$, a current will flow. This occurs in a wide frequency span at high cantilever excitation energy (A3 and sparsely hatched area) and in a narrower frequency span at lower excitation energy (A2 and densely hatched area).

$V_{o,\mathrm{ss}}=V_E-R\overline{I_{\mathrm{in}}}=V_E+(R/R_C)(t_c/T)V_E$, where $\overline{I_{\mathrm{in}}}$ is the time average of the input current and $T$ is the cycle time. $V_{o,\mathrm{ss}}$ was measured using a computer controlled Keithley 2000. It is apparent that the larger the amplitude, the larger the frequency span $\Delta f$ in which a current will flow [Fig. 1(b)]. The reciprocal relative frequency resolution $f_0/\Delta f$ thereby serves as a convenient measure of the quality of the measurement.

The cantilever used in the experiments was fabricated using standard microfabrication techniques. The cantilever was defined in a 2 $\mu$m thick silicon dioxide film thermally grown on a silicon substrate by etching in a STS advanced oxide etcher using aluminum as etch mask. The cantilever was subsequently released by underetching using a STS reactive ion etcher for isotropic silicon etching. Then platinum was deposited onto the sides and top of the structure using e-beam evaporation. A scanning electron microscope (SEM) image of the resulting cantilever is seen in Fig. 1(a). The cantilever is $L=60$ $\mu$m long, $W=1.8$ $\mu$m wide, and $H=1.5$ $\mu$m thick. The theoretical resonant frequency is 390 kHz with a mass responsivity of $\sim 1$ kHz/pg. The rough top surface [clearly seen in Fig. 3(a)] increases the surface area of the cantilever by roughly a factor of 10. This is desirable for gas detection.[10]

For mass loading of the cantilever $\sim 1$ $\mu$m diameter latex spheres[11] with an expected mass of $\Delta m=0.5$ pg were used. The latex-spheres were positioned on the cantilever using a manipulation setup based on a high-resolution optical Navitar microscope. A Newport *XYZ* stage was used for cantilever positioning, while an etched tungsten tip with a tip diameter of roughly 1 $\mu$m mounted on a Burleigh PCS-5400 piezomicromanipulator was used to manipulate the latex spheres.

In all measurements $V_{A,\mathrm{ac}}=10$ $V_{\mathrm{pp}}$ and $V_E=1$ V, while $V_{A,\mathrm{dc}}$ was varied to adjust the vibration amplitude. At a high level of the dc actuation voltage $V_{A,\mathrm{dc}}\simeq 22$ V, the resonant frequency was localized visually. $V_{o,\mathrm{ss}}$ was measured while the excitation frequency was scanned in discrete steps near and at the resonant frequency. This was repeated at decreasing levels of $V_{A,\mathrm{dc}}$, until the resonant peak disappeared in $V_{o,\mathrm{ss}}$. The results are shown in Fig. 2(a), which shows that the frequency span with a significant output signal, $\Delta V_{o,\mathrm{ss}}>0.1$ V, decreases with decreasing $V_{A,\mathrm{dc}}$, is minimized at $V_{A,\mathrm{dc}}=19.2$ V, and vanishes at $V_{A,\mathrm{dc}}=19.1$ V. From the measured voltages, the time averaged current is estimated to be in the order of $\overline{I_{\mathrm{in}}}\approx 10-50$ nA.

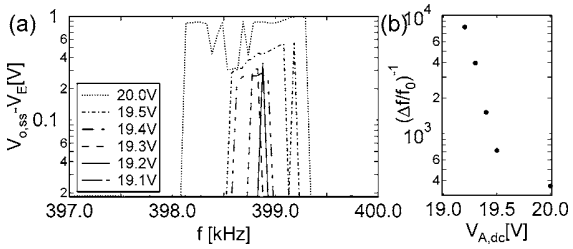


FIG. 2. The measured voltage $\Delta V_{o,\mathrm{ss}}$ as a function of frequency at different dc actuation voltages (a). The reciprocal relative frequency resolution $f_0/\Delta f$ in the measurements (b).

In Fig. 2(b) the reciprocal relative frequency resolution $f_0/\Delta f$ corresponding to the measurements in Fig. 2(a) is shown. From $V_{A,\mathrm{dc}}=20$ V to $V_{A,\mathrm{dc}}=19.2$ V, the reciprocal relative frequency resolution increases from $f_0/\Delta f=300$ to $f_0/\Delta f\simeq 8000$. Note that at $V_{A,\mathrm{dc}}=19.2$ V the resolution is limited by the resolution in applied frequencies.

A demonstration of the detection method used for mass sensing is shown in Fig. 3. Here two latex spheres were placed on the cantilever one after the other; the SEM image in Fig. 3(a) shows the apex of the cantilever with both latex spheres in place. The latex spheres were deformed by the manipulation but remained intact. The frequency responses with no, one, and two latex spheres are shown in Fig. 3(b). The change in resonant frequency for each added latex sphere was $\sim -1.1$ kHz, and the reciprocal relative frequency resolution was $20\,000<f_0/\Delta f\leqslant 80\,000$. The change in resonant frequency is more than twice as large as anticipated. The reason for the large frequency shift could be a lower effective mass density of the cantilever due to the very rough surface with rather deep holes etched into the cantilever material, but the latex spheres could also have a higher mass than expected due to absorbed water and salts from the atmosphere and the shipping liquid.

In all microelectromechanical system (MEMS) or NEMS systems where contact between surfaces is required or unavoidable, sticking is a serious concern. The nonstick condition for the detection method here is that the elastic energy stored in the cantilever with Young's modulus $Y$, deflected a distance $a_0$, exceeds the adhesive energy $A_C E_{\mathrm{adh}}$, due to a contact of area $A_C$. $E_{\mathrm{adh}}$ depends strongly on the mechanisms involved in the adhesion, but in worst case, where chemical bonds are formed, the order of magnitude is $E_{\mathrm{adh}}\sim 1$ J/m$^2$.[12] These considerations lead to the geometrical design rule $(W/L)^3\ Ha_0^2/A_C>8E_{\mathrm{adh}}/Y$ that must be fulfilled to unconditionally avoid sticking. Assuming a blunt wedge-like electrode and thereby a contact area of $A_C=H\ell$, the

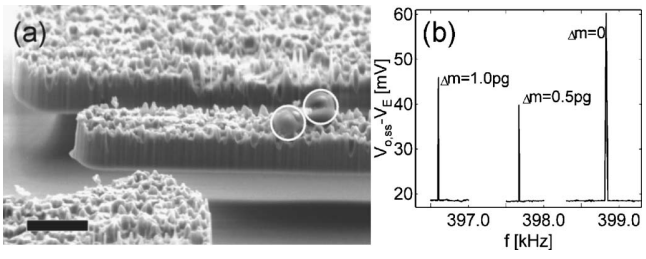


FIG. 3. SEM image of the cantilever apex with two latex spheres added (a). The frequency response with no, one, and two latex spheres on the cantilever (b). The two latex spheres are marked with white rings and are positioned $\sim 7$ $\mu$m from the apex. The scale bar is 2 $\mu$m long.

length $\ell$ of the contact region in the experimental devices presented here must fulfil $\ell < 1$ $\mu$m. This is in perfect agreement with observations, since sticking was never observed in these devices. For linear geometrically scaled devices, $\ell$ scales linearly, which should not pose problems, because the better lithographic tools required also improve the wedge sharpness.

The average current measured in this method depends on the ratio of contact time to cycle time and on the contact resistance. These parameters are thus important when considering the scaling behavior of the method. Assuming that $N$ coherent electron channels are formed in the contact, the contact resistance becomes $R_C = h/(2e^2N) \approx 13$ k$\Omega$/N,[13] where $h$ is Planck's constant and $e$ is the unit charge. Note that other resistance contributions, such as bulk and spreading resistances, are unimportant if low resistivity ($\sim 2$ $\mu\Omega$ cm) metals are used. The number of electron channels is probably affected by scaling, and in an ultimate scaled device a single channel is assumed to remain, which still results in a useful low resistance.

To a first approximation, the contact time is determined by the cantilever beam dynamics. During the contact time $t_c$, the cantilever motion is described by a superposition of modes for the cantilever pinned to the end deflection $a_0$. It follows that the contact time $t_c$ scales with geometry and material parameters exactly as the cycle time $T$ does; as a result the ratio of these is unaffected by geometrical scaling.

Compared to other electronic readout methods, the main advantage of the hard contact method is that a dc current is measured. Therefore simple low-bandwidth off-chip electronics can be used, and unavoidable parasitic and stray capacitances do not affect the frequency resolution; hence scaling to very high resonant frequency NEMS cantilevers is straightforward. Since delicate alignment of the cantilever chip to the detection system is not required, system integration is facilitated, especially for portable systems where the cantilever chip is a consumable; in such applications, this method may compete favorably with optical detection methods. A portable system based on the hard contact method combined with readout at higher bending modes[14] operated in ambient conditions could prove very sensitive and economical.

We have described a method for detection of the resonant frequency of microcantilevers based on measurement of a direct current from an intermittent hard contact to a biased electrode. The method was shown experimentally to provide high quality resonant frequency detection, since a relative frequency resolution of 1/80 000 was demonstrated in ambient conditions at a signal to noise ratio of several hundreds. We have shown that the method is scalable to high resonant frequency NEMS applications and provided a design rule to prevent sticking. Thus we are convinced that the method will prove useful in many cantilever based sensor systems, in particular, in portable systems, where it could prove to be a useful alternative to optical sensing as no critical alignment to the detection circuitry is needed with the method.

CINF is sponsored by The Danish National Research Foundation.

[1] M. Roukes, Phys. World **14**, 25 (2001).
[2] G. Y. Chen, T. Thundat, E. A. Wachter, and R. J. Warmack, J. Appl. Phys. **77**, 3618 (1995).
[3] T. Ono, X. X. Li, H. Miyashita, and M. Esashi, Rev. Sci. Instrum. **74**, 1240 (2003).
[4] K. L. Ekinci, X. M. H. Huang, and M. L. Roukes, Appl. Phys. Lett. **84**, 4469 (2004).
[5] E. Forsen, G. Abadal, S. Ghatnekar-Nilsson, J. Teva, J. Verd, R. Sandberg, W. Svendsen, F. Perez-Murano, J. Esteve, E. Figueras, F. Campabadal, L. Montelius, N. Barniol, and A. Boisen, Appl. Phys. Lett. **87**, 43507 (2005).
[6] A. Erbe, R. H. Blick, A. Tilke, A. Kriele, and J. P. Kotthaus, Appl. Phys. Lett. **73**, 3751 (1998).
[7] K. L. Ekinci, Y. T. Yang, and M. L. Roukes, J. Appl. Phys. **95**, 2682 (2004).
[8] G. Stemme, J. Micromech. Microeng. **1**, 113 (1991).
[9] K. Y. Yasumura, T. D. Stowe, E. M. Chow, T. Pfafman, T. W. Kenny, B. C. Stipe, and D. Rugar, J. Microelectromech. Syst. **9**, 117 (2000).
[10] A. G. Hansen, M. W. Mortensen, E. T. Andersen, J. Ulstrup, A. Kühle, J. Garnæs, and A. Boisen, Probe Microsc. **2**, 139 (2001).
[11] Kisker, pps-1.0 polystyrene micropartikel, 992 nm.
[12] W. P. Maszara, G. Goetz, A. Cavaglia, and J. B. McKetterick, J. Appl. Phys. **64**, 4943 (1988).
[13] S. Datta, *Electronic Transport In Mesoscopic Systems* (Cambridge University Press, Cambridge, 1995), p. 57.
[14] S. Dohn, R. Sandberg, W. Svendsen, and A. Boisen, Appl. Phys. Lett. **86**, 233501 (2005).

SENSOR LETTERS
Vol. 3, 1–4, 2005

# Direct Measurement of Resistance of Multiwalled Carbon Nanotubes Using Micro Four-Point Probes

Søren Dohn,* Kristian Mølhave, and Peter Bøggild

*MIC-Department of Micro and Nanotechnology, Technical University of Denmark, DK-2800 Kgs. Lyngby, Denmark*

(Received: 10 August 2005. Accepted: 14 September 2005)

The electrical properties of multiwalled carbon nanotubes was investigated by micro four point probes, fabricated using conventional silicon microfabrication techniques. After positioning of chemical vapour deposition-grown multi-walled carbon nanotubes on a $SiO_2$ substrate, the two- or four-point resistance at specific positions along the nanotubes, was measured by microprobes with different microelectrode spacings. Individual nanotubes were investigated in more detail by measuring current as a function of bias voltage until the point of failure and the results are compared to previously reported findings, using conventional measurement techniques.

**Keywords:** Four-Point Probe, Carbon Nanotube, Microelectrode, Resistance, Characterization.

## 1. INTRODUCTION

The electrical properties of multi-walled carbon nanotubes (MWNT) are of significant scientific interest and are relevant for many proposed and realized applications.[1–4] In practice, studies of the electrical properties generally require the pre-fabricated nanotubes to be interfaced to measurement equipment via microelectrodes. This can be done by dispersing nanotubes randomly on a surface and manipulating the nanotubes towards electrodes[5] or by locating the positions of the nanotubes for subsequent lithographic deposition of electrodes.[6] Other methods have been used, such as various scanning probe microscopy techniques[7–9] and using a nanowire as a shadow-mask when evaporating electrode material, thus leaving a MWNT bridging the narrow electrode gap under the nanowire.[10, 11]

From IV characteristics at high bias voltages, Avouris, and co-workers[12, 13] studied MWNT fabricated by arc-discharge, and discovered that individual carbon nanotube shells could be destroyed by passing a high current through the MWNT. Nakayama et al.[14] showed from TEM studies that current induced destruction of outer nanotube shells can be used to sharpen a MWNT. The authors observed an annealing-like behaviour, with the two-point resistance decreasing as the current limit was approached.

To rule out the possibility of chemicals in the lithography process affecting the electrical properties of carbon nanotubes, it is highly convenient to measure the resistance directly using a movable probe. A movable probe eliminates the need for lithography and manipulation of the sample, and allows for quick screening of the conductive properties of many nanostructures on the same sample, hence making the acquisition of statistical information easier. Previously, two-point resistance measurements have been performed using conducting AFM,[7] but this technique involves connecting one or two ends of the carbon nanotube to a fixed electrode and thus lithography and processing.

In this paper, we investigate the possibility of using a micro fabricated four-point probe for fast characterisation of CVD-grown MWNT by directly aligning the probes on top of the carbon nanotube using an optical or electron microscope. In this way time-consuming and potentially damaging deposition and processing of lithographic contacts are avoided. We compare our results to work reported in literature obtained by conventional techniques.

## 2. EXPERIMENTAL SETUP

Microchips with four microcantilevers extending over the chip edge were fabricated using conventional silicon micro fabrication.[15, 16] The microcantilevers are 1 $\mu$m thick, typically 1 to 8 $\mu$m wide, and 10–40 $\mu$m long. For multi-point electrical measurements, the silicon oxide cantilevers are covered with a Ti/Au metal layer giving a total serial resistance around 50 $\Omega$.

The experimental setup is based on an optical Navitar microscope, which allows viewing what appear to be

*Corresponding author; E-mail: sd@mic.dtu.dk

RESEARCH ARTICLE

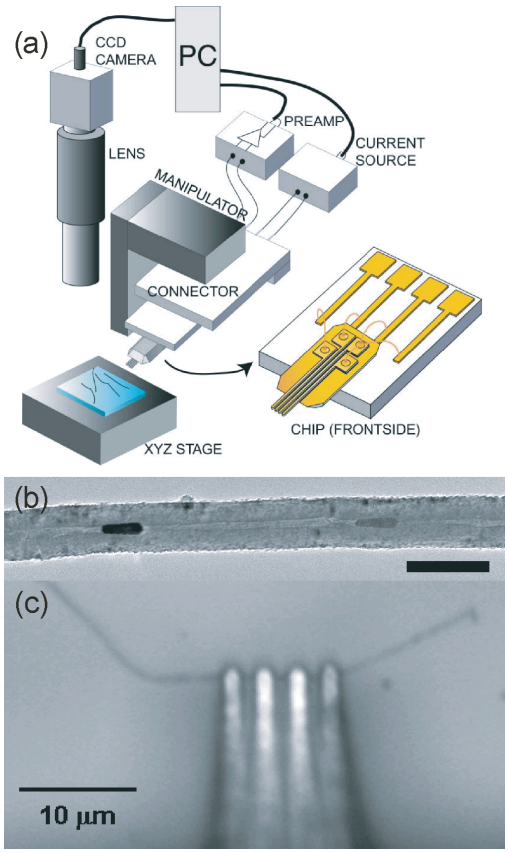


**Fig. 1.** (a) Schematic of the experimental setup. (b) A TEM image of a MWNT from the batch used in the experiments (upper part), and a micro four-point probe positioned on a MWNT that was first aligned using one of the microcantilevers (lower part). The scalebar is 100 nm. Inspection of the MWNT in a SEM after contact with the microprobe did not show any visible damage to the MWNT.

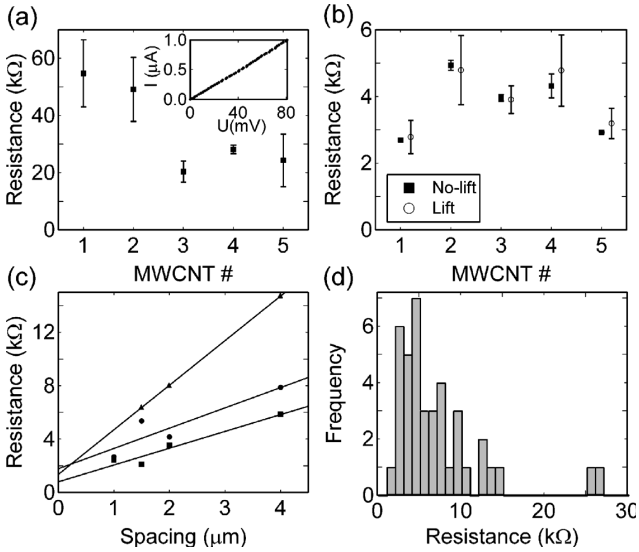


**Fig. 2.** (a) Average of 10 two-point measurements on five different MWNT with the probe remaining in contact between measurements. Each measurement is a linear fit to an IV-curve as shown in the inset. (b) Average of 10 four-point measurements on the same five MWNT with the probe remaining in contact between measurements and average of similar measurements where the probe was lifted between each measurement. (c) The resistance of three different MWNT as a function of centre electrode spacing in four-point measurements. (d) Histogram showing the distribution of four-point resistance of 39 MWNT.

individual MWNT with diameters down to roughly 20 nm when positioned on a reflecting surface. A Newport XYZ stage with 50 nm resolution is used for sample positioning, while the microcantilever probe is mounted on a Burleigh PCS-5400 piezo-micromanipulator with a precision better than 50 nm. The conductance was measured with a Keithley 2400 source-meter, and both the manipulation and the measurements were controlled by a PC running National Instruments Labview. A schematic of the setup is shown in Figure 1(a). For measurements in a LEO 1550 scanning electron microscope, we used a xyz-nanomanipulator from Klocke Nanotechnik to control the microcantilever probe. The investigated carbon nanotubes were grown by chemical vapour deposition[17] and they consist of 30–100 shells with considerable amounts of structural defects and catalytic particle residues as shown in the transmission electron microscope image of a typical MWNT in Figure 1(b).

## 3. RESULTS AND DISCUSSION

We examined the reproducibility of the cantilever probe resistance measurements. Figure 2(a) shows the two-point resistance of five MWNTs. Each data point is an average of 10 consecutive measurements with the microprobe fixed on the MWNT, recorded with time intervals of 1 s. The error bars show the standard deviation which is between $\pm 1.5$ and $\pm 12$ kΩ. In Figure 2(b), the measured four-point resistance for the same MWNTs is plotted both for 10 consecutive measurements and for measurements where the microprobe was lifted between each measurement. Lifting the probe between measurements increased the measurement error significantly from $\pm 0.1$ kΩ to 1 kΩ.

The resistance variations between the individual MWNTs appear to be larger than the errors, thus the microprobes seem to be capable of distinguishing differences in the intrinsic resistance properties of the individual MWNTs in the present sample. From TEM investigations of the MWNTs, the resistance is expected to vary because of differences in nanotube diameter and possibly remains of catalytic particles in the shell structures. By comparing the data in Figures 2(a) and 2(b), the relatively small uncertainty on the 4 point measurements indicates that the typical contact resistance is between 15 kΩ and 50 kΩ for these MWNTs and thereby is a considerable error source in the 2 point measurements. SEM investigations of MWNTs after 4 point measurements showed no sign of damage or deformation.

The importance of the electrode-spacing in the four-point measurements was investigated on three MWNTs. The result can be seen in Figure 2(c), where the resistance for centre electrode-spacing of 1, 1.5, 2, and 4 $\mu$m are

RESEARCH ARTICLE

shown. The MWNT resistivity obtained from linear fits to the data is in the range 1.3–3.3 kΩ/μm. The fitted lines do however not pass through the origin, but give zero-spacing resistances in the range 0.8–1.4 kΩ.

The fairly linear dependence of resistance with microelectrode pitch indicates that the conductance of the MWNTs is diffusive as expected from the TEM investigations, and the findings are thereby in qualitative agreement with previous reported results.[8] The non-zero resistance found at an electrode spacing of zero indicates that the exact position of the contact point between an individual microelectrode and nanotube can vary and is not necessarily at the edge of the electrode as assumed when plotting the results as function of electrode spacing.

Using a microprobe with a pitch of 3 μm we measured the four-point resistance of 39 MWNTs in ambient conditions with a relatively low bias voltage corresponding to a current in the 1–10 μA range. The average four-point resistance was found to be 4.7 kΩ. The behaviour at a higher bias voltage was investigated on 48 MWNTs by slowly increasing the bias voltage in a two-point measurement until the measured current decreased within a few measurement points, interpreting this as a sign of damage to the shell structure. When the drop in current was observed, the bias voltage was set to zero. For each nanotube we repeated this procedure until no current could be passed through the MWNT, indicating total failure of the carbon nanotube.

Figure 3 shows optical and SEM images of MWNT before and after breakdown of all shells. When IV measurements were performed in a SEM, the MWNT in all studied cases burned in the region between the cantilevers, preferably in the middle or at a kink of the MWNT. In the similar experiments in ambient conditions, it was difficult to determine exactly where the MWNT burned relative to the position of the microcantilevers.

While 44 of the MWNTs burned within a few consecutive voltage sweeps, four MWNTs showed stepwise decrease in current in six or more steps. In Figure 4(a), 11 IV-measurements of a single MWNT are shown with the first IV curve plotted as a thick line. The shape of the curves from measurement 2–11 are very similar with the current increasing with voltage until a saturation point is reached ($dI/dV = 0$), after which a rapid increase in resistance is observed. The shape of the first curve is remarkably different from the following curves, with a higher low-bias resistance and sudden decrease around 1.5 V. The saturation point is reached at a voltage of 2.2 V with a maximum current of 911 μA. In the inset the low bias conductance is plotted as a function of the number of shell burn events, and the four MWNTs are seen to be divided in two groups, i.e., two MWNTs (top) showing a linear and two MWNTs (bottom) showing a nonlinear behaviour.

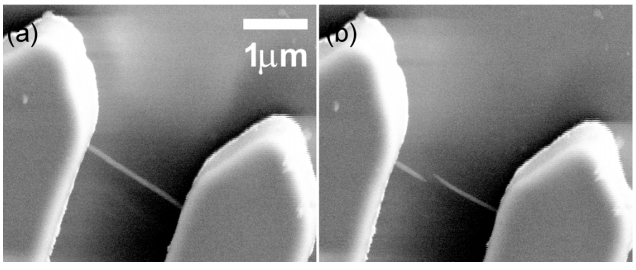


**Fig. 3.** (a) Two microcantilever electrodes in contact with a MWNT inside a scanning electron microscope. (b) After applying a high bias the nanotube is broken in the middle.

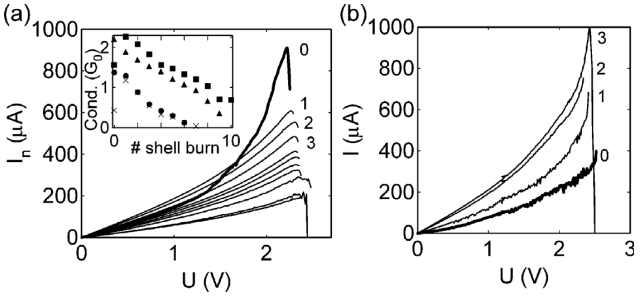


**Fig. 4.** (a) IV-characteristics of a MWNT. The first measurement is drawn with a heavy line, while the thin line show ten measurements made with the same conditions. The shape of the curves from measurement 2–11 is very similar, with the current increasing with voltage until a saturation point is reached ($dI/dV = 0$), after which a rapid increase in resistance is observed, at which point the voltage is set to zero. The shape of the first curve is remarkably different from the following curves, i.e., higher low-bias resistance and lower minimum resistance. The inset shows the development of the low bias conductance by consecutive IV curves for four different MWNT. (b) A series of curves on a different sample, where the voltage sweep was each time aborted before the saturation regime was reached. Eventually, at (3), the MWNT was destroyed.

We examined the deviating IV-characteristics of a MWNT by aborting the measurements before the saturation point was reached, i.e., before the outer shell(s) were removed, as shown in Figure 4(b). Subsequent IV-curves exhibit decreasing resistance, appearing to converge to the level of the third curve.

The IV-curves shown in Figure 4(a) are very similar to those observed in Refs. [12, 13] where however no difference in behavior of the first and successive shells was observed. We observed the annealing-like behavior in several samples. A similar effect was reported by Ref. [14] and Ref. [18]. The exact number of shells destroyed in each measurement series are not clear from the measurements; in several experiments we observed the MWNT to fail after just a few destructive events. This could be caused by a large number of shells being removed at the same time. Shell removal experiments performed in a Transmission Electron Microscope are currently under preparation and will hopefully clarify this point.

## 4. CONCLUSION

We have demonstrated that micro four-point probes can be used as a characterisation tool for quickly measuring

the resistance and IV curves of MWNT with a reasonable reproducibility. The studied MWNT did not appear to be permanently deformed by such measurements and the contact resistances were in the range 1–50 kΩ when stable contact was achieved, and hence comparable to contact resistance achieved by contacts defined by electron beam lithography. With this method we can freely select a position for contacting a nanostructure without the need to pattern electrodes lithographically to the nanostructure. With improved mechanical stability and vibration control a scanning four-point measurement may be viable, which would be a useful tool in studying the intrinsic properties of carbon nanotubes and other nanoscale one-dimensional structures.

**Acknowledgments:** We acknowledge discussions with Dorte Nørgaard Madsen and Jakob Kjelstrup Hansen, and contributions from Daniel Kjær and Tabasam Ali. Nanotubes were supplied by Richard Czerw and Ramona Mateiu. The project was supported by the STVF talentproject grant: "Nanohand."

## References and Notes

1. R. Martel, T. Schmidt, H. R. Shea, T. Hertel, and P. Avouris, *Appl. Phys. Lett.* 73, 2447 **(1998)**.
2. J. K. Abraham, B. Philip, A. Witchurch, V. K. Varadan, and C. C. Reddy, *Smart Mater. Struct.* 13, 1045 **(2004)**.
3. N. Koratkar, A. Modi, E. Lass, and P. Ajayan, *J. Nanosci. Nanotechnol.* 4, 744 **(2004)**.
4. R. Mateiu, Z. J. Davis, D. N. Madsen, K. Molhave, P. Boggild, A. M. Rassmusen, M. Brorson, C. J. H. Jacobsen, and A. Boisen, *Microelectron. Eng.* 73–74, 670 **(2004)**.
5. P. Avouris, *Acc. Chem. Res.* 35, 1026 **(2002)**.
6. W. Fritzsche, J. M. Kohler, K. J. Bohm, E. Unger, T. Wagner, R. Kirsch, M. Mertig, and W. Pompe, *Nanotechnology* 10, 331 **(1999)**.
7. M. Freitag, M. Radosavljevic, W. Clauss, and A. T. Johnson, *Phys. Rev. B* 62, R2307 **(2000)**.
8. A. Bachtold, M. S. Fuhrer, S. Plyasunov, M. Forero, E. H. Anderson, A. Zettl, and P. L. Mceuen, *Phys. Rev. Lett.* 84, 6082 **(2000)**.
9. Y. Yaish, J. Y. Park, S. Rosenblatt, V. Sazonova, M. Brink, and P. L. Mceuen, *Phys. Rev. Lett.* 92, **(2004)**.
10. P. J. de Pablo, E. Graugnard, B. Walsh, R. P. Andres, S. Datta, and R. Reifenberger, *Appl. Phys. Lett.* 74, 323 **(1999)**.
11. S. Dohn, J. Kjelstrup-Hansen, D. N. Madsen, K. Mølhave, and P. Bøggild, *Ultramicroscopy* **(2005)**, In press.
12. P. C. Collins, M. S. Arnold, and P. Avouris, *Science* 292, 706 **(2001)**.
13. P. G. Collins and P. Avouris, *Appl. Phys. A-Mater. Sci. Proc.* 74, 329 **(2002)**.
14. Y. Nakayama and S. Akita, *New J. Phys.* 5, **(2003)**.
15. C. L. Petersen, T. M. Hansen, P. Boggild, A. Boisen, O. Hansen, T. Hassenkam, and F. Grey, *Sensors and Actuators a-Physical* 96, 53 **(2002)**.
16. P. Boggild, T. M. Hansen, C. Tanasa, and F. Grey, *Nanotechnology* 12, 331 **(2001)**.
17. The MWCNT was supplied by Richard Czerw at Wake University.
18. P. G. Collins, M. Hersam, M. Arnold, R. Martel, and P. Avouris, *Phys. Rev. Lett.* 86, 3128 **(2001)**.

# Enhanced functionality of cantilever based mass sensors using higher modes

Søren Dohn,[a] Rasmus Sandberg, Winnie Svendsen, and Anja Boisen
*Department of Micro and Nanotechnology, Technical University of Denmark, DK-2800 Lyngby, Denmark*

(Received 19 November 2004; accepted 10 June 2005; published online 3 June 2005)

By positioning a single gold particle at different locations along the length axis on a cantilever based mass sensor, we have investigated the effect of mass position on the mass responsivity and compared the results to simulations. A significant improvement in quality factor and responsivity was achieved by operating the cantilever in the fourth bending mode thereby increasing the intrinsic sensitivity. It is shown that the use of higher bending modes grants a spatial resolution and thereby enhances the functionality of the cantilever based mass sensor. © *2005 American Institute of Physics*. [DOI: 10.1063/1.1948521]

The demand for sensors with high sensitivity, improved functionality, and reduced analyte usage as well as the demand for portable devices is driving the development of sensors from the micro- to the nanoregime. Cantilever based sensors have been a part of this development since the method was proposed by Chen *et al.*[1] in 1995. Today cantilevers are used widely in sensor applications in the static mode where a reaction on the surface creates surface stress which in turn causes a bending of the cantilever.[2,3] Also, the use of vibrating cantilevers shows great promises for sensor applications and recently systems capable of detecting masses in the $10^{-18}$ g range have been reported.[4,5] Here we report on the investigation of cantilever sensitivity using a movable point-mass, and experimental results are compared with simulations.

The resonant frequencies for a cantilever is given by

$$f_n = \omega_n/2\pi = (2\pi)^{-1}\sqrt{k/m_n^*}, \tag{1}$$

where $m_n^*$ is the effective mass of the $n$th mode of vibration. The higher the mode of vibration the smaller the effective mass due to the increasing number of nodal points. Schematics of the first four bending modes are shown in Fig. 1. It is seen that certain regions of the cantilever do not take part in the vibration and the positions of these are changing with the mode of vibration. The resonant frequency change caused by added mass therefore depends on the mass position. This has previously been investigated theoretically on the macroscopic scale.[6–8] The sensitivity of cantilever based mass sensors has been investigated by several groups[9,10] and the terminology used here is adopted from the work of Ekinci *et al.*[10] The mass responsivity is $\mathcal{R} \approx 2\pi\Delta f/\Delta m$, and the intrinsic sensitivity is $\delta m_n \propto \mathcal{R}^{-1}\sqrt{1/\omega_n Q_n}$ (assuming the energy in the cantilever is constant).

As an alternative to use the entire cantilever surface for molecular adsorption we propose to use only certain areas of the cantilever and positioning these for optimum sensitivity. We investigate the concept by adding a point-mass to a microcantilever. By moving this point-mass in small steps along the length direction of the cantilever, and simultaneously determining the resonant frequency for several bending modes, we can locate the positions yielding high mass responsivity. The experimental data are compared to simulations performed using finite element software.

The experimental setup (Fig. 2) consists of a HeNe laser, which is focused on a micrometer sized cantilever. The cantilever chip is clamped on top of a piezoactuator which is driven by a HP4194A gain/phase analyzer and placed in a custom built vacuum chamber capable of maintaining a vacuum of 0.5 mbar at which all experiments are performed. The position of the reflected beam is registered by a photodiode, and the signal is after amplification measured using the HP4194A gain/phase analyzer. By actuating the cantilever using a piezoactuator driven by the gain/phase analyzer the amplitude and phase of the resonating cantilever can be detected. Data from the gain/phase analyzer are transferred through a general purpose interface bus interface to a personal computer.

The cantilever used in the experiment is fabricated in $SiO_2$ and subsequently coated on the topside with 10 nm Ti and 100 nm Au (the fabrication process is described in Ref. 11). The cantilever dimensions are measured in a scanning electron microscope (SEM) yielding a length, width, and thickness of approximately 153, 11, and 1.05 $\mu$m, respectively. A rather large cantilever with a large surface area was chosen because it facilitates easy manipulation of particles on the cantilever surface and it gives high resolution in the length direction. The metal coating was used to

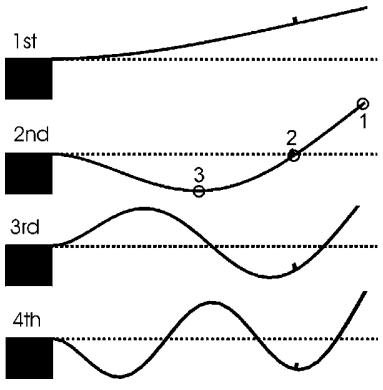


FIG. 1. Schematics of the first four bending modes of a cantilever seen from the side. Due to the nodal points certain parts of the cantilever do not take part of the vibration, and the particle depicted approximately 3/4 from the base of the cantilever is in theory not detectable in the second mode.

[a]Electronic mail: sd@mic.dtu.dk

 

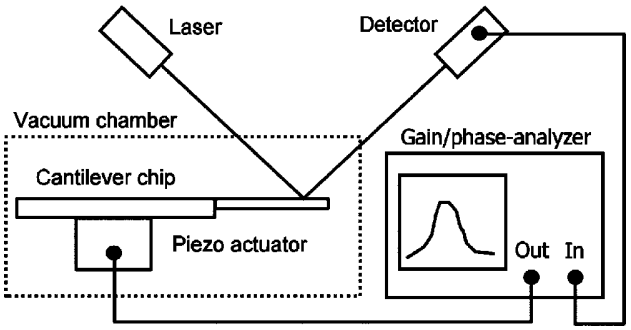


FIG. 2. Schematic of the setup used in the experiments. The micro cantilever chip is clamped on a piezo actuator driven by a gain/phase analyzer. Both cantilever and piezoactuator are placed in a vacuum chamber. A laser is focused on the cantilever and the position of the reflected beam is detected by a photodiode, and the signal is feed into the gain/phase analyzer.

improve the reflectivity of the $SiO_2$ cantilevers.

A single gold bead with a radius of 0.9 $\mu$m, corresponding to a mass of approximately 60 pg, is positioned on the cantilever [Fig. 3(a)] using a manipulation setup based on a high resolution optical Navitar microscope: A Newport *XYZ* stage is used for cantilever positioning, while an etched tungsten tip with a tip diameter of roughly 1 $\mu$m mounted on a Burleigh PCS-5400 piezomicromanipulator is used for manipulating the gold bead. The position of the gold bead is determined from optical images with an estimated accuracy of $\pm 1\mu$m. After positioning of the gold bead the resonant frequency of the cantilever is measured, and the bead is pushed with the tungsten tip to a new location where the resonant frequency is measured again.

The cantilever structure on which simulations are performed using the finite element software, CowentorWare, is shown in Fig. 3(b). The simulated cantilever has the same dimensions as the cantilever used in the experiment and is also metal coated.[12] The mesh generated for the calculations consists of bricks which are 1 $\mu$m in the length direction of the cantilever. The gold bead is simulated as a gold box with sidewalls of 1.8 $\mu$m in length, and this causes two problems. The mass of the box is too big, and since the contact area between a surface and box is much larger than between a surface and a sphere, a stiffening of the cantilever will occur. Therefore the density of the box is reduced[12] so the weight matches that of the gold bead. Also Young's modulus of the box was reduced to a 100th of that of gold, since no stiffening was observed at this value.

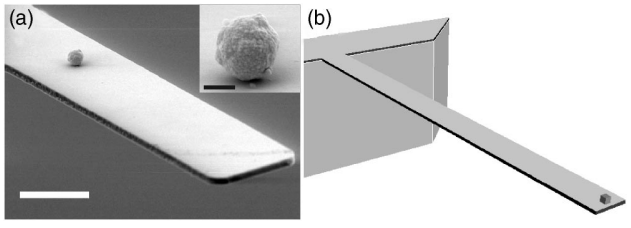


FIG. 3. (a) SEM image showing part of the micro cantilever with a gold bead positioned close to the apex. The scale bar is 5 $\mu$m. The inset shows a close-up of the gold particle (scale bar 500 nm). (b) Simulated structure used for calculation of the theoretical shift in resonance as a function of mass position. The simulated cantilever has the same dimensions as the cantilever used in the experiment, and the mesh generated for the calculations consists of bricks which are 1 $\mu$m in the length direction of the cantilever.

TABLE I. The resonant frequency measured and simulated for the first four bending modes of the cantilever together with the experimentally observed maximum change in frequency and relative sensitivity for the specific mode.

| Mode | 1 | 2 | 3 | 4 |
|---|---|---|---|---|
| $f_{exp}$ (Hz) | 30 712 | 192 493 | 539 060 | 1 056 640 |
| $f_{sim}$(Hz) | 31 734 | 198 815 | 556 486 | 1 089 920 |
| $\Delta f_{max}$(Hz) | 480 | 2541 | 6059 | 9864 |
| $\delta m_1/\delta m_n$ | 1 | 23 | 102 | 276 |

The resonant frequency ($f_{exp}$) of the first four bending modes of the microcantilever is measured before the gold bead is positioned on the cantilever. The results are shown in Table I together with the simulated resonant frequencies ($f_{sim}$). The simulated resonant frequencies are within 3.5% of the experimental values for all the measured bending modes.

When adding the single gold bead to the tip of the cantilever the resonant frequency of all four modes decrease as expected from Eq. (1). Typical examples of the recorded amplitude resonance peaks are depicted in Fig. 4. These particular resonant peaks are taken from the second bending mode, and the numbering of the peaks refers to the position of the gold bead on the cantilever (Fig. 1). The fitted peaks of the first four bending modes all have an average standard deviation of less than 0.01%, and the standard deviation of successive experiments with no movement of the bead is within this limit. From measurements at all positions an average *Q* factor was calculated for each mode (Fig. 4). The *Q* factor increases almost a factor of 3 going from the first to the second bending mode and the fourth mode has a *Q* factor that is more than five times larger than the first mode. There is no significant difference between the *Q* factor of the loaded and unloaded cantilever.

The change in resonance frequency for the first four bending modes of the cantilever as a function of particle position along the length axis has been recorded. The experimentally observed relative change in resonance is compared to the values obtained by simulations and excellent agreement is obtained for all bending modes (Fig. 5). For all modes the highest change in frequency ($\Delta f_{max}$) is obtained when the gold bead is positioned at the tip of the cantilever (experimental values listed in Table I). The absolute change in frequency and thereby the responsivity increases with the mode number giving a mass responsivity of $\sim$5 fg/Hz in the fourth mode for the added mass of 60 pg. The relative sensitivities $\delta m_1/\delta m_n$ have been calculated (Table I), and the sensitivity is seen to increase by a factor of $\sim$300 using the fourth mode.

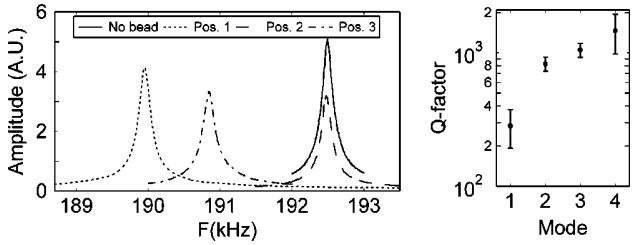


FIG. 4. Resonant peaks for the second bending mode as function of position and the average *Q* factor for the recorded bending modes. The positions are indicated in Fig. 1. Only part of the recorded second bending mode peaks are shown for clarity.

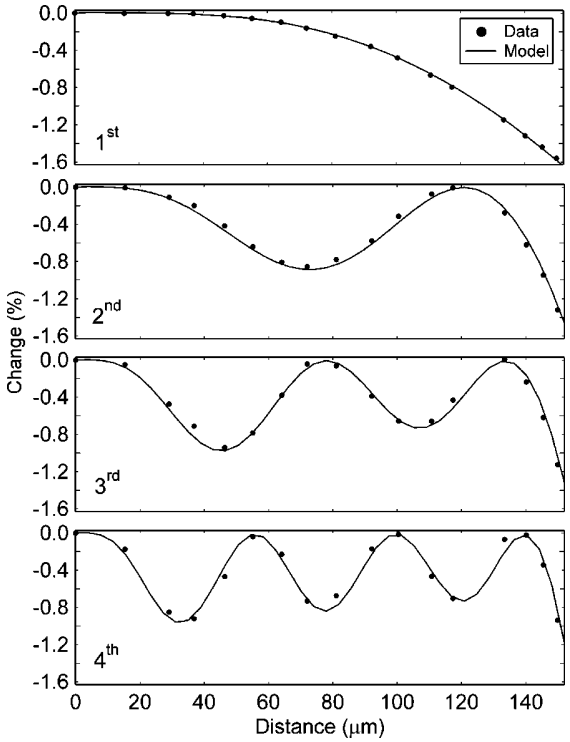


FIG. 5. Measured shift in resonance as a function of position compared to the simulated values shown for the first four bending modes of vibration.

The highest measured resonance mode results in the best mass responsivity of the cantilever and corresponds to our theoretical predictions. The large increase in sensitivity with increasing bending modes is mainly owed to a decrease in the effective mass [Eq. (1)], but also to the increase in $Q$ factor. The rather low $Q$ factor observed for the cantilevers are due to the metal coating,[13] and similar uncoated cantilevers have $Q$ factors that are 10 times higher. The increasing $Q$ factor has previously been observed[14,15] and is likely due to the smaller centre of mass movement and smaller radiation at the support for increasing bending modes.[16]

In conclusion, a mass responsivity of approximately 5 fg/Hz has been observed for a micrometer sized cantilever when operating the cantilever in the fourth mode. The increase in $Q$ factor and resonant frequency as well as the decrease in effective mass makes the intrinsic sensitivity of the cantilever significantly better for increasing mode numbers ($\sim$300 for the fourth mode). This implies that a 300 times smaller mass can be detected in the fourth mode compared to the first, assuming the cantilever is the dominant source of noise. To fully utilize the capabilities of a cantilever based mass sensor it is therefore important to operate it at higher modes.

The experimentally observed changes in resonant frequency when adding a point mass show excellent agreement with the simulations for the first four bending modes. From the measurements it follows that a single cantilever operated in the fourth mode has four positions for high sensitivity mass sensing. The number of sensitive positions can be further increased by operating at even higher modes.

The method presented can be used for enhancing the performance compared to conventional cantilever based mass sensors since the $Q$ factor degrading gold coating of the entire cantilever can be avoided. Using higher bending modes for detection it is possible to achieve a significant increase in the intrinsic sensitivity compared to the fundamental bending mode and moreover the method in principle grants a spatial resolution to the cantilever based mass sensor. By measuring different modes of vibration it should be possible to locate the position of the added mass on the cantilever. One possible application could be to detect more than one specific molecule using a single cantilever, by position several particles or coated areas functionalized for recognition of different molecules individually on the cantilever.

[1] G. Y. Chen, T. Thundat, E. A. Wachter, and R. J. Warmack, J. Appl. Phys. **77**, 3618 (1995).
[2] J. Fritz, M. K. Baller, H. P. Lang, H. Rothuizen, P. Vettiger, E. Meyer, H. J. Guntherodt, C. Gerber, and J. K. Gimzewski, Science **288**, 316 (2000).
[3] P. A. Rasmussen, J. Thaysen, O. Hansen, S. C. Eriksen, and A. Boisen, Ultramicroscopy **97**, 371 (2003).
[4] T. Ono, X. X. Li, H. Miyashita, and M. Esashi, Rev. Sci. Instrum. **74**, 1240 (2003).
[5] K. L. Ekinci, X. M. H. Huang, and M. L. Roukes, Appl. Phys. Lett. **84**, 4469 (2004).
[6] S. Park, W. K. Chung, Y. Youm, and J. W. Lee, J. Sound Vib. **230**, 591 (2000).
[7] M. Chiba and T. Sugimoto, J. Sound Vib. **260**, 237 (2003).
[8] K. H. Low, J. Sound Vib. **215**, 381 (1998).
[9] P. I. Oden, Sens. Actuators B **53**, 191 (1998).
[10] K. L. Ekinci, Y. T. Yang, and M. L. Roukes, J. Appl. Phys. **95**, 2682 (2004).
[11] C. L. Petersen, T. M. Hansen, P. Boggild, A. Boisen, O. Hansen, T. Hassenkam, and F. Grey, Sens. Actuators, A **96**, 53 (2002).
[12] The density ($\rho$) and Young's ($E$) modulus for the simulated materials are $\rho=2150$ kg/m$^3$ and $E=70$ GPa($SiO_2$), $\rho=4500$ kg/m$^3$ and $E=110$ GPa (Ti) and $\rho=19300$ kg/m$^3$ and $E=57$ GPa (Au). The density of the box is set to $\rho=10106$ kg/m$^3$ with $E=0.57$ GPa.
[13] R. H. Blick, A. Erbe, L. Pescini, A. Kraus, D. V. Scheible, F. W. Beil, E. Hoehberger, A. Hoerner, J. Kirschbaum, and H. Lorenz, J. Phys.: Condens. Matter **14**, R905 (2002).
[14] L. B. Sharos, A. Raman, S. Crittenden, and R. Reifenberger, Appl. Phys. Lett. **84**, 4638 (2004).
[15] J. L. Yang, T. Ono, and M. Esashi, Sens. Actuators, A **82**, 102 (2000).
[16] G. Stemme, J. Micromech. Microeng. **1**, 113 (1991).

Available online at www.sciencedirect.com
SCIENCE DIRECT®
ELSEVIER
Ultramicroscopy 105 (2005) 209–214
ultramicroscopy
www.elsevier.com/locate/ultramic

# Multi-walled carbon nanotubes integrated in microcantilevers for application of tensile strain

S. Dohn*, J. Kjelstrup-Hansen, D.N. Madsen, K. Mølhave, P. Bøggild

*MIC – Department of Micro- and Nanotechnology, DTU Building 345 East Technical University of Denmark, DK-2800 Kgs. Lyngby, Denmark*

Received 21 May 2004; received in revised form 20 December 2004

**Abstract**

Individual multi-walled carbon nanotubes were positioned on silicon oxide microcantilevers using nanomanipulation tools. A silicon nanowire with a diameter of 200 nm is positioned across the nanotube, and serves as shadow mask during deposition of conducting electrode material, leading to a 200 nm gap in the cantilever electrode only connected by the nanotube. By deflecting the cantilever, tensile strain of the nanotube up to 0.6% can be applied, with negligible transverse deformation or bending. Measurements of the conductance as a function of strain on different samples showed large variations in the response. Using a simple resistor model we estimate the expected conductance-strain response for a multi-walled carbon nanotube, and compare to our results on multi-walled carbon nanotubes as well as measurements by others on single-walled carbon nanotubes. Integration of nanotubes or nanowires with microcantilevers could lead to highly compact force feedback sensors for characterization and manipulation of nanostructures.


*PACS:* 07.07.Df; 81.05.Tp

*Keywords:* Cantilever; Sensor; Nanotube

## 1. Introduction

The possibility of using structures such as carbon nanotubes and nanowires [1] as readymade mechanical or electrical components in microfabricated devices, has led to the construction of field-effect transistors [2–4] quantum dots [5], gas- and biosensors [6,7], field-emitters [8] and logic circuitry [9]. Recently, the electromechanical properties of carbon nanotubes have attracted much attention. Stretching of a single-walled carbon nanotube (SWCNT) is expected to cause conductance changes through changes in the energy bandgap [10–12]. By pressing the tip of an atomic force

*Corresponding author. Tel.: +45 4525 5733; fax: +45 4588 7762.
*E-mail address:* sd@mic.dtu.dk (S. Dohn).

0304-3991/$ - see front matter © 2005 Elsevier B.V. All rights reserved.
doi:10.1016/j.ultramic.2005.06.038

microscope (AFM) on a suspended SWCNT, Tombler et al. [13] measured an increase in resistance of about two orders of magnitude for a strain $\varepsilon$ of 3%, which translates into a gauge factor, $g = \Delta R/\varepsilon R$, of order $10^3$. These variations were mainly attributed to transverse deformations induced by the AFM tip such as bending and collapse of the tube.

However, calculations considering both the effect of transverse deformations and stretching on conductance performed by Maiti et al. [14] indicated that the main cause of change in conductance was tensile stretching rather than transverse deformation, and that the conductance response to tensile strain is highly dependent on bandstructure; while armchair nanotubes are hardly affected, zig-zag nanotubes undergo conductance changes comparable to the semiconductor piezoresistors. A second set of experiment by Cao and co-workers [11] using a different geometry with more uniform tensile deformation, showed distinct differences in response that were related to the bandstructure of the nanotubes, and also found that the responses were generally larger than what should be expected from purely stretch-induced changes in bandgap. The authors could not rule out the possibility of transverse deformations, due to the method of stretching.

At this point, no measurements of the strain sensitivity of multi-walled carbon nanotubes (MWCNT) resistance have been performed. MWCNT are much easier to manipulate than SWCNT, and it is also an interesting question in which way the shell structure with several shells contributing with different levels of strain sensitivities, will affect the total response.

In this work we studied the response of MWCNT fixed mechanically and electrically on a microcantilever using a nanowire as a shadow mask in a metallization step, in order to create a narrow gap in the electrode layer on the cantilever, and thereby forming source and drain contacts to the MWCNT. A similar method was used to electrically contact carbon nanotubes by Pablo et al. [15], however, using a 4.3-μm-diameter tungsten wire across a carbon nanotube resting on a planar substrate. Deflecting the cantilever creates a nearly pure tensile strain in the nanotube with negligible transverse deformation. We have investigated a few devices made with this technique and observe large variations in the response, which we compare to a simple model treating the individual shells as resistors in a network. The method opens for the possibility of using a MWCNT or other type of strain-sensitive wire or tube as a strain gauge on a microcantilever, which could lead to very compact force-feedback probes.

## 2. Experimental setup

Microchips equipped with two or four microcantilevers were fabricated using conventional silicon microfabrication techniques [16,17]. The microcantilevers are 1-μm-thick and 4–8-μm-wide silicon oxide cantilevers, which can be covered with a thin metallic coating that allows the cantilevers to be used for multi-point electrical measurements [16].

The MWCNTs investigated were grown by chemical vapor deposition at Clemson University with diameters up to 100 nm. The silicon nanowires used as shadow masks were single-crystalline, 10–100-μm-long, 200–300-nm-wide wires fabricated by a deep etching technique at Phillips research laboratories [18].

The experimental setup is based on an optical Navitar objective lens, which in combination with a CCD camera allows for viewing MWCNT or bundles of nanotubes with diameters down to 20–30 nm when these are placed on a reflecting surface. A Newport XYZ stage with 50 nm resolution is used for sample positioning, while one or two microcantilever tools are mounted on independent Burleigh PCS-300 piezo-manipulators with 300 μm travel range and roughly 50 nm precision. Conductance measurements were performed using a Keithley 2400 combined current source and voltmeter. Fig. 1a illustrates the procedure for assembly of a MWCNT strain gauge. The procedure includes the following steps: (i) a single MWCNT is isolated from the sample using an etched tungsten tip as manipulation tool. (ii) The nanotube is placed on a 3–8-μm-wide microcantilever. By manipulating the nanotube on the surface of the target cantilever using the

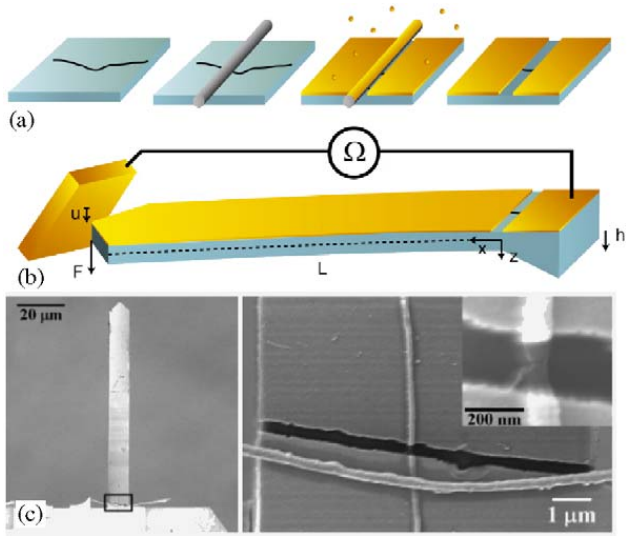


Fig. 1. (a) Procedure for assembly of a MWCNT strain gauge: a nanotube is positioned near the fixed end of a microcantilever and oriented along the length axis. A silicon nanowire is positioned across the nanotube. A 60–90 nm Ti/Au layer is deposited on the cantilever, embedding the nanotube. Finally, the silicon nanowire is removed, thus exposing about 200 nm of MWCNT in the electrode gap. (b) Sketch of the setup for electromechanical measurements. The resistance as a function of strain can be measured by deflecting the cantilever, and calculating the resulting strain from continuum mechanics. The length L, thickness h and deflection u of the cantilever are denoted for a force F applied to the tip, by a conducting substrate. The dashed line marks the neutral axis. (c) SEM image of an 8-μm-wide microcantilever, with a silicon nanowire positioned across. The image to the right shows an enlarged portion of the image. The nanowire has been released, and the electrode gap appears as a dark line. In the inset, a MWCNT with a diameter of 60 nm is visible in the electrode gap.

tungsten tip, the nanotube is aligned with the target cantilever. (iii) The first three steps are now repeated with a silicon nanowire. The nanowire is however positioned perpendicular to the carbon nanotube to span across the target cantilever and is placed as close to the support of the cantilever as possible. (iv) The structure is covered by 10–40 nm Ti and 50 nm Au using an electron beam evaporation system. (v) By removing the silicon nanowire, a non-metallized 200-nm-long section of the MWCNT is exposed, in the following referred to as the electrode gap. By pressing the cantilever against a gold surface, the nanotube can be strained reversibly, while the conductance is measured, as depicted in Fig. 1b. Measurements were performed on seven MWCNT devices, of which three showed a clear dependence on strain, while the rest showed no detectable strain-dependence. One of the fabricated devices is shown in Fig. 1c.

## 3. Results and discussion

The strain $\varepsilon$ induced by an end-point deflection $u(L) = u_L$ of a cantilever with length $L$, width $w$ and thickness $h$, is related to the internal bending moment $M = F(L - x)$ by $\varepsilon = -yM/EI$, where $E$ is the Young's modulus of the cantilever and $I$ the moment of inertia [19]. The distance from the neutral axis is $y = h/2$ at the surface for a homogeneous cantilever. When compensating for the thin metallic electrode layer, $y$ is shifted by 15%. Hence, the strain is given by $\varepsilon = F(L - x)y/EI$. Since the length of the electrode gap is very short compared to the cantilever, we take $L - x \approx L$ at the electrode gap. Using Hooke's law $F = u_L \cdot 3EI/L^3$ for a simple uniform cantilever with an applied end-point force $F$ [19], we obtain the strain of the nanotube as a function of deflection, $\varepsilon_L = 3yu_L/L^2$.

Fig. 2a shows the conductance of two samples, fabricated by identical processes using the shadow masking method and measured in the same range of tensile strain. Both devices exhibited an initial conductance of approximately $3G_0$, with $G_0$ being the conductance quantum $G_0 = 2e^2/h = (12.9\,\mathrm{k\Omega})^{-1}$. For sample A, the conductance decreased by a factor of 4 by a strain of 0.6%, while device B exhibited no detectable change in conductance before electrical connection was irreversibly lost at a strain of 0.42%. An inspection of sample B showed that the nanotube was broken. For sample A, the conductance returned to its initial value when the deflection was reduced to zero. The experiment was repeated with an identical metal coated cantilever, however, without an integrated MWCNT, and here no change in conductance was observed.

Three measurements performed on the same device are shown in Fig. 2b. The three successive measurements show similar behavior with linear change in conductance as a function of strain, and

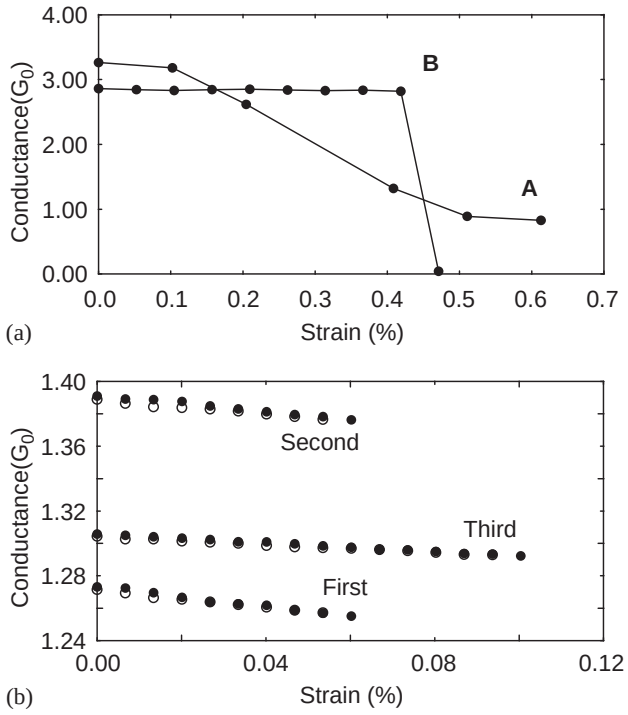


Fig. 2. (a) Measurements of the conductance as a function of strain for two MWCNT samples. Both devices had a conductance of roughly $3G_0$ at zero strain. Device A showed a dramatic decrease of the conductance by a factor of 4 as the strain is increased to 0.6%, while the conductance of device B did not change, before it broke at a strain of 0.42%. (b) Three conductance measurements performed on the same device. Full circles denote values obtained for increasing strain, and open circles for decreasing strain. The three measurements showed similar behavior even though the initial conductance and gauge factors varied. The conductance as a function of strain is linear and strain variations below 0.01% are resolved. The zero-strain conductance is seen to vary 5% from the average conductance, and the gauge factors are ranging from 10–24 decreasing in successive measurements.

the change in conductance is decreasing from 1.4% in the first measurement to 1% in the third. The zero-strain conductance is seen to vary 5%.

Translating the resistance changes into gauge factor, $g = \Delta R/\varepsilon R$, we obtain gauge-factors in the range 0–24, except for a single device with a gauge factor of 500. Although more measurements have to be done in order to provide statistics, it is noteworthy that most of the samples exhibit low gauge factors. Experimentally, gauge factors as large as 1000 have been observed by Tombler et al [13].

A rough estimate of the expectable gauge factors of SWCNT can be obtained from the maximal energy bandgap changes expected from small tensile strain, $dE_g/d\varepsilon \approx \pm 9.6\,\text{eV}$ for semiconducting [12] and metallic nanotubes and $dE_g/d\varepsilon \approx \pm 7.6\,\text{eV}$ for quasi-metallic nanotubes [20], and the resistance in terms of energy bandgap $R = R_c + R_0(1 + \exp(E_g/2k_BT))$ where $R_0 \approx h^2/4h$ is the two-terminal resistance of a ballistic, metallic nanotube [11]. From $g = (1/R)dR/d\varepsilon = (1/R)(dR/dE_g)(dE_g/d\varepsilon)$ we then get the maximal gauge factors $g_{max} \approx \pm 185$ for metallic and semiconducting nanotubes, and $g_{max} \approx \pm 146$ for quasi-metallic nanotubes assuming negligible contact resistance.

The simplest explanation of the rather low gauge factors is that the MWCNT simply slides in the metallic layer on the cantilever, i.e. the metal is either not sufficiently thick, hard or adhesive to effectively pull the MWCNT. A more subtle explanation could be that other conduction mechanisms contribute to the total conduction, either due to adsorbed gas molecules, water [21] or alternatively surface conduction due to a water thin film on the $SiO_2$ material between the electrodes. This could in principle make the resistance less sensitive to strain, thus effectively reducing the gauge factor.

It is however worth noting, that interactions between shells of the MWCNT makes the situation different from that of SWCNT. Our measurements were performed on MWCNT, which are expected to consist of randomly alternating series of zig-zag, armchair and chiral nanotubes. For near-perfect MWCNT, as produced by arc-discharge or laser ablation methods, the coupling between the individual shells is presumably poor, which may be expressed as a high inter-shell resistance [22]. In this case the gauge factor of the MWCNT would be mainly determined by the outer shell.

The calculated distribution of gauge factors for four ensembles of $2.5 \times 10^5$ MWCNT's (15 shells) chosen with random coordination numbers ($n$,$m$), with a outer diameter of around 35 nm and inner diameters decreasing by two times the inter shell distance, 3.5 Å are plotted in Fig. 3. For each shell the resistance is estimated from the energy gap [20,23],which together with the gauge factor is

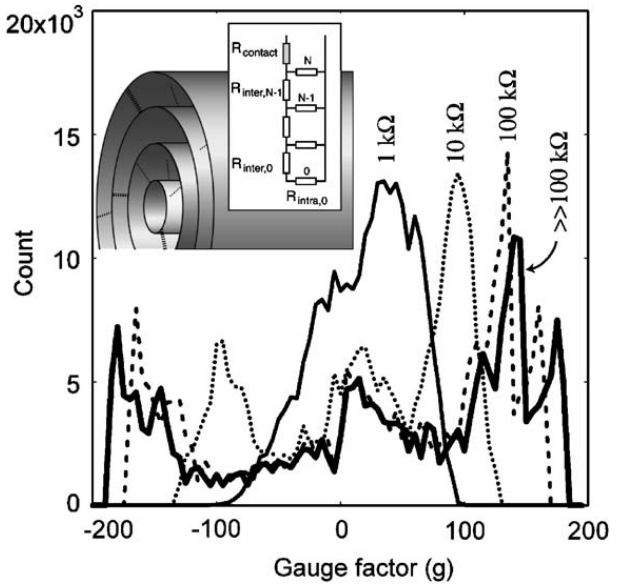


Fig. 3. The calculated distribution of gauge factors for an ensemble of $10^4$ MWCNT with diameters around 35 nm. The gauge factor is calculated by taking several shells into account, using the model shown in the inset. The shells are picked randomly with coordination numbers so that the diameter fits between neighboring shells. The resistance of each shell, $R_{\text{intra}}$, is calculated from the energy band gap given by the coordination numbers.

calculated from the coordination numbers. The thick line shows the distribution of gauge factors calculated as in Ref. [11], assuming the outer shell to be considered insulated from the inner shells. To estimate the contribution of the inner shells, a finite inter-shell resistance is taken into account, using a naïve resistor network model illustrated in Fig. 3 (inset) for values of $R_{\text{inter}} = 1$, 10 and 100 kΩ. Clearly, a low inter-shell resistance makes the gauge factors smaller, i.e. closer to zero. The device does not allow a direct evaluation of the contact resistance; however, the 2-point resistance values found are comparable to the lowest found in literature for MWNT, i.e. down to 4 kΩ. Using direct measurement with movable cantilever probes arrays [24] we found the difference to be around 1 kΩ between 2P and 4P measurements for MWNT picked from the same batch, so $R_{\text{contact}}$ is assumed negligible and is set to zero.

By adopting the method of shell-burning initially demonstrated by Collins and Avouris [22] investigations of the inter-shell coupling and shell conductivity has been performed [25]. By modeling the nanotube as a resistor network, the inter-shell resistance of the investigated nanotubes was found to be 1–10 kΩ, indicating that the nanotubes used are far from ideal in terms of integrity of the individual shells. The nanotubes in the present study were fabricated by CVD, so the relatively low inter-shell resistance is most likely related to geometrical defects, which is consistent with gauge factors not exceeding 50–100, simply due to mixing of contributions from shells with positive, small and negative gauge factors.

An explanation for the large observed gauge factor of 500 could be that a defect zone by chance was located in the electrode gap, which could lead to a higher sensitivity to mechanical deformation. Comparison of nanotube strain devices using arc-discharge carbon nanotubes with our results obtained with CVD-grown MWCNT is necessary to further clarify this issue.

Measurements have been performed on few devices due to a low yield. The low yield was mainly due to nanotubes either not properly connected to begin with, or loosing contact when deflecting the cantilever. We speculate that the thickness and material of the metallic layer could be critical in obtaining a good electrical as well as mechanical contact. We are currently optimizing this aspect of the device.

The nanowire shadow-mask device is analogous to the mechanical break junction, except that the component is integrated in a cantilever, so that a deflection of the cantilever leads to a change in resistance. Hence, this technique may be used not only to investigate the electro-mechanical properties of nanowires and nanotubes, but also for integration of nanotubes or nanowires as strain sensors in microcantilevers, similar to silicon-based piezoresistors [26]. Whereas silicon based piezoresistors are difficult to integrate on the nanoscale, nanotubes have an obvious advantage in size with a gauge factor comparable to that of silicon. Possible applications could be as force feedback sensors in micro- or nano-AFMs suitable for characterization and manipulation of nanostructures, cantilever based biosensors or tactile nanotweezers.

## Acknowledgement

We thank Mads Brandbyge and Peter Rasmussen for valuable discussions. The research was supported by a talent project grant "NANO-HAND" from the Danish Technical Research Council.

## References

[1] M.S. Dresselhaus, Y.M. Lin, O. Rabin, A. Jorio, A.G. Souza Filho, M.A. Pimenta, R. Saito, Ge. Samsonidze, G. Dresselhaus, Mater Sci Eng.: C 23 (2003) 129.
[2] R. Martel, T. Schmidt, H.R. Shea, T. Hertel, Ph. Avouris, App. Phys. Lett. 73 (1998) 2447.
[3] J. Kong, C. Zhou, A. Morpurgo, H.T. Soh, C.F. Quate, C. Marcus, H. Dai, Appl. Phys. A Mater. Sci. Proc. 69 (1999) 305.
[4] S.J. Tans, A.R.M. Verschueren, C. Dekker, Nature 393 (1998) 49.
[5] P.L. McEuen, Appl. Phys. Lett. 79 (2001) 1363.
[6] A. Star, J.-C.P. Gabriel, K. Bradley, G. Gruner, Nano Lett. 3 (2003) 459.
[7] J. Kong, N.R. Franklin, C.W. Zhou, M.G. Chapline, S. Peng, K.J. Cho, H.J. Dai, Science 287 (2000) 622.
[8] S.S. Fan, M.G. Chapline, N.R. Franklin, T.W. Tombler, A.M. Cassell, H.J. Dai, Science 283 (1999) 512.
[9] A. Bachtold, P. Hadley, T. Nakanishi, C. Dekker, Science 294 (2001) 1317.
[10] J.W. Ding, X.H. Yan, J.X. Cao, D.L. Wang, Y. Tang, Q.B. Yang, J. Phys. Condens. Matter 15 (2003) L439–L445.
[11] J. Cao, Q. Wang, H. Dai, Phys. Rev. Lett. 90 (2003) 157601.
[12] L. Yang, J. Han, Phys. Rev. Lett. 85 (2000) 154.
[13] T.W. Tombler, C.W. Zhou, L. Alexseyev, J. Kong, H.J. Dai, L. Lei, C.S. Jayanthi, M.J. Tang, S.Y. Wu, Nature 405 (2000) 769.
[14] A. Maiti, A. Svizhenko, M.P. Anantram, Phys. Rev. Lett. 88 (2002) 126805.
[15] P.J. de Pablo, E. Graugnard, B. Walsh, R.P. Andres, S. Datta, R. Reifenberger, Appl. Phys. Lett. 74 (1999) 323.
[16] C.L. Petersen, T.M. Hansen, P. Boggild, A. Boisen, O. Hansen, T. Hassenkam, F. Grey, Sensors and Actuators a-Phys. 96 (2002) 53.
[17] P. Boggild, T.M. Hansen, C. Tanasa, F. Grey, Nanotechnology 12 (2001) 331.
[18] J.E.A.M. van den Meerakker, R.J.G. Elfrink, F. Roozeboom, J.F.C.M. Verhoeven, J. Electrochem. Soc. 147 (2000) 2757.
[19] S.D. Senturia, Microsystem Design, first ed., Kluwer Academic Publishers, 2001.
[20] A. Kleiner, S. Eggert, Phys. Rev. B (Condens. Matter) 63 (2001) 073408.
[21] O.K. Varghese, P.D. Kichambre, D. Gong, K.G. Ong, E.C. Dickey, C.A. Grimes, Sensors Actuators B: Chem 81 (2001) 32.
[22] P.C. Collins, M.S. Arnold, P. Avouris, Science 292 (2001) 706.
[23] J.W. Ding, X.H. Yan, J.X. Cao, Phys. Rev. - Section B – Condens. Matter 66 (2002) 73401.
[24] R. Lin, P. Boggild, O. Hansen, J. Appl. Phys. 96 (2004) 2895.
[25] S. Dohn, K. Mølhave, D.N. Madsen, P. Bøggild, unpublished.
[26] J. Thaysen, A. Boisen, O. Hansen, S. Bouwstra, Sensors Actuators A-Phys 83 (2000) 47.

# Soldering of Carbon Nanotube Bridges using Electron Beam Deposited Gold

Søren Dohn, Kristian Mølhave, Dorte Nørgaard Madsen, Ramona Mateiu, Peter Bøggild, Anne Marie Rasmussen[1], Michael Brorson[1] and Claus J.H. Jacobsen[1]
MIC, Technical University of Denmark, Building 345 east, DK-2800 Kgs. Lyngby, Denmark
[1]Haldor Topsøe A/S, Nymøllevej 55, DK-2800 Kgs. Lyngby, Denmark

## ABSTRACT

We have formed suspended bridges of carbon nanotubes between microcantilevers using electron beam dissociation of metal-organic vapours. By electron beam exposure of a surface in the presence of gold-carbon molecules emitted inside an environmental scanning electron microscope, we are able to form tips and other freestanding nanostructures of high metallic content. Suspended bridges made entirely of this material exhibit resistances less than 50 times that of pure gold, and consist of dense metallic cores surrounded by a crust of nanoparticles. We used standard microfabrication techniques to produce silicon chips with multiple microcantilevers extending over the edge. Individual multiwalled carbon nanotubes grown catalyticcally by chemical vapour deposition, were positioned across two cantilevers using in-situ nanomanipulation tools. Drawing a cross-shaped gold-carbon bond on each end of the carbon nanotube consistently resulted in electrical contact with resistances in the range 1-90 kΩ and linear current-voltage characteristics. We found that soldering bonds having a line width down to 10-15 nm form connections and lasts for days in ambient conditions.

## INTRODUCTION

Since the discovery of the carbon nanotube (CNT) in 1991 by S. Iijima [1], the CNT has been foretold a great future in electronic devices and as reinforcement in various materials due to the unique mechanical and electrical properties. To gain insight as well as to fabricate prototype devices it is therefore of paramount importance to obtain electrical connections to CNT. In practice, studies of the electrical properties generally require the nanotubes to be interfaced to measurement equipment via microelectrodes. This is often done by dispersing CNT on a surface and subsequently manipulating the nanotubes towards electrodes [2] or alternatively, locating the positions of the nanotubes for subsequent lithographic deposition of electrodes [3].

Although these methods have proven excellent for investigations of the electrical properties alone, the interplay of mechanical and electrical properties is more accessible from studies of suspended nanotube bridges that allow electrical measurement during mechanical deformation. Such bridges have been formed by underetching devices after deposition of electrodes [4], and by growth from prepositioned catalytic material. Finally, nanomanipulators equipped with sharp tips have been used inside scanning electron microscopes (SEM) to mechanically bend and pull nanotubes while monitoring their electrical conductance [5]. In these experiments, none of the methods used appear to offer strong mechanical connection combined with low-resistance electrical contact, a prerequisite for reliable studies of electro-mechanical properties.

Lately, in-situ made deposits of carbonaceous material was used to measure the torsional spring constant of a single carbon nanotube bridge, with a paddle attached to the middle of a suspended multiwalled carbon nanotube (MWNT). These experiments clearly show the potential of electron beam deposition as a direct way of attaching nanotubes to electrodes. In these experiments the conductance was not simultaneously monitored [6]. Hence, a major issue

regarding the investigation and application of nanotubes is the mechanical and electrical contact between the nanotube and the device.

In this paper we describe a method for fixing a nanotube in-situ by electron beam deposition of gold, which reduces the contact resistance. The contact region between the nanotube and the deposited gold is mechanically very strong and at the same time highly conducting.

## EXPERIMENTAL METHODS

We used a Philips XL30 ESEM-FEG environmental SEM, operating at a water vapor pressure of 100 Pa. The metalorganic precursor, Dimethylacetyl-acetonate gold(III), which has a vapor pressure of 1 Pa at 25ºC, was placed in a container outside the ESEM chamber, and lead into the ESEM through an aluminum tube (Figure 1) equipped with valves and a pump to control the diffusion rate of metal-organic vapor. This reduces unwanted contamination significantly, since vapor is only distributed in the chamber when needed. A nanomanipulator stage inside the chamber was used to move a silicon chip with four microcantilever electrodes [7]. The electrodes were connected to a DC voltage source and the current was monitored continuously.

We used two batches of Chemical Vapor Deposition (CVD)-grown multiwalled nanotubes, sample 1 with diameters in the range of 80 nm - 120 nm fabricated at Haldor Topsøe A/S and sample 2 with diameters of 20-100 nm, donated by R. Czerw, Clemson University. After placing one such nanotube sample in the ESEM, a microelectrode pair was aligned to a MWNT extending from the sample, so both electrodes touched the nanotube. By slowly scanning the beam across the nanotube, two cross-shaped gold-carbon soldering bonds were formed on each nanotube-electrode intersection. In this way we fabricated five devices.

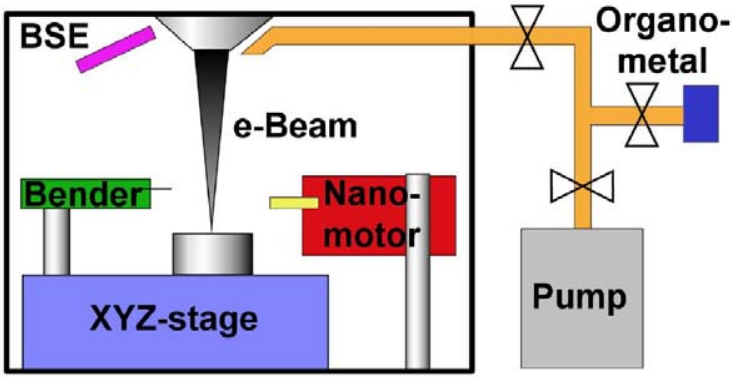


**Figure 1.** ESEM setup used for nanosoldering of MWNT on silicon microelectrodes. The metalorganic precursor was placed in a container outside the chamber of the ESEM, and connected through aluminum tubes equipped with valves and a pump to control the diffusion of metalorganic vapor into the chamber. A nanomanipulator stage mounted inside the chamber was used to align a silicon chip with four cantilever microelectrodes and a MWNT for soldering. Further, an STM tip placed on a piezo-electric bender manipulator, and was used for testing the mechanical stability of the soldered bonds.

When opening the valve connecting the chamber to the metalorganic precursor, the maximum rate of deposition was reached after 10 minutes. After two minutes of pumping

followed by closing of the valve connecting the chamber to the metalorganic compound, the rate of EBD was reduced to a point where nearly no soldering or contamination occurred.

**RESULTS**

Focusing the electron beam on a substrate lead to narrow tips growing at a rate of 400 nm per min. Figure 2A shows such a tip with a length of 1.5 μm. TEM analysis of the soldering material revealed a gold-carbon composite structure with a porous crust containing of 3-5 nm nanoparticles around a dense core (Figure 2A and 2B). From these TEM images it appears that the core consists of large crystalline domains. By controlling the deposition conditions the structure of the deposits can be changed from nearly homogeneously distributed particles to a dense core surrounded by a carbon crust.

We deposited free-standing wires connecting suspended nanotubes, by slowly moving the beam spot between nanotubes. Several such bonds were investigated in a TEM, as shown in

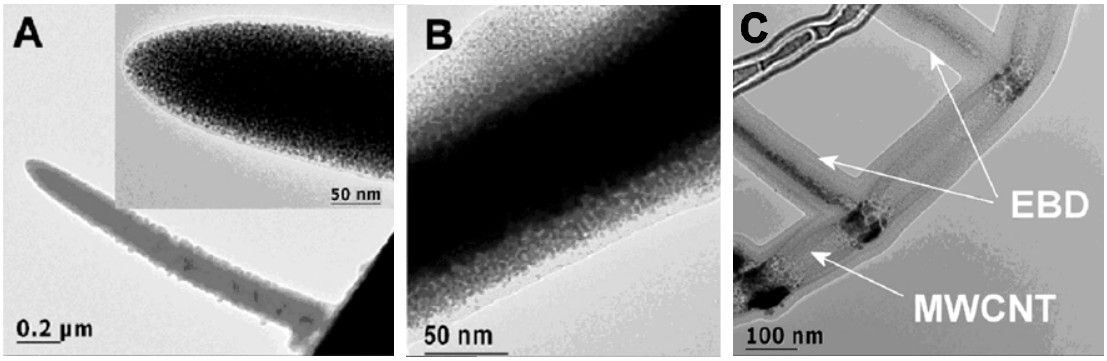


**Figure 2.** A) TEM image of a beam of soldering material. In the inset, the porous crust of amorphous carbon with 3-5 nm gold nanoparticles can be seen. B) changing the deposition conditions can lead to generation of a dense gold core with a nanoparticle crust. C) TEM image of a MWNT with a beam of electron beam deposited gold. The gold is seen to penetrate the shells of the MWNT forming a solid core. On the outer shell of the MWNT a layer of amorphous carbon is deposited on the MWNT as well as on the EBD wire.

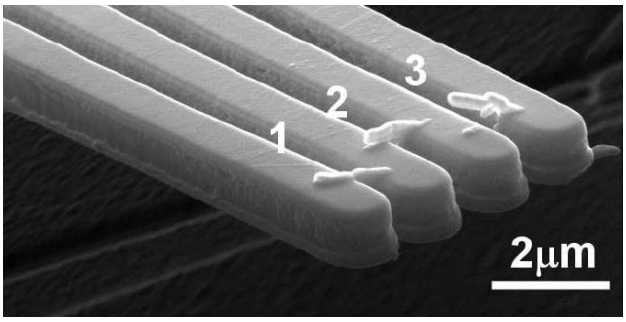


**Figure 3.** SEM image of three bridges of soldering material deposited between microelectrodes by scanning the electron beam across the gaps at different speeds (fastest for bridge 1). The resistances were 127 Ω for bridge 1 and 520 Ω for bridge 2. Bridge 3 did not connect to both electrodes.

Fig. 2C. The deposited wire connections have dense gold-containing cores with diameters down to 20-30 nm. It appears that the soldering wire at the contact point penetrates the nanotube, resulting in deformation of the nanotube structure. On the nanotube as well as on the deposited soldering wires, a layer of amorphous carbon was deposited. In these experiments, the precursor source was not switched off between actual soldering. By regulating the deposition rate the thickness of this carbon shell could be significantly reduced.

A verification that the soldering material was conducting was obtained by depositing bridges of soldering material between microelectrode pairs and measuring the IV characteristics. All of the bridges that connected properly to both microelectrodes, such as bridges 1 and 2 in Figure 3, exhibited Ohmic resistances between 80 Ω and 520 Ω. By estimating the cross-section of the bridges from SEM images and taking a serial resistance of roughly 60 Ω into account, we estimated the resistivities to be around $10^{-4}$ Ωcm.

An example of a MWNT from sample 2 before and after soldered to four microelectrodes is seen in Figure 4A-B while Figure 4C shows a nanotube from sample 1 bridging 2 electrodes. The latter was biased by 10 mV during the soldering. When the second bond of this carbon nanotube bridge was deposited, the current abruptly jumped to a higher stable value, as shown in Figure 4D.

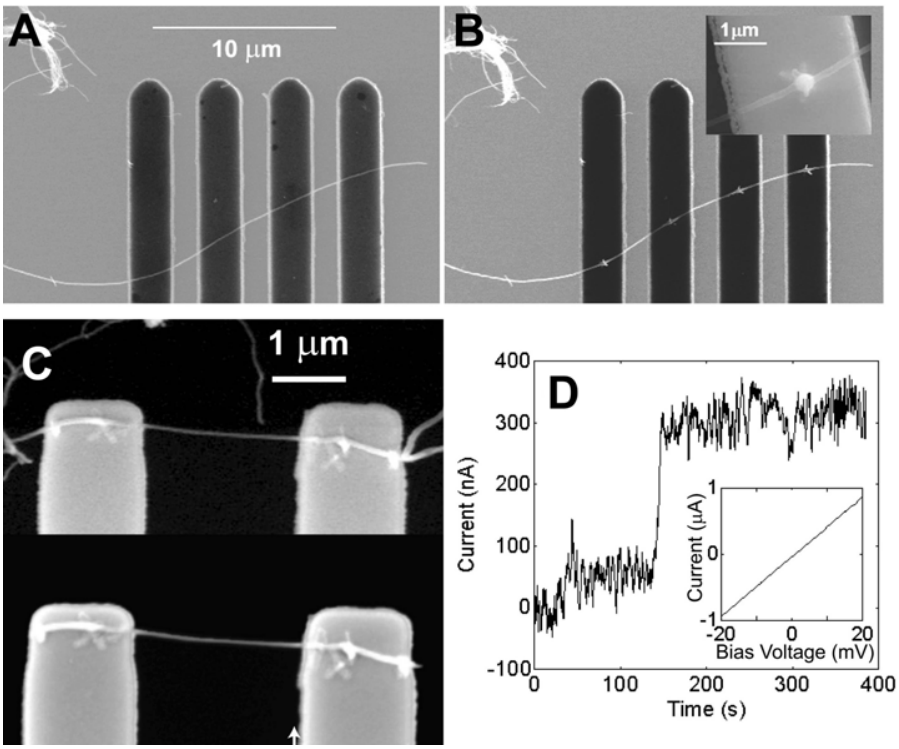


**Figure 4.** A) SEM image of a microelectrode four point probe, with a carbon nanotube positioned across. B) Four cross-shaped solderings have been deposited on the nanotube (inset: enlarged view of a single soldering point). C) By forming "cutting" bonds near the edges of the cantilevers, the nanotube tends to break off at the edge, without damaging the cross-shaped bond. D) A fixed voltage of 10 mV was applied across the microelectrodes. During deposition of the second bond, the current abruptly increased to 300 nA, indicating that the soldering now forms a good electrical contact. The inset shows the IV curve of the MWNT bridge after soldering.

The resistance was typically found to be in the range 10-30 kΩ, while in a few cases resistances as small as 1 kΩ and as large as 90 kΩ were measured. As was reported earlier [8], the breaking of the soldered CNT could be done without harming the soldering bonds by depositing a protective bond near the edge of the microelectrode. This lead in most cases to breaking of the nano-tube near the edge, and not at the soldering bond itself, as seen in the lower panel of figure 4C.

The strength of the soldering bonds was tested with an STM tip mounted on a piezo-electric bender (see Figure 1). Figure 5 shows the STM tip deflecting a microcantilever supporting one end of a 150 nm wide carbon nanotube bridge. A lower estimate for the bond strength can be derived from the deflection of the center electrode, which from the images is seen to be roughly 250 nm. Using a piezoresistive force cantilever chip, we measured the spring constant of the microelectrode to be 0.08 N/m, which gives a minimum force applied to the bond of $20\times10^{-9}$ N.

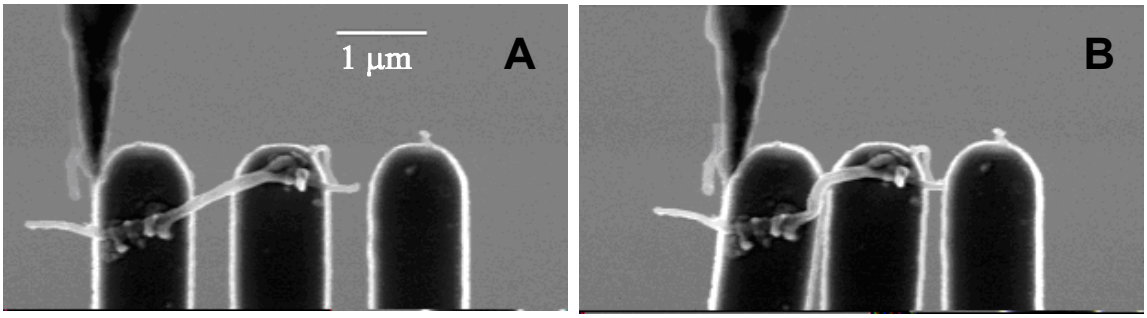


**Figure 5.** A) A 150 nm diameter carbon nanotube was bonded to two microcantilevers. A sharp scanning tunneling tip mounted on a piezobender is touching the leftmost cantilever. B) The tip deflecting the cantilever and thereby deforming the nanotube did not seem to damage the soldering bonds. During the operation the center electrode deflected 250 nm.

## DISCUSSION

The question regarding the contribution of individual shells in MWNTs to the conductivity of the tube is still not resolved. Frank et al. [9] observed a consistent resistance of 13 kΩ for nearly defect-free arc-discharge-grown MWNTs, whereas Collins and co-workers [10] found lower values (5-15 kΩ) and evidence of several contributing shells at low bias. Whereas each shell ideally should contribute $4e^2/h$ to the conductance (assuming two open channels), corresponding to a resistance of 6.5 kΩ, only the outer shell is expected to contribute at low bias voltages because of a high inter-shell resistance [10]. This however depends on whether the contact couples to one or more shells. It appears in figure 2 that the gold material connects to the center of the CNT, which suggest that many shells may be connected. On the other hand, a deformation of the carbon nanotube is taking place. This may explain the rather different resistances measured. CVD grown tubes typically have more defects than arc-discharge or laser-ablation grown tubes. Such defects affect the inter-shell scattering and the elastic mean free-path. It is possible that defects in some cases can cause more shells and thereby conducting channels to be available for transport. This however requires more thorough investigations to clarify.

The resistivity of the soldering material is slightly larger than the value of $1.3\times10^5$ Ωcm reported by Bietsch et al. for microcontact-printed pure gold nanowires of similar dimensions [11] and two orders of magnitude larger than that of bulk gold. For electron-beam-deposited nano-

wires, resistances as small as ours have been obtained by heating the sample to 80°C during deposition to increase the relative content of gold [12]. These values were obtained only after annealing at 180°C, which further reduced the resistivity by 2-3 orders of magnitude. An explanation for the high conductivity of our material achieved at room temperature without annealing could be that the presence of $H_2O$ in the sample chamber reduces the relative amount of carbon, as suggested by Folch and co-workers [13]. This will be addressed elsewhere [14].

Whereas the results indicate a highly conducting core in the free-standing soldering deposits, it was not possible to verify a gold core in substrate deposits, i.e. connections between a nanotube and a microelectrode. Secondary electrons are expected to play an important role in the electron beam deposition, and it is likely that the presence of the substrate changes the composition and structure of the deposits. This may be investigated using a semi-transparent TEM substrate, that would scatter low-energy electrons in the ESEM but not the high-energy electrons of the TEM.

We have presented a method for forming reliable mechanical and electrical connections between nanotubes and microelectrodes. The method does not depend on the particular nanocomponent or on the electrodes. It involves no lithographic steps or electrical connections such as in spot welding, and it is straightforward to achieve accurate alignment. With further refinement of the system for regulation of the deposition rate the contamination problem is expected to be entirely resolved. The goal is to have the possibility of fitting the soldering system into a SEM, without risk of contamination. The system is now being equipped with a homebuilt electron beam lithography system, for controlling the beam position using a PC interface. We anticipate automated electron beam nanosoldering to be useful for quickly connecting complex circuitry consisting of nanoscale components in a way similar to the soldering of electronic components on the macroscale.

## ACKNOWLEDGEMENTS

We thank Richard Czerw for carbon nanotube samples. The project was funded through a "talentproject" grant from Danish Technical Research Council.

## REFERENCES

[1] Iijima, S.: *Nature* 1991, 354, 56 (1991)
[2] Avouris Ph. et al.: *Appl. Surface. Sci.* 1999, 141, 201
[3] Fritzche, W. et al.: *Nanotech.* 1999, 10, 331
[4] Nygard, J. et al.: *Appl. Phys. Lett.* 2001, 79, 4216
[5] Tombler, T. W. et al.: *Nature* 2000, 405, 769
[6] Williams P. A. et al.: *Appl. Phys. Lett.* 2003, 82, 805
[7] Bøggild, P. et al.: *Nanotechnology*, 2001, 12, 331
[8] Madsen, D. N. et al.: *Nano Lett.* 2003, 3, 47
[9] Franks, S. et al.: *Science* 1998, 280, 1744
[10] Collins, P. G. et al.: *Appl. Phys. A* 2002, 74, 329
[11] Bietsch, A. et al.; *Appl. Phys. Lett.* 2002, 80, 3346
[12] Koops, H. W. P. et al.: *M. J. Vac. Sci. Technol., B* 1996, 14, 4105
[13] Folch, A. et al.: *Appl. Phys. Lett.* 1995, 66, 2080.
[14] Mølhave, K. et al, in preparation.